Modelling of crystal plasticity effects in the fracture of a metal/ceramic interface - bridging the length scales

Muhammad Amir Siddiq

Modelling of crystal plasticity effects in the fracture of a metal/ceramic interface - bridging the length scales

Von der Fakultät Maschinenbau
der Universität Stuttgart
zur Erlangung der Würde eines
Doktor-Ingenieurs (Dr.-Ing.)
genehmigte Abhandlung

vorgelegt von
MSc.
Muhammad Amir Siddiq
aus
Karachi /Pakistan

Hauptberichter:	Prof. Dr. S. Schmauder
Mitberichter:	Prof. Dr. M. Rühle
Tag der mündlichen Prüfung:	06.07.2006

Institut für Materialprüfung, Werkstoffkunde und Festigkeitslehre der Universität Stuttgart
und
Max-Planck-Institut für Metallforschung, Stuttgart
Juni 2006

Acknowledgements

I would like to express my deepest gratitude to Prof. S. Schmauder for his continuous guidance throughout my research work at Institut für Materialprüfung, Werkstoffkunde und Festigkeitslehre (IMWF), Universität Stuttgart. I also express my warm and sincere heartfelt thanks for every discussion that I had with him, the confidence he had shown and the vast amount of patience he had with me.

I would like to thank Prof. M. Rühle for his support during this work and accepting to become the “Mitberichter” for my thesis.

I would also like to thank Prof. G. Cailletaud (Centre des Materiaux, Ecole Nationale Superieure des Mines de Paris), Prof. Y. Huang (University of Illinois at Urbana-Champaign), Prof. M. Finnis (Imperial College London), Dr. R. M. Cannon (Lawrence Berkeley Laboratory, USA), Dr. J. Kysar (Columbia University) and Dr. D. Brunner (Max-Planck-Institut for Metal Research) for the useful discussions and forward-looking suggestions.

Special thanks to Prof. G. Cailletaud for the ZMAT program and Prof. Y. Huang for crystal plasticity subroutines.

Furthermore, I would like to thank Dr. I. Scheider (GKSS-Forschungzentrum) for providing the cohesive model subroutine for this work and the discussions that I had with him.

I would also like to thank Prof. D. Raabe and Mr. A. Ma (Max-Planck-Institute for Iron Research, Düsseldorf) for providing the uniaxial compression test data of niobium single crystalline material.

I am very grateful to my colleagues at IMWF, all members of the group, especially Peter Binkele and Wolfgang Lutz, for warm working atmosphere, many beneficial works and private discussions, and support with solving all kind of problems.

I would also like to acknowledge my colleagues at Graduiertenkolleg for their cooperation and friendly atmosphere we had during the meetings and retreats.

Finally, I express my thanks to my family and friends for their support, friendship and love during the whole period of this work. I would especially like to thank my mother who has been patiently waiting for my PhD to finish. My brother Imran for taking care of my mother during this time and my sister Ambreena, who always kept me motivated to finish this thesis.

Stuttgart, June 2006 Muhammad Amir Siddiq

Dedicated to my parents and siblings, specially to my late father who died during my stay in Germany

Table of Contents

Nomenclature V

Kurzfassung 1

1. Introduction 5

2. Metal/Ceramic Interfaces 7

2.1 Review of Literature 8
2.1.1 Experimental Studies 8
2.1.2 Ab-Initio Studies 9
2.1.3 Continuum Studies 10

2.2 What is still required? 12

2.3 Goal of this work 12

3. Theoretical Background 14

3.1 Crystal Plasticity Theory 14
3.1.1 Plastic Flow in Metals 14
3.1.2 Kinematics of Crystal Plasticity 15
3.1.3 Constitutive Law 15
3.1.4 Strain Hardening 16
3.1.5 Dislocation Mechanics based Crystal Plasticity Models 19
3.1.6 Numerical Implementation 23

3.2 Fracture Mechanics 26
3.2.1 Global Energy Method 27
3.2.2 Virtual Crack Closure Technique 28
3.2.3 J-Integral Method 30

3.3 Crack Growth Criterion 32
3.3.1 Characteristic Parameters of Node Release Techniques 32
3.3.1.1 Maximum Stress Criterion 32
3.3.1.2 Crack tip Opening Displacement Criterion 32
3.3.1.3 Maximum Energy Release Rate Criterion 33
3.3.2 Damage Mechanics Approach 33
3.3.3 The Cohesive Model 33

3.4 Finite Element Method (FEM) 37

4. Results 41

4.1 Material Parameter Identification of Single Crystalline Niobium 41
4.1.1 Introduction 41

4.1.2 Strain Hardening Models 42
4.1.3 Deformation Behaviour of Niobium Single Crystals 44
4.1.4 Modelling 45
4.1.5 Results and Discussion 46
4.1.6 Summary 54

4.2 Crystal Orientation Effects of the Metal on the Crack Initiation Energies of a Bimaterial Interface (Nb/Al_2O_3) 55
4.2.1 Introduction 55
4.2.2 Finite Element Model 56
4.2.3 Finite Element Analysis 57
4.2.4 Results and Discussion 59
4.2.5 Summary 74

4.3 Effect of Thermal Residual Stresses 75
4.3.1 Introduction 75
4.3.2 Finite Element Model 75
4.3.3 Finite Element Analysis 76
4.3.4 Results and Discussion 78
4.3.5 Summary 79

4.4 Interface Fracture Analyses Using a Cohesive Modelling Approach 80
4.4.1 Finite Element Model 80
4.4.2 Results and Discussion 81
4.4.2.1 Effect of Cohesive Law Parameters on Fracture Energy 81
4.4.2.2 Stresses along the Crack Front ahead of the Crack Tip 91
4.4.2.3 Local Mode Mixity at the Crack Tip 93
4.4.2.4 Stress Triaxiality at the Crack Tip along the Interface 97
4.4.2.5 Influence of Strain Gradient Crystal Plasticity 100
4.4.3 Correlation between Local Adhesion Capacity and Macroscopic Fracture Energy 104
4.4.4 Summary 110

5. Summary and Conclusion 112

References 118

Nomenclature

Chapter 2: Metal-Ceramic Interface

$W_{elastic}$ work of elastic deformation
$W_{plastic}$ work of plastic deformation
W_{adh} work of adhesion
Γ fracture energy
γ_{12} interface energy
σ_{1v} surface energy of the material 1
σ_{2v} surface energy of the material 2

Chapter 3: Theoretical Background

A crack front area
G cross hardening function
G_c energy release rate
G_I mode-I energy release rate
G_{II} mode-II energy release rate
J j-integral
$\underline{\underline{K}}$ stiffness matrix
L_{ijkl} elasticity tensor
U total energy of the specimens
$a^{\alpha\beta}$ interaction matrix
$\underline{b}$ body force
$\underline{f}^{e}_{ext}$ external nodal force
$\underline{f}^{e}_{\mathrm{int}}$ internal nodal force
$f_{\alpha\beta}$ interaction strength
g^{α} strength of slip system α
h_0 initial hardening moduli
h_s hardening moduli during easy glide
$h_{\alpha\beta}$ hardening moduli
m rate sensitivity exponent
$\underline{m}^{\alpha}$ vector normal to slip system α
q latent to self hardening ratio
$\underline{s}^{\alpha}$ vector tangent to slip system α
δ crack opening displacement
ε_{ij} total strain tensor
ε^{el}_{ij} elastic strain tensor
ε^{pl}_{ij} plastic strain tensor
γ plastic shear strain
γ^{α}_0 reference shear strain
γ^{α} plastic strain in slip system α
η material constant

μ_{ij}^{α} schmidt factor of slip system α
ρ density
ρ_0 initial dislocation density
ρ_{sat} saturation dislocation density
σ_f normal failure stress
σ_{ij} stress tensor
σ_n normal stress
$\overset{\nabla}{\sigma}$ jaumman rate of cauchy stress
τ_0 resolved shear stress at yielding
τ_1 shear stress in 1-direction
τ_1^f shear failure stress in 1-direction
τ_2 shear stress in 2-direction
τ_2^f shear failure stress in 2-direction
τ_s saturation resolved shear stress
τ^{α} resolved shear stress in slip system α

Chapter 4: Results

E_c elastic modulus
J_C fracture energy
K_I mode-I stress intensity factor
K_{II} mode-II stress intensity factor
L characteristic length
$L_n(t)$ cost function
$R^*(\varepsilon)$ experimental data
$R(\varepsilon)$ simulation data
T T-stress
$\underline{b}$ Burgers vector
g_0 reference slip resistance
g_T^{α} effective slip resistance
g_s^{α} slip resistance due to statistically stored dislocations
g_G^{α} slip resistance due to geometrically necessary dislocations
h thickness of metal layer
l intrinsic material length
n hardening exponent
r distance from the crack tip
Γ_0 work of adhesion
α thermal expansion coefficient
β dundurs second parameter
ε elastic mismatch
η_G density of geometrically necessary dislocations
μ shear modulus
μ_1 shear modulus of material 1

μ_2 shear modulus of material 2
υ_1 poisson’s ratio of material 1
υ_2 poisson’s ratio of material 2
σ_0 yield stress
σ_c cohesive strength
σ_{xx} normal opening stress
σ_{xy} shear stress
σ_y yield stress
ψ' local phase angle
ψ loading phase angle

Kurzfassung

Die Materialkombination Metall/Keramik ist weithin bekannt und hat viele industrielle Anwendungen. Zum Beispiel wird Aluminiumoxid (α-Al_2O_3) in der elektronischen Industrie seit vielen Jahren als keramische Isolierung eingesetzt, während Niob, Aluminium und Kupfer als Elektrodenmaterialien verwendet werden, da sie eine gute Leitfähigkeit besitzen. Pulver und Fasern von Aluminiumoxid (α-Al_2O_3) werden auch zur Verstärkung. von Aluminiumlegierungen, eines der gebräuchlichsten Leichtmetalle für Bauteile in Fahrzeugen und anderen Transportsystemen angewendet.

Metall/Keramik-Verbunde werden in der modernen Technologie immer wichtiger, weil sie die Eigenschaften der Metalle wie Duktilität, hohe elektrische und Wärmeleitfähigkeit und die Eigenschaften von Keramiken wie hohe Härte, Korrosionsbeständigkeit und Verschleißfestigkeit kombinieren. Der Bruch an oder nahe solcher Grenzflächen begrenzt häufig die Zuverlässigkeit dieser Verbindungen. Die Kenntnis der Spannungs- und Deformationsfelder an der Risspitze an Metall/Keramik-Verbundgrenzflächen ist erforderlich, um ein grundlegendes Verständnis dieses Bruchprozesses zu entwickeln. In vielen Situationen beginnen Risse an der Grenzfläche und verlaufen entlang der Grenzfläche, in Richtung der Grenzfläche oder von ihr weg.

Diese Arbeit befasst sich mit einer Studie der Kristallplastizitätseffekte an der Grenzfläche von Metall/Keramik-Verbunden für das System Nb/Al_2O_3. Ein Verfahren wird beschrieben, um das Bruchverhalten des Systems Nb/Al_2O_3 realistisch zu simulieren. Die Kristallplastizitätstheorie [43] wurde verwendet, um den Einfluss der Kristallorientierung auf die plastische Deformation und schließlich auf die Bruchenergie des Systems Nb/Al_2O_3 zu berücksichtigen. Die Analyse der Rissausbreitung wird mit Hilfe eines Kohäsivzonenmodells [84, 85] durchgeführt. Das entscheidende Ziel dieser Untersuchung ist die theoretische Aufklärung des Zusammenhangs zwischen der lokalen Adhäsionskapazität und makroskopischen Bruchenergie.

Die Niobeinkristallmaterialien werden immer als kubisch-raumzentrierte Kristalle mit Hilfe der Kristallplastizitätstheorie behandelt. Die dreistufige Verfestigung der Niobeinkristalle während der Deformation wird mit dem Modell von Bassani und Wu modelliert. Für kubisch-raumzentrierte Kristalle sind für das Modell von Bassani und Wu 20 Parameter zu bestimmen, d. h. 10 Parameter für jede Familie der Gleitsysteme. Ein Interface-Programm wurde entwickelt um die mit ABAQUS simulierte Spannungs-Dehnungs-Kurve zusammen mit den dazugehörigen kristallplastischen Verfestigungsparameter zu einem Optimierungsprogramm

zu übertragen. Das Optimierungsprogramm vergleicht die simulierte Spannungs-Dehnungs-Kurve mit der experimentellen Kurve. Durch Anwendung der Methode der kleinsten Fehlerquadrate werden die neuen kristallplastischen Verfestigungsparameter bestimmt, die als Input für die FEM-Simulation dienen. Diese Prozedur wird wiederholt bis eine gute Übereinstimmung zwischen der experimentellen und der simulierten Spannungs-Dehnungs-Kurve für beide Gleitsysteme erhalten wird.

Für die Berechnung der Bruchenergie für zwei- und dreidimensionale Strukturen sind unterschiedliche Techniken, wie die globale Energiemethode, die virtuelle Rissschließungs-technik (VCCT) und die J-Integralmethode, verwendet worden.

Weiterhin wurden Vier-Punkt-Biege-Versuche von Bikristallproben mit der Kristall-plastizitätstheorie für den Niobeinkristall simuliert. Die Simulationsergebnisse der Vier-Punkt-Biege-Versuche des Bikristalls zeigen im Falle einer stationären Rissspitze, dass es eine z.T. sehr starke Veränderung der Bruchenergie für unterschiedliche Kristall-orientierungen gibt, und zwar mit denselben Trends wie sie auch in den Experimenten gemessen wurden.

Dieses liegt an der plastischen Anisotropie der Niobeinkristalle, die nicht durch die kontinuumsmechanische Deformations-Plastizitätstheorie berücksichtigt wird, weil diese Theorie nur für isotrope Materialien verwendet werden kann. Der Unterschied in den Bruchenergien kann mit dem unterschiedlichen Beitrag der Dehnung jedes Gleitsystems bei der plastischen Gleitung für verschiedene Kristallorientierungen erklärt werden. Die Ergebnisse der Finite-Elemente-Analyse mit Hilfe der Kristallplastizitätstheorie zeigen für eine stationäre Rissspitze die gleiche Tendenz der berechneten und der experimentell bestimmten [20, 21] Bruchenergien.

Der Effekt der thermischen Eigenspannungen, die in der Bikristallprobe während des Diffusionsschweißens entstehen, wenn ein Probe von der Schweißtemperatur 1400 °C auf Raumtemperatur abgekühlt wird, ist ebenfalls untersucht worden. Da die Fehlpassung in den Koeffizienten der thermischen Ausdehnung sehr klein ist, ergibt sich, dass die hierdurch verursachten thermischen Restspannungen ebenfalls klein sind. Folglich wurde kein bedeutender Effekt auf die Bruchenergien für das Nb/Al_2O_3-System gefunden.

Der Grenzflächenbruch des Nb/Al_2O_3-Bikristall-Systems wird im Falle eines sich ausbreitenden Risses mit einem Kohäsivzonenmodell studiert. Dabei werden die Bruchenergien an das Experiment angepasst und es ergeben sich höhere Kohäsivfestigkeiten für höheren Bruchenergien (u.u.). Parameterstudien wurden durchgeführt, um die Auswirkung der unterschiedlichen Kohäsivgesetzparameter, wie die Bindungsstärke und die Adhä-

sionsarbeit auf die Bruchenergie und den Rissfortschrittswiderstand zu untersuchen. Hierbei wurde gefunden, dass sich die maximale Kohäsivspannung auf die Bruchenergie nicht linear auswirkt und verglichen mit der Adhäsionsarbeit weitereichender ist. Weiterhin wurde gefunden, dass sich mit steigender Kohäsivspannung, auch die Bruchenergie wegen der höheren plastischen Energiedissipation erhöht. Zusätzlich hängt die Bruchenergie linear von der Adhäsionsarbeit für verschiedene Orientierungen des Niobeinkristalls in der Nb/Al_2O_3-Bikristallprobe ab. Die Parameter des Kohäsivzonenmodells wurden für unterschiedliche Kombinationen für die maximale Kohäsivspannung und Adhäsionsarbeit bestimmt, indem ein skalenübergreifendes Verfahren angewendet wurde, wie die Abbildung zeigt:

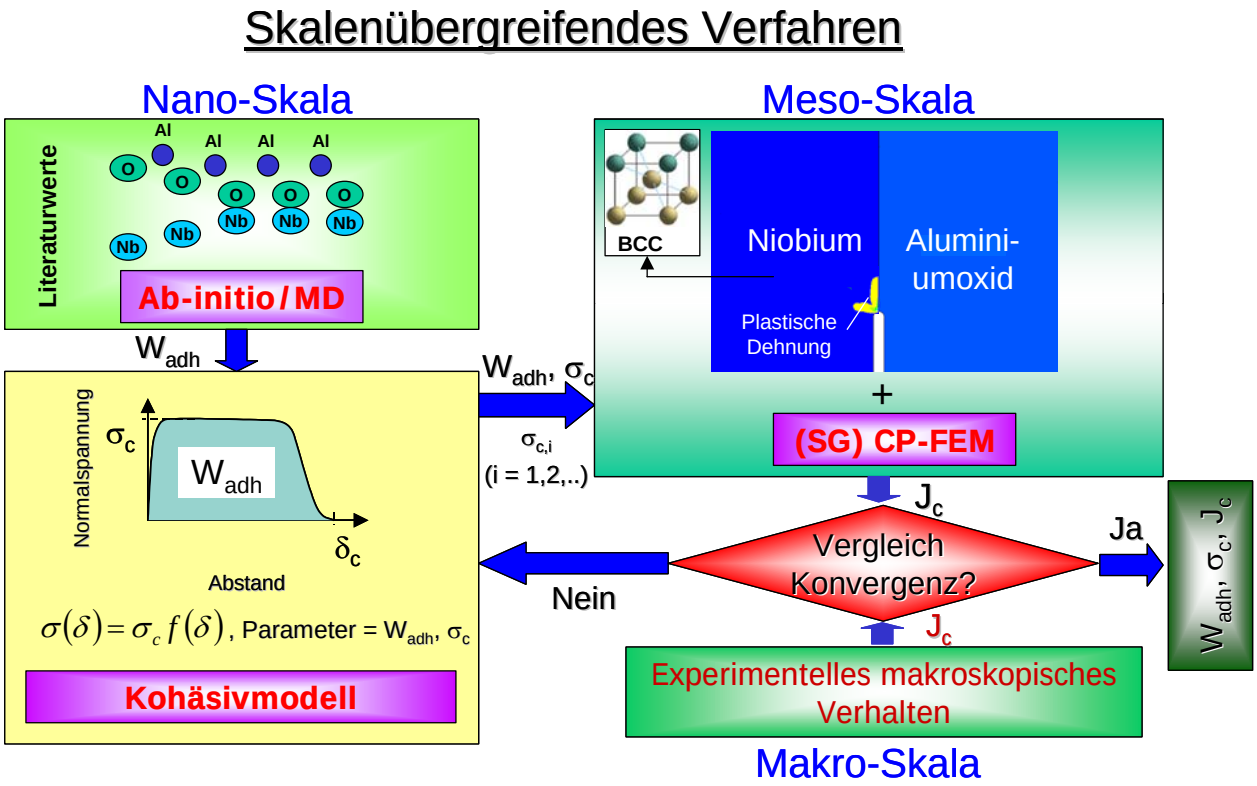

Abbildung: Skalenübergreifendes Verfahren für die Simulation des Metall/Keramik-Grenzflächenbruchs

Dabei werden drei unterschiedliche Längenskalen verknüpft, wie in der Abbildung gezeigt und die Skalenüberbrückungsparameter sind die Adhäsionsarbeit (W_{adh}) und die maximale Kohäsivspannung (σ_c) für die Verbindung zwischen der atomistischen und der Mesoskala sowie die makroskopische Bruchenergie (J_c) zur Verknüpfung der Mesoskala mit der Makroskala. Für jeden Wert der Adhäsionsarbeit wird die maximale Kohäsivspannung (σ_c) variiert und dem Finite-Elemente-Modell für den Bikristall Niob/Aluminiumoxid als Eingangsparameter für die Adhäsionsarbeit (W_{adh}) übergeben. Hiermit wird dann der Grenzflächenbruch simuliert. Niobeinkristalle werden mittels der Kristallplastizitätstheorie in

der Nähe der Grenzfläche des Niob/Aluminiumoxid-Bikristalls modelliert. Das Resultat der Simulation, d.h. die Bruchenergie des Systems wird dann mit dem experimentellen Bruchenergiewert verglichen. Wenn Übereinstimmung erreicht wurde, dann wird der endgültige Satz der Grenzflächenbruchparameter (σ_c, W_{adh}) und die Bruchenergie (J_c) des Systems berechnet, andernfalls wird die Simulation mit einer neuen Annahme der Kohäsivspannung (σ_c) wiederholt. Dieses Verfahren wurde für jeden Wert der Adhäsionsarbeit (W_{adh}) wiederholt.

Die Spannungen entlang der Rissfront vor der Rissspitze und die lokalen Belastungs-Modenverhältnisse werden auch für die Fälle stationärer Rissspitzen und für wachsende Risse analysiert. Es wird gefunden, dass der Beitrag der Scherspannungen verglichen mit den Normalspannungen vor der Rissspitze vernachlässigt werden kann, weil die Fehlpassung in den elastischen Eigenschaften von Niob und Aluminiumoxid klein ist. Auf der Basis der Spannungen vor der Rissspitze wird das lokale Modenverhältnisse berechnet und gefunden, dass es im Bereich –7° bis -4° liegt. Dies zeigt, dass das lokales Modenverhältnis eine untergeordnete Rolle für Niob/Aluminiumoxid-Bikristallproben spielt.

Der Einfluss der Dehnungsgradienten-Kristallplastizitätstheorie wird zusätzlich auch mit der mechanismenbasierten Kristallplastizitätstheorie studiert. Es wird gezeigt dass wegen der hohen Dehnungsgradienten in der Nähe der Rissspitze, d.h. im Bereich von 0,1 - 2 μm, die Spannungen für die mechanismenbasierte Dehnungsgradienten-Kristallplastizitätstheorie immer höher sind als für die herkömmliche Kristallplastizitätstheorie. Es wird auch gefunden, dass der Unterschied bezüglich der Spannungen von beiden Theorien nicht groß ist - dies liegt an dem niedrigen Verhältnis von Probengröße/Größe der plastischen Zone. Weiterhin wird auch gezeigt, dass beiden Theorien dieselbe Gesamtbruchenergie liefern.

Im letzten Teil der Dissertation wird eine generalisierte Wechselbeziehung zwischen der Bruchenergie, der Kohäsivspannung, der Adhäsionsarbeit und der resultierenden Spannung an der Grenzfläche abgeleitet. Weiterhin wurden die Parameter für diese Wechselbeziehung für unterschiedliche Orientierungen der Niobeinkristalle in Niob/Aluminiumoxid-Bikristall-proben bestimmt.

1. Introduction

The combination of metal and ceramic is well known and has many industrial applications. For instance, alumina has been used in electronic industry for many years as a ceramic insulator, whereas niobium, aluminium and copper are three of the best electrodes, having good conductivity. Powders and fibres of alumina are also used to reinforce aluminium alloys, one of the most common lightweight materials for components in automobile engines and other transportation systems.

Metal/ceramic joints become more and more important in modern technology, because they combine the properties of metals like ductility, high electrical and thermal conductivity and the properties of ceramics like high hardness, corrosion resistance and capacity of resistance to wear. The fracture at or near such interfaces often limits the reliability of these joints. Knowledge of the stress and deformation fields at the crack tip at a metal/ceramic interface is needed in order to develop a fundamental understanding of this fracture process. In many situations, cracks initiate at interfaces and advance along, towards or away from the interfaces.

The safety of such components inevitably requires a thorough understanding of their behaviour under load. Such studies to explain the metal/ceramic interfaces have not been performed in detail in the past. Therefore, an effort is put to devise a procedure which can simulate a realistic fracture behaviour of niobium/alumina bicrystal interfaces. Effects of crystal orientations of niobium single crystalline material on the fracture energy is studied using crystal plasticity theory. The ultimate goal of the investigation is to theoretically clearing-up the connection between local adhesion capacity and macroscopic fracture energy. All the work has been performed to study niobium/alumina bicrystal interfaces where niobium single crystalline material is bonded with alumina. The single crystalline niobium is always modelled using crystal plasticity theory in order to take into account crystal orientation effects which is different than polycrystalline material. The reason is that polycrystalline material is always modelled as an isotropic material while single crystalline materials always show plastic anisotropy if crystal orientation is changed. Therefore, plastic anisotropy of a single crystalline material can only be taken into account using crystal plasticity theory.

The work is divided into five parts. The introduction of metal/ceramic interfaces along with the literature review about the work that has been done until now in this field is presented in chapter 2. The goal of this work is also presented in chapter 2.

In chapter 3 the theoretical background of crystal plasticity theory is discussed. Furthermore, basics of interface fracture mechanics, different crack growth criteria and finite element method, are highlighted in chapter 3.

In chapter 4 results of the finite element simulations of metal/ceramic interface fracture using crystal plasticity theory are presented and discussed. In section 4.1 an automatic identification procedure is presented to identify the hardening parameters of individual slip systems in single crystalline niobium. Hardening parameters are identified for three different orientations of single crystalline niobium.

In section 4.2 four-point-bending test simulations are performed to study the crystal orientation effects of the metal on the crack initiation energies of a bicrystal niobium/alumina interface. The simulation results show that changing the crystal orientation has strong influence on crack initiation energies and the trends in crack initiation energy are the same as were found in the experiments. In section 4.3 the effect of thermal residual stresses is studied which are induced during the diffusion bonding of niobium/alumina interface. The results show the induced thermal residual stresses are very low due to the small mismatch in the thermal expansion coefficients of niobium and alumina. This shows that the effect of thermal residual stresses is almost negligible.

Interface fracture analyses is performed using a cohesive modelling approach in section 4.4. The effect of different cohesive law parameters such as cohesive strength and work of adhesion is analyzed in detail. The results show that cohesive strength has stronger effects on macroscopic fracture energies, i.e., a nonlinear cubic relation while macroscopic energies are linearly dependent on the work of adhesion. Based on these results a correlation is derived for three different orientations of niobium/alumina bicrystal interfaces. Other factors such as stresses along the crack front ahead of the crack tip, local mode mixity and stress triaxiality at the crack tip are also studied and the results show that there is no significant effect of these parameters on fracture energies of bicrystalline niobium/alumina interfaces. The correlation derived in this work can bridge the gap between meso- and macroscopic length scales involved in the fracture of metal/ceramic interfaces.

In chapter 5 the results obtained throughout this work are summarized and future outlook of the work is presented.

2. Metal/Ceramic Interfaces

Metal/ceramic interfaces play a vital role in modern materials technology, as evident by their use in a variety of applications (figure 1). For example, high-strength materials such as metal-matrix composites consist of internal interfaces between ceramic (e.g. SiC or Al_2O_3) particles or filaments within a metallic host. Because of their high melting points, extreme hardness, and favourable corrosion resistance, ceramic coatings are often used to protect an underlying metallic component in environments subject to high temperatures and wear rates (i.e., cutting tools). In microelectronics packaging, interfaces between metallic (Cu and/or Al) inter-connects and SiO_2, carbide/nitride (TiCN) or oxide (Al_2O_3) ceramics are commonplace, and impact the performance and longevity of solid state devices.

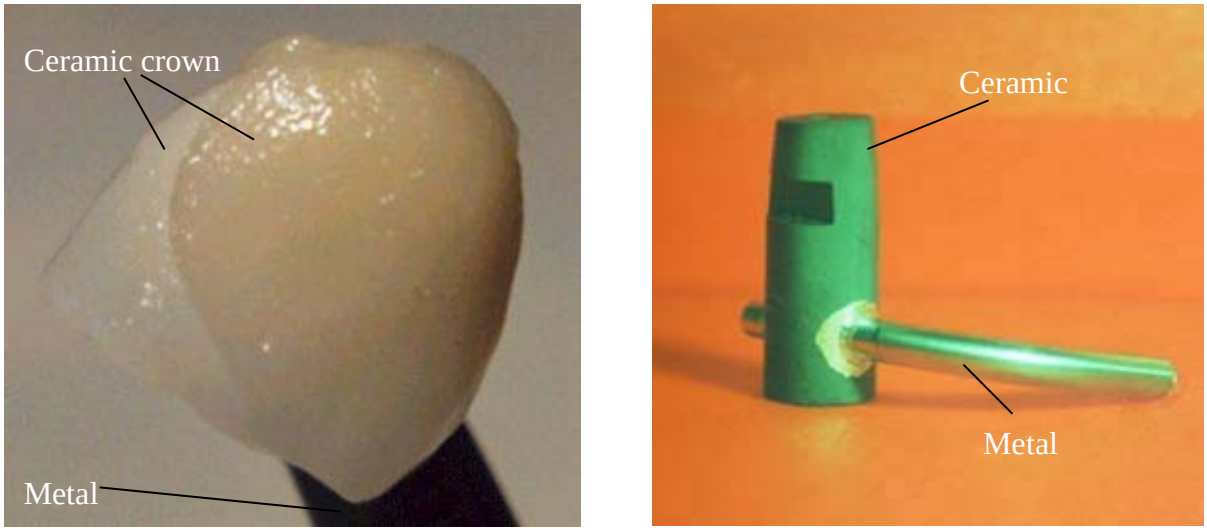

(a) (b)

Figure 1: Typical metal/ceramic systems; (a) metal/ceramic crown [1] and (b) pressure port of the crew returning vehicle X38, metal-inconel [2].

Despite their widespread use, a basic understanding of these interfaces has been elusive. For example, given a particular metal/ceramic interface, it is not yet possible to accurately predict such fundamental properties as its fracture energy. In most of the cases, improvements in interface properties proceed via a costly and time consuming trial-and-error process in which numerous materials are evaluated until suitable performance is obtained.

Computational methods provide a wide range of possibilities to study the fracture behaviour of such metal/ceramic interfaces. Scientists and engineers have been studying different metal/ceramic interfaces for a long time, in order to create a better understanding of the factors that influence the fracture behaviour of the metal/ceramic interfaces, such as plasticity induced around the crack tip and interface strength. In what follows next, a brief review of

literature is presented describing the work that has already been conducted on different metal/ceramic systems, such as niobium/alumina and copper/alumina.

2.1 Review of Literature

2.1.1 Experimental Studies

A fundamental quantity which influences the mechanical properties of an interface is the ideal work of adhesion, W_{adh} [3], which is defined as the energy required to break interfacial bonds and reversibly separate an interface into two free surfaces, neglecting diffusion, elastic and plastic deformation. When combined with the work of plastic deformation, $W_{plastic}$, and work of elastic deformation, $W_{elastic}$, the work of adhesion determines the fracture energy of an interface, Γ separating material 1 and 2:

$$\Gamma = W_{elastic} + W_{plastic} + W_{adh} \tag{1}$$

The work of adhesion is defined in terms of the surface and interfacial energies, which is given by:

$$W_{adh} = \sigma_{1v} + \sigma_{2v} - \gamma_{12} \tag{2}$$

Here σ_{iv} is the surface energy of material i=1, 2, γ_{12} is the interface energy.

The most straightforward and common way to determine W_{adh} experimentally is through a sessile drop experiment [4 - 6]. In these works, interfacial energies for metal/Al_2O_3 systems were estimated. Metal used for these experiments were Ni, Cu, Al and Au on pure, polycrystalline alumina.

The mechanical properties of single crystalline sapphire/Nb/sapphire joints were investigated in [7, 8] for different orientation relationships between metal and ceramic. The orientation of the single crystalline material was found to have significant effects on the fracture energies of the Nb/Al_2O_3 interface.

The influence of chemical composition of a region at or close to an interface on the strength of a metal-ceramic interface was studied in [9]. It was found that the strength of a metal/ceramic interface depends upon the density of the metal-oxide bonds. Ni/Al_2O_3 and Cu/Al_2O_3 joints were studied in [10, 11, 12], it was found that higher strength results from adding reactive alloying elements. This addition of alloying elements raises the work of adhesion.

Various groups [13 - 18] postulated that the fracture energy of interfaces depends not only on W_{adh}, but also on the amount of plasticity that occurs in the metal during the fracture process, on the interfacial flatness, and on their interrelation. Gibbesch et al. [19] found that the

fracture energy of Nb/sapphire and Cu/sapphire interfaces changes dramatically with the relative crystallographic orientation of the two constituents. Beltz [20, 21] and Korn et al. [22, 23] observed that the amount of plasticity initiated in the metal during fracture of such interfaces is strongly influenced by both, the interface chemistry and the orientation of the slip system relative to the fracture plane. Kysar [24] studied the Cu/sapphire interface and the directional dependence of the crack for various orientations. Fuller et al. [51] and Chiao [52] observed dislocation emission from crack tips, and also proposed that brittleness or ductility of a crack tip can be characterized by its response to mechanical loading. Jameel et al. [53] studied the brittleness and ductility of cracks along the interface of copper bicrystals. The brittleness and ductility of the crack tip was explained in terms of angles that various slip systems make with the crack flanks. They found that these angles of slip planes plays a critical role in the process of deformation at the crack tip.

2.1.2 Ab-Initio Studies

Niobium and sapphire form stable interfaces which are of importance both practically and as model systems because there is almost no chemical reaction at the interface. Moreover, both niobium and sapphire single crystalline material possess similar coefficients of thermal expansion [22, 23], with a coefficient of thermal expansion of single crystalline niobium $\alpha_{Nb} = 7.3x10^{-6}K^{-1}$ and of single crystalline alumina $\alpha_{Al_2O_3(0001)} = 5.8x10^{-6}K^{-1}$ and $\alpha_{Al_2O_3(11-20)} = 6.8x10^{-6}K^{-1}$.

Different researchers have performed ab-initio calculations to understand the adhesion at a fundamental quantum-mechanical level [25 - 28]. Methfessel et al. [25] performed ab-initio calculations to compute the surface energies of 4d transition metals (Y, Zr, Nb, Mo, Tc, Ru, Rh, Pd, Ag). The surface energies of the fcc and bcc structures for (111), (100) and (110) surfaces were computed. They modelled niobium as both face-centered-cubic (fcc) and body-centered-cubic (bcc), although niobium exists as bcc in nature. Results for the case of niobium are given below in Table I:

Table I: Surface energies of niobium

	Crystal structure	Surface	Surface Energy [J/m^2]
Niobium	fcc	(111)	2.20
	fcc	(110)	2.26
	bcc	(110)	2.36
	bcc	(100)	2.86

Finnis et al. [26] performed ab-initio calculations of metal/ceramic interfaces. These calculations not only predicted the electronic structure of the interface but also the ideal work of adhesion. The calculations were based on niobium(111)/α-alumina(0001) interfaces. The computed value of the adhesion energy of a niobium monolayer to the oxide surface amounts to 9.8 J/m^2. Batirev et al. [27] also performed the ab-initio calculations. The work of adhesion for O- and Al-terminated niobium(111)/α-alumina(0001) interfaces was reported. The results are shown in Table II:

Table II: W_{adh} for niobium(111)/α-alumina(0001) interfaces [27]

Interface type	Location (/) of fracture plane	W_{adh} [J/m^2]
$Nb_m/(Al_2O_3)_O$	Nb/O-Al-Al…	10.8
$Nb_b/(Al_2O_3)_O$	…Nb-Nb-Nb/O-Al-Al-O…	9.8
$Nb_b/(Al_2O_3)_{Al}$	…Nb-Nb-Nb/Al-O-Al-Al…	2.8
Nb_b/Nb_m-$(Al_2O_3)_O$	…Nb-Nb-Nb/Nb-O-Al-Al…	3.8

Here $(Al_2O_3)_{Al}$ designates an Al-terminated α-alumina (0001) surface, and $(Al_2O_3)_O$ the O-terminated α-alumina (0001) surface. The surface of niobium is denoted by Nb_b, and a monolayer of niobium on $(Al_2O_3)_O$ is denoted by $Nb_m/(Al_2O_3)_O$.

Smith et al. [28] examined the relative stability of both stoichiometric and non-stoichiometric niobium(111)/α-alumina(0001) interfaces. The work of adhesion was computed using two methods local-density approximation (LDA) [28] and generalized-gradient approximation (GGA) [28]. The work of adhesion computed was consistent with the results of Finnis [27]. Table III depicts the results achieved from their calculations:

Table III: W_{adh} for niobium(111)/α-alumina(0001) interfaces

Interface type	Ref. 28, LDA [J/m^2]	Ref. 28, GGA [J/m^2]	Ref. 25, [J/m^2]
$Nb/(Al_2O_3)_{Al}$	3.3	2.6	2.8
$Nb/(Al_2O_3)_O$	12.3	10.6	9.8

2.1.3 Continuum Studies

Continuum mechanical studies have been done by many researchers to study and understand the fracture behaviour of metal/ceramic interfaces. Armstrong [48] and Kelly [49] proposed that distinction between the intrinsic brittleness and ductility can be considered as a competition between cleavage failure and plastic shear at the crack tip.

McHugh [29,33] studied aluminium/rigid and copper/rigid material interfaces numerically. A rate dependent crystal plasticity theory was used [30 - 32]. A hybrid decohesion model based

on cohesive strength and work of adhesion, was proposed to describe the crack propagation along the interface. The model is discussed in section 3.3.3.

Mason [48] and Rice [20] used the rate dependent crystal plasticity theory, whereas Asaro [30 - 32] studied the crack tip behaviour of a copper/sapphire interface. Rice [20] interpreted the experimental results of Beltz [21] based on the dislocation nucleation. It was shown that brittle failure occurs when the energy required for dislocation nucleation is greater than the energy required for cleavage, while, the failure is ductile if the energy required for dislocation nucleation is less than the energy required for cleavage.

Wang [43] performed a series of interfacial fracture experiments on specially oriented copper symmetric tilt bicrystals and reported a directional dependence of crack growth; that is, the interfacial crack oriented in one crystallographic direction propagates much more readily than the crack on the same interface but oriented to propagate in the opposite crystallographic direction. Wang [34] proposed a micromechanical model for interface cracking. Three different systems were studied, i.e., gold/sapphire, aluminium/sapphire and nickel/sapphire. The model proposed in this work, predicted the crack tip behaviour, i.e., ductility or brittleness of the crack tip, consistent with the experimental observations [21].

In addition to the dislocation nucleation analyses, there have been other approaches to predict relative brittleness and ductility. Kysar [35 - 37] studied the directional dependence of crack growth along a copper/sapphire interface. Finite element analyses of copper/sapphire bicrystal speciement were performed using crystal plasticity theory. It was shown that relative ductility/brittleness can be explained on the basis of the normal opening stress.

Nakatani [38] analyzed the small-scale yielding around a stationary crack along a ductile single crystal-rigid material interface. Both continuum slip and discrete dislocation plasticity theory were used with either two or three slip systems. Results obtained using both theories were found to be consistent. The discrete dislocation simulations provide a valuable window into the actual micromechanics of how near-tip plastic deformation develops, and what the actual underlying dislocation distribution is that corresponds to the macroscopic elastic-plastic deformation pattern. However limitations on how many dislocations can be handled and how many computer runs can be made, make it difficult to determine the near-tip stress and deformation fields that occur on a larger scale near such a crack tip. This information can be obtained from the continuum crystal plasticity solutions, which gave full-field results for the elastic-plastic continuum crystal plasticity solutions. It was also shown that both discrete dislocation simulations and continuum cystal plasticity theory accurately predict the crack tip opening behaviour, which is important in understanding the type of failure anticipated.

Kohnle [39, 40] analyzed polycrystalline niobium/sapphire interface. The influence of the plastic properties of the metal part on the interface strength and on the energy release rate is examined. It was shown that a low yield stress results in high plastic deformation in the metal part and consequently a higher energy is stored before the critical stress value for crack propagation is reached. As these studies were performed to study the polycrystalline niobium/sapphire interface, therefore, are not enough to explain the experiments performed on niobium/alumina bicrystal specimens where niobium single crystalline material is bonded with alumina. Also, these studies do not explain the effect of orientation of single crystalline niobium on fracture energies of bicrystal niobium/alumina specimens.

2.2 What is still required?

As discussed in the previous section, most of the work has been done to study the directional dependence of crack growth in metal/ceramic interfaces. Most of the attention is given to study the brittleness or ductility of the crack tip during crack propagation along copper/sapphire interfaces.

The majority of researchers have studied fcc crystals and out of those researchers, only, Kysar [35, 36] has put some effort to find the hardening parameters involved in the crystal plasticity theory and compared it with experimental results of uniaxial tension tests for single crystalline copper. One reason is the availability of experimental results and another reason is to use the crystal plasticity theory for the case of bcc seems to be complicated because there are three families of slip systems present in bcc crystals as compared to fcc single crystals which have one family of slip systems.

In reality, engineers are interested in validating the analysis results with experiments which has not been considered in the majority of these works as how these theories can be used to quantitatively validate the experimental results, such as, experimentally computed fracture energies, etc.

Therefore, an effort is required to devise a procedure which can simulate the fracture behaviour of bcc metal/ceramic interfaces and quantitatively validate it with experiments.

Also, theoretically clearing-up the connection between local adhesion capacity and macroscopic fracture energy is still to be addressed.

2.3 Goal of this work

Korn et al. [22, 23] and Cannon [42] studied the influence of crystal orientation and impurities on the fracture behaviour of niobium/sapphire interfaces using notched bending specimen. They observed that the amount of plasticity initiated in the metal during fracture of

such interfaces is strongly influenced by both the inerface chemistry and the orientation of the slip systems relative to the fracture plane and direction.

The fracture energy derived from the experiments for various interface orientations between niobium (Nb) and sapphire (Sp) at a bonding temperature of 1400 °C are summarized in Table IV, respectively:

Table IV: Fracture energy and interface orientation of bicrystals consisting of sapphire and single crystalline niobium, bonded at 1400 °C

Orientation relationship	Symbol	J_c [J/m^2]
Nb(100)[001]|Sp(11-20)[0001]	Or I	115
Nb(110)[001]|Sp(11-20)[0001]	Or II	370
Nb(111)[-1-12]|Sp(11-20)[0001]	Or III	112

They found that changing the orientation strongly influences the fracture energy. It was also found [22, 23] that specimens bonded at different temperatures give different fracture energies. It was found that specimens bonded at 1400 °C had lower fracture energy than the specimens bonded at 1300 °C. The reason is, reducing the bonding temperature from 1400 °C to 1300 °C reduces the yield stress of niobium, at room temperature, from 74 MPa to 56 MPa [43, 44]. This change in yield stress of niobium is attributed to an increase in dissolved oxygen (0.055 % at 1300 °C and 0.099 % at 1400 °C) which results from dissolving alumina [43, 44]. The decrease in oxygen content reduces the yield stress of niobium [43, 44]. The reduction in yield stress of niobium by decreasing the bonding temperature from 1400 °C to 1300 °C causes more macroscopic plasticity, in the bicrystal specimens leading to higher toughnesses when deformed at room temperature.

The goal of this work is to study crystal plasticity effects in the fracture of metal/ceramic interfaces (Nb/Al_2O_3) when a single crystalline metal is used. An effort is being put to devise a procedure which can simulate the fracture behaviour of Nb/Al_2O_3-systems. The crystal plasticity theory [45] will be applied to take crystal orientation effects into account. Finite element analyses will be performed using crystal plasticity theory for various orientations of bicrystal specimens. A cohesive model [87, 88] is applied to perform crack propagation analyses. Parametric studies are performed to study the effect of different cohesive model parameters, such as interface strength and cohesive energy (work of adhesion) on the fracture energies of the niobium/alumina-interfaces. An attempt will be made to theoretically clear-up the connection between local adhesion capacity and macroscopic fracture energy.

3. Theoretical Background

In this chapter, a brief overview of crystal plasticity theory is summarized. Furthermore, some basic concepts of fracture mechanics will be discussed along with an overview of cohesive models used in crack propagation analyses. Lastly, after creating a basic understanding of the theory, finite element methods are briefly discussed, in which these theories have been implemented.

3.1 Crystal Plasticity Theory

3.1.1 Plastic Flow in Metals

Based on Taylor's finding [54], plastic deformation in metals starts when dislocations move along specific crystallographic planes in a specific crystallographic direction. Therefore, the fundamental deformation mechanism is a shearing action along a specific crystallographic direction. In figure 2, a picture of a deformed single crystalline niobium surface illustrates this feature. The sample has been loaded in uniaxial tension. As the specimens deforms, slip occurs on slip planes where the resolved shear stress is high. At larger deformations several slip systems can be activated, due to hardening on activated planes and lattice rotations.

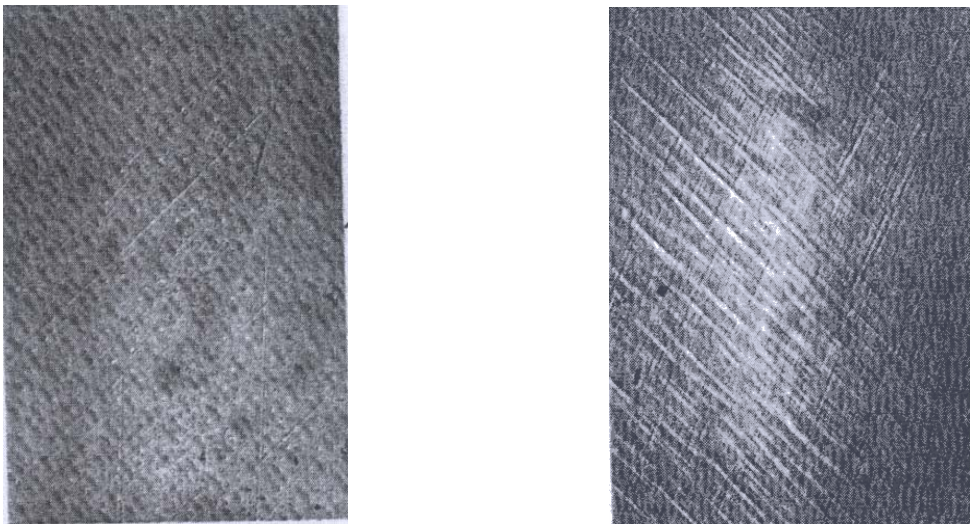

(a) (b)

Figure 2: (a) Single slip in single crystalline niobium, (b) Multiple slip in single crystalline niobium [88]

As discussed above, the main physical mechanism of plastic deformation at ambient temperatures is the flow of dislocations along crystal slip systems. Slip systems are close packed atomic planes. This yields the smallest dislocation Burgers vector magnitude and

hence the most favourable direction for slip. Some basic crystal structures and major slip systems are (indicated by their Miller Indices) as follow:

- fcc with a total number of twelve slip systems of (111)[110]-type
- bcc with a total number of 48 slip systems, out of which, twelve slip systems are of (110)[111]-type, twelve of (112)[111]-type and twenty four of (123)[111]-type
- hcp with slip systems of (0001)[1110]-type

3.1.2 Kinematics of Crystal Plasticity

In crystal plasticity theory, dislocation flow on a slip system is represented in a continuum sense as a plastic shear strain γ. Crystal plasticity is considered to be a physically based theory, since it is based on the microstructural behaviour of materials. To make the kinematical concept of shearing in slip directions useful, shear strains are related to a tensorial representation of deformation and/or strain. The precise mathematical theory was proposed by Hill [55], Rice [56], Hill and Rice [45] and Asaro [57]. The following is a basic summary of the theory.

During loading of an elastic-plastic crystal, the total strain rate is the sum of elastic strain rate and plastic strain rate, given by:

$$\dot{\varepsilon}_{ij} = \dot{\varepsilon}_{ij}^{el} + \dot{\varepsilon}_{ij}^{pl} \tag{3}$$

The evolution of plastic strain rate is related to the slipping rate $\dot{\gamma}^{\alpha}$ of the α-*th* slip system by:

$$\underline{\dot{\varepsilon}}^{p} = \sum_{\alpha} \dot{\gamma}^{\alpha} \underline{s}^{\alpha} \underline{m}^{\alpha} \tag{4}$$

where the sum ranges over all activated slip systems, the unit vector $\underline{s}^{\alpha}$ is the vector tangent to the slip plane α, $\underline{s}^{\alpha}$ corresponds to the slip direction while, $\underline{n}^{\alpha}$ is the vector normal to the slip plane α. The dyadic product between $\underline{s}^{\alpha}$ and $\underline{n}^{\alpha}$ known as Schmidt factor is given by:

$$\mu_{ij}^{(\alpha)} = \frac{1}{2}\left(s_i^{(\alpha)} n_j^{(\alpha)} + s_j^{(\alpha)} n_i^{(\alpha)}\right) \tag{5}$$

The Schmidt factor is used to calculate the resolved shear stress, $\tau^{(\alpha)}$ on the α-*th* slip system, from the stress tensor σ_{ij} as:

$$\tau^{(\alpha)} = \sigma_{ij} \mu_{ij}^{(\alpha)} \tag{6}$$

3.1.3 Constitutive Law

The stress rate $\dot{\sigma}_{ij}$ is related to the elastic strain rate as:

$$\dot{\sigma}_{ij} = L_{ijkl}\dot{\varepsilon}^{e}_{kl} = L_{ijkl}(\dot{\varepsilon}_{kl} - \dot{\varepsilon}^{p}_{kl}) \tag{7}$$

where L_{ijkl} is the elastic moduli tensor.

The plastic slip rate in a slip system α was presented by Hutchinson [58] and Peirce [57] which takes the form of a viscoplastic, power-law expression; it involves a reference strain rate $\dot{\gamma}^{\alpha}_{o}$ and a rate sensitivity exponent *m*, which are material properties. The viscoplastic power-law expression for the plastic strain rate $\dot{\gamma}^{\alpha}$ in a slip system α is given by:

$$\dot{\gamma}^{\alpha} = \gamma^{\alpha}_{o}\ \mathrm{sgn}(\tau^{(\alpha)})\left\{\left|\frac{\tau^{(\alpha)}}{g^{(\alpha)}}\right|\right\}^{m} \tag{8}$$

where $g^{(\alpha)}$ is the strength of each slip system and a functional of the past slip history, i.e., accumulated plastic strains during previous increments of loading.

Equation (8) shows that the strain rate of each slip system α is a function of resolved shear stress $\tau^{(\alpha)}$ and the current slip system strain hardness (strength of slip system) $g^{(\alpha)}$. According to this law (equation (8)), the ratio $\left|\tau^{(\alpha)} / g^{(\alpha)}\right| \leq 1$ [58]. The reason is, the stress state of a deforming elastic-plastic material cannot exceed the yield limit, i.e. stresses will either be inside the yield surface or on the yield surface [58]. Then the rate independent limit $\left(\dot{\gamma}^{\alpha} = const.\right)$ is achieved as *m* gets larger (m = 100): This is because as *m* gets larger the plastic slip rate becomes constant (equal to γ^{α}_{0}), as the ratio of resolved shear stress $\tau^{(\alpha)}$ to current strength $g^{(\alpha)}$ of the slip system α is equal to 1. For the cases when the value of this ratio is less than 1 the large value of exponent *m* reduces this ratio to a very small value making $\dot{\gamma}^{\alpha}$ infinitesimal, i.e. almost no slip in the slip system α. This is particularly useful in order to specify the constant slip rate for the case where the loading rate is constant during all the simulations.

3.1.4 Strain Hardening

In equation (8), the strength of the slip system $g^{(\alpha)}$ characterizes the strain hardening. The evolution of the strength $g^{(\alpha)}$ is given by its rate representation:

$$\dot{g}^{(\alpha)} = \sum_{\beta} h_{\alpha\beta}\dot{\gamma}^{(\beta)} \tag{9}$$

where the matrix $h_{\alpha\beta}$ contains the hardening moduli as shown below; the functional form of $h_{\alpha\beta}$ is determined by the hardening model. Here $h_{\alpha\alpha}$ and $h_{\alpha\beta}$ ($\alpha \neq \beta$) are called self and latent

hardening moduli, respectively. In what follows next, a few of the most prominent hardening models are briefly discussed.

Taylor [54] proposed an isotropic hardening modulus for single crystals given by:

$$h = h_{\alpha\beta} = const. \tag{10}$$

Since h is constant for all slip systems, Taylor's model implies that all the slip systems harden equally. Therefore, the crystal hardens isotropically.

There is little experimental evidence that supports Taylor's model, because this model cannot describe the higher latent hardening effect observed experimentally.

Nakad and Keh [59] proposed a two parameter model (a modification to Taylor's model) to describe the experimentally observed higher latent hardening rate:

$$d\tau_\alpha = H_1 \sum_l d\gamma^l + H_2 \sum_m d\gamma^m \tag{11}$$

with H_1 and H_2 being two material constants. H_1 represents the hardening rate of the primary slip system, while H_2 denotes the hardening rate of other slip systems due to slip in the primary system. This model describes the higher latent hardening rate.

Havner and Shalaby [60] proposed that the higher latent hardening rate, or more generally, the anisotropic hardening of single crystalline deformation is caused by the relative rotation of the crystalline material with respect to the underlying lattice. Without this relative rotation, the hardening would be isotropic. That is, all slip systems will harden equally.

Peirce, Asaro and Needleman [61] pointed out that Havner and Shalaby's [60] simple theory of latent hardening of single crystals predicts very strong latent hardening. They suggested a modified model of latent hardening moduli which gives a less severe latent hardening effect that is more in accord with experimental results, while for self hardening they used the mathematical property of a hyperbolic secant function to reach a peak value of hardening and then saturate, i.e. self hardening starts with a higher initial hardening and vanishes after reaching a saturation resolved shear stress (figure 3). The hardening model is given by:

$$h_{\alpha\alpha} = h(\gamma) = h_o \sec h^2 \left| \frac{h_o \gamma}{\tau_s - \tau_o} \right| \tag{12}$$

$$h_{\alpha\beta} = q h(\gamma) \qquad (\alpha \neq \beta)$$

where, h_0 is the initial hardening modulus, τ_0 the initial yield stress, τ_s the saturation stress, γ the total shear strain in all slip systems, and q the latent to self hardening ratio.

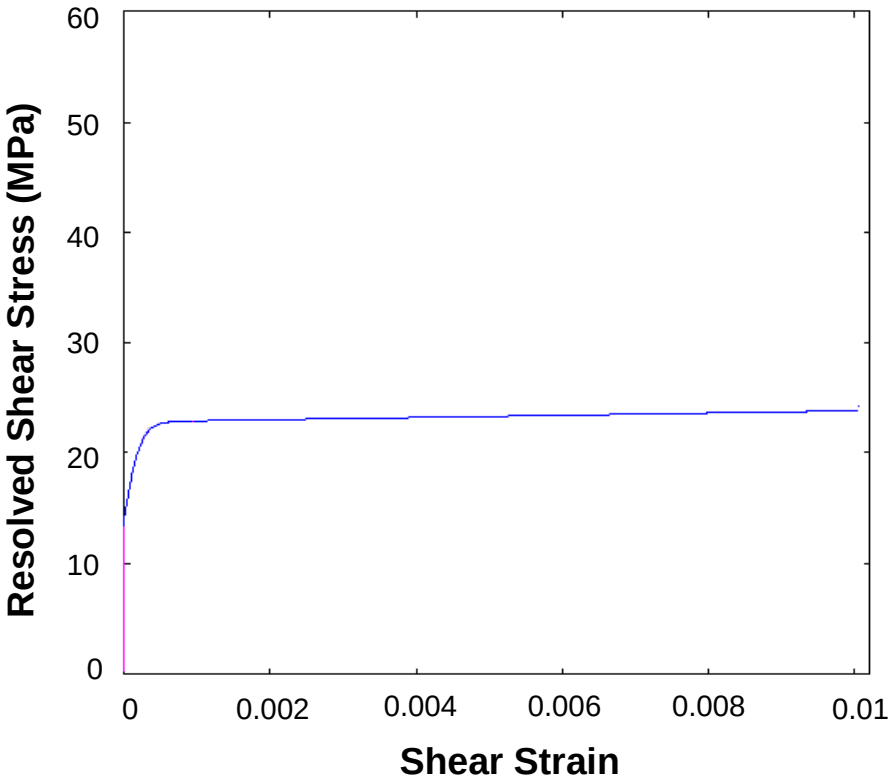

Figure 3: Peirce, Asaro & Needleman (PAN) model [61] for self-hardening of a slip system in single crystalline materials (equation (12)).

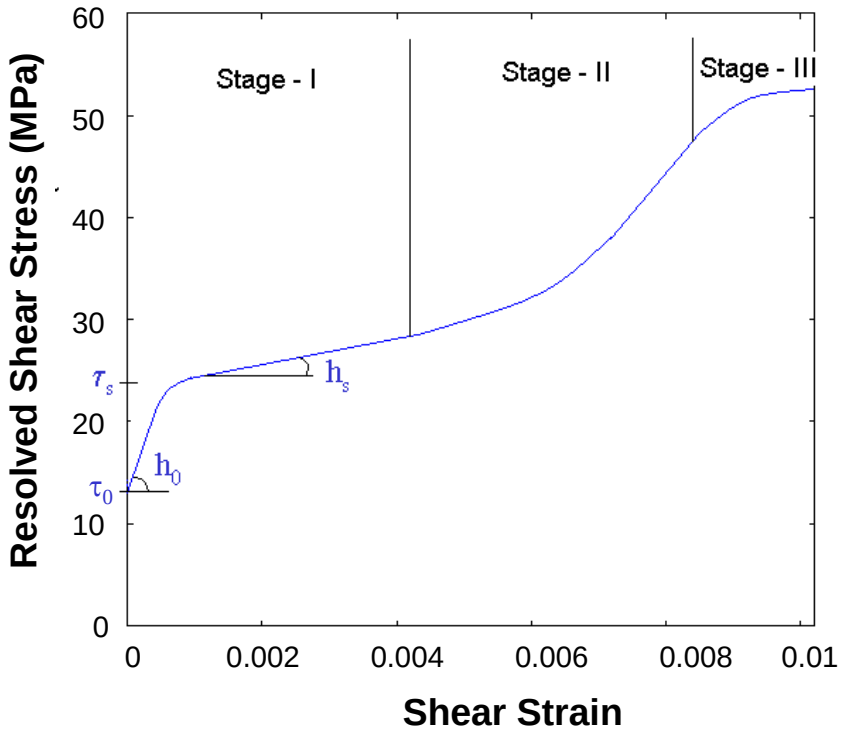

Figure 4: Bassani & Wu (BW) model [62, 63] for self-hardening of a slip system in single crystalline materials (equation (13)).

Bassani & Wu (BW) [62, 63] used a different expression for the hardening modulus to describe the three stages of hardening of crystalline materials. This model is based upon the analytical characterization of hardening moduli at any stage during deformation (figure 4). The expression for self and latent hardening depends on the shear strain γ^{α} of all slip systems:

$$h_{\alpha\alpha} = \left\{ (h_o - h_s)\sec h^2 \left[\frac{(h_o - h_s)\gamma^{\alpha}}{\tau_s - \tau_o} \right] + h_s \right\} G\left(\gamma^{\beta}; \beta \neq \alpha\right)$$

$$h_{\alpha\beta} = q h_{\alpha\alpha} \qquad (\alpha \neq \beta)$$

$$G\left(\gamma^{\beta}; \beta \neq \alpha\right) = 1 + \sum_{\beta \neq \alpha} f_{\alpha\beta} \tanh\left(\gamma^{\beta} \Big/ \gamma_o \right) \tag{13}$$

Here, h_0 is the initial hardening modulus, τ_0 the initial yield stress, τ_s the saturation stress, $\gamma^{(\alpha)}$ the total shear strain in system α, h_s the hardening modulus during stage I deformation, $f_{\alpha\beta}$ the interaction strength between slip system α and β, and $\gamma^{(\beta)}$ the total shear strain in slip system β.

The hardening moduli ($h_{\alpha\alpha}$) are described with an initial hardening modulus (h_0) which saturates after reaching the resolved shear stress (τ_s). This is achieved by using a hyperbolic secant function which has the mathematical property that it starts to decrease as $\gamma^{(\alpha)}$ increases and as the resolved shear stress reaches the value of τ_s the hyperbolic secant function diminishes. After the diminishing of the hyperbolic secant term, the saturation hardening (h_s) specifies that each slip system possesses a finite hardening rate within the easy glide region of the primary slip system. The function G deals implicitly with cross-hardening that occurs between slip systems during stage II hardening.

3.1.5 Dislocation Mechanics based Crystal Plasticity Models

Dislocation mechanics has been used to generate other models, for example those proposed by Cuitino and Ortiz [64], Zikry [66], Ohashi [67], Harder [68], Acharya [70], and Arsenlis and Parks [69]. These models explicitly account for the quantification of dislocation density evolution and the kinetics of dislocation interaction. These types of models involve a large number of parameters and coefficients that must be derived from experiments. In the following, the above mentioned models are discussed briefly.

Cuitino and Ortiz [64] proposed a viscoplastic dislocation mechanics based crystal plasticity model. The model is summarized in box 1.

This model is a statistical mechanical model with a large number of parameters to be identified from experiments. The parameters to be identified for this model are initial strength

g_0 of a slip system, a numerical coefficient η which is a measure for the strength of point obstacles and is constant for a material its value ranges from 0.3 – 0.5, length b of Burgers vector, initial dislocation density ρ_0, a saturation shear strain γ_{sat}, a saturation dislocation density ρ_{sat} at which the rate of annihilation balances the rate of dislocation production, and an interaction matrix $a^{\alpha\beta}$ which can be determined experimentally as shown by Franciosi [65]. Franciosi classifies the interactions according to whether the dislocations belong to the same system (interaction coefficient a_0), fail to form junctions (interaction coefficient a_1), form Hirth locks (interaction coefficient a_2), co-planar junction (interaction coefficient a_3), glissile junctions (interaction coefficient a_4), or sessile Lomer-Cottrell locks (interaction coefficient a_5). According to Franciosi, Hirth locks and Lomer-Cottrell locks are formed when a dislocation from one slip system interacts with the dislocation of another slip slip system at the intersection of the two slip systems. If the lock is formed between two dislocations from two different slip systems with the same Burgers vector magnitude then such a lock is termed as Lomer-Cotrell lock while if the Burgers vector magnitudes are different then the lock is known as Hirth locks.

With this kind of model [64] one ends up with a total number of twelve parameters g_0, η, b, γ_{sat}, ρ_0, ρ_{sat}, $a_0 - a_5$ ($a^{\alpha\beta}$) to be identified from experiments (see box 1).

The crystal plasticity model proposed by Zikry [66] includes the mobile and immobile dislocation densities as internal variables in the constitutive formulation. They derived the relation for the evolution of mobile and immobile dislocation densities that correspond in an average sense to the generation, interaction, trapping, and recovery of dislocations. The evolution equation for mobile and immobile dislocations is given by

$$\dot{\rho}_m^{\alpha} = f\left(\dot{\gamma}^{\alpha}, g_{source}, b, \rho_{im}^{\alpha}, \rho_m^{\alpha}, g_m, H, g_{immob}\right) \tag{14}$$

$$\dot{\rho}_{im}^{\alpha} = f\left(\dot{\gamma}^{\alpha}, g_m, b, \rho_{im}^{\alpha}, g_{immob}, H, g_{re\,cov}\right) \tag{15}$$

where, g_{source} is a coefficient related to an increase in the mobile dislocation density due to dislocation sources, g_m is a coefficient related to the trapping of mobile dislocations due to dislocation interactions, g_{recov} a coefficient related to the rearrangement and annihilation of immobile dislocations, g_{immob} a coefficient related to the immobilization of mobile dislocations, ρ_m^{α} the density of mobile dislocations, ρ_{im}^{α} the density of immobile dislocations and H is the enthalpy of the material at the given temperature. The densities of mobile (ρ_m^{α}) and immobile (ρ_{im}^{α}) dislocations are obtained from equation (14) and (15) by integration

while initial values of these densities are estimated from material charaterization data such as transmission electron microscopy.

The strength g^{α} of the slip system α is defined using a classical form that relates the strength of a slip system to a square-root dependence on the dislocation density.

$$g^{\alpha} = \tau_y^{\alpha} + a_1 \mu b \sqrt{\rho_m^{\alpha}} + a_2 \mu b \sqrt{\rho_{im}^{\alpha}} \tag{16}$$

with, μ the shear modulus, τ_y^{α} the static yield shear stress of slip system α, and a_1 and a_2 the interaction coefficients.

This model requires the identification of seven parameters g_{source}, g_m, g_{recov}, g_{immob}, a_1, a_2, τ_y^{α} for each slip system from uniaxial tension/compression experiments.

Box 1: Crystal plasticity model of Cuitino and Ortiz [64]

Viscoplastic slip rate:

$$\dot{\gamma}^{\alpha} = \begin{cases} \dot{\gamma}_0 \left[\left(\tau^{\alpha} / g^{\alpha} \right)^{1/m} - 1 \right] & \text{If } \tau^{\alpha} > g^{\alpha}; \\ 0 & \textit{otherwise.} \end{cases}$$

Evolution of the shear strength of the slip system α:

$$\dot{g}^{\alpha} = h^{\alpha\alpha} \dot{\gamma}^{\alpha} \text{ (with initial strength } g_0)$$

incremental form of above relation is given as:

$$\Delta g^{\alpha} = \sum_{\alpha} h^{\alpha\alpha} \Delta\gamma^{\alpha} \text{ (with } \Delta g^{\alpha} = g_1^{\alpha} - g_0 \text{ for first increment)}$$

with hardening moduli

$$h^{\alpha\alpha} = h_c^{\alpha} \left(\frac{g^{\alpha}}{\tau_c^{\alpha}} \right)^3 \left\{ \cosh \left[\left(\frac{\tau_c^{\alpha}}{g^{\alpha}} \right)^2 \right] - 1 \right\}$$

where,

$h_c^{\alpha} = \dfrac{\tau_c^{\alpha}}{\gamma_c^{\alpha}}$, $\tau_c^{\alpha} \cong \eta \mu b \sqrt{\pi n^{\alpha}}$, $\gamma_c^{\alpha} \cong \dfrac{b\rho^{\alpha}}{2\sqrt{n^{\alpha}}}$, where η is numerical coefficient ~ 0.3 – 0.5

The density of point obstacles is given as:

$$n^{\alpha} = \sum_{\beta} a^{\alpha\beta} \rho^{\beta}$$

where $a^{\alpha\beta}$ defined by six coefficients $a_0 - a_5$ is an interaction matrix obtained by comparing with experimental stress-strain-curves.

The evolution of the dislocation density is given as:

$$\dot{\rho}^{\beta} = \left(\lambda / b \right) \left(1 - \rho^{\beta} / \rho_{sat} \right) \dot{\gamma}^{\alpha} \Rightarrow \rho^{\beta} = \rho_{sat} \left[1 - \left(1 - \frac{\rho_0}{\rho_{sat}} \right) e^{\left(-\gamma^{\alpha} / \gamma_{sat} \right)} \right]$$

where ρ_{sat} is the saturation density at which the rate of dislocation annihilation balances the rate of production, λ is mean free path between cross gliding and γ_{sat} is saturated shear strain.

Ohashi [67] proposed a model in which the evolution of plastic slip was defined using models of dislocation movement for fcc crystals. The mean free path in this model is defined as a function of the densities of statistically stored as well as geometrically necessary dislocations. This model is scale dependent where the edge and screw components of the geometrically necessary dislocations are obtained from the strain gradients. This model requires eleven parameters to be identified for each slip system from experiments.

Harder [68] proposed a crystallographic model for pure fcc metals in the low temperature range. Rate dependent constitutive equations are based on either isotropic as well as kinematic hardening, whereby the mutual interactions of dislocation processes on the different slip systems are taken into account. This model requires the identification of eleven parameters such as dislocation interactions $a_0 - a_5$, material constant K, y_c the critical annihilation length, ρ_0^r dislocation density at time t = 0 and c, d constants for kinematic hardening and was applied to fcc metals in the past [68].

Arsenlis and Parks [69], and Acharya [70], proposed a continuum constitutive model based on internal variables characterizing crystallographic dislocation densities. The evolution of plastic strain is given by Orowan's relation as a function of dislocation flux and average dislocation velocity. A large number of parameters are to be indentified in this model, approx. 6-18, depending on dislocation interactions. These dislocation interactions can be in-plane interactions or out-of-plane interactions. In-plane interaction means the interaction of dislocations belonging to the slip system parallel to each other while out-of-plane dislocations mean the interaction of dislocations belonging to slip systems which are not parallel to each other.

The above discussion about dislocation mechanics based models leads to the conclusion that these models explicitly account for such things as the quantification of dislocation density evolutions and kinetics of dislocation interactions. On the other hand, these types of crystal plasticity models involve many parameters and coefficients that have to be derived from experiments.

Therefore, dislocation mechanics based crystal plasticity simulations provide a valuable window into the actual micromechanics of how the near-tip plastic deformation develops, and what the actual underlying dislocation distribution is, that corresponds to the macroscopic elastic-plastic deformation pattern. However, limitations on how many dislocations can be handled and how many computer runs can be made, make it difficult to determine the near-tip stress and deformation fields present on a larger scale near a crack tip. This information can be obtained from continuum slip crystal plasticity solutions [38], which give full-field results

for the elastic-plastic stress and deformation fields. Both numerical approaches also accurately show the crack tip opening behaviour, which is important in understanding the type of failure anticipated, see for example [38].

3.1.6 Numerical Implementation

To solve problems with the theory presented in sections (3.1.1 - 3.1.4), the rate equations (4, 7, 8, 9) must be integrated with respect to time, i.e., from stress and strain rates we must generate stresses and strains. As the governing rate equations are highly non-linear, integration is usually achieved incrementally, i.e., going from time t to time t+Δt. Usually, a large number of increments are required to achieve an accurate solution. Stress and other state variables, i.e., plastic slip in each slip system are updated during every increment. Different stress update algorithms are available, such as explicit and implicit stress update algorithms.

Explicit algorithms use information at time t to get to time t+Δt directly. Perhaps the simplest explicit method is the Simple/Forward Euler method [86] which is based on a linearization of the constitutive law of crystal plasticity theory [57, 58] (for details see section 3.1.3) about time t. It is usually easy to implement but it is not very accurate unless very small time steps are used. Another explicit method is the Runge Kutta method [86, 90]. This is a multi-step explicit method based on subdivision of the time step in the form of small time increments.

For an implicit integration algorithm, the state at time t+Δt is determined from information at time t and t+Δt. An example of a fully implicit method is the backward Euler method which is based on a linearization of the constitutive law about time t+Δt. Since the state at t+Δt is unknown, the method usually produces a system of coupled non-linear equations in the stress/state variables at time t+Δt that must be solved to perform the stress/state variable update. The resulting equations can usually be solved using a Newton Raphson iteration scheme. Newton Raphson iteration schemes are generally used to find a root of an equation f(x) = 0: A simple function f(x) can be described using Taylor's expansion near x as:

$$f(x+h) = f(x) + hf'(x) + O(h^2)$$

Starting with an initial guess of the root x, a better guess (x+h) can be obtained using the equation:

$$x + h = x - \frac{f(x)}{f'(x)}$$

Implicit algorithms usually allow larger time increments to be taken than explicit formulations, from the point of view of accuracy and stability, due to the iteration and the shooting for convergence at the end of the time step.

Crystal plasticity theory proposed by Hill [55], Rice [56] and Asaro [57] (for details see section 3.1.2) is implemented in an ABAQUS user subroutine by Huang [90]. This crystal plasticity theory implemented by Huang [90] is based on finite deformation framework. Also it can be used for bcc as well as for fcc materials. An outline of the formulation is given in the following. The governing rate equation written in tensor notation in terms of the Jaumann rate of Cauchy stress, $\overset{\nabla}{\sigma}$ and deformation tensor, $\underline{D}$ is available as a user subroutine (CPMAT) for ABAQUS.

The Jaumann rate of Cauchy stress, $\overset{\nabla}{\sigma}$ is the corotational stress rate on axes that rotate with the crystal lattice, is given by:

$$\overset{\nabla}{\sigma} = \underline{\underline{C}} : \underline{D} - \underline{\sigma}(\underline{I} : \underline{D}) - \sum_{\alpha} \dot{\gamma}^{\alpha} \underline{Y}_{\alpha} \tag{17}$$

with $\underline{\underline{C}}$ representing elasticity tensor, $\underline{I}$ is the identity tensor, $\underline{D}$ is deformation tensor given by:

$$\underline{D} = sym(\dot{\underline{F}} \cdot \dot{\underline{F}}^{-1})$$

where $\underline{F}$ is the deformation gradient and is given by:

$$\underline{F} = \frac{\partial \underline{x}}{\partial \underline{x}'}$$

where $\underline{x}$ are the coordinates of a material point in its deformed state and $\underline{x}'$ are coordinates of a point in the undeformed state.

The deformation gradient tensor $\underline{F}$ keeps information about the true deformation of the body and solid body rotation.

While the Jaumann stress $\underline{Y}_{\alpha}$ is used in order to take into account finite rotations of the loading axes that rotates with the crystal lattice, the orientation tensor $\underline{\mu}_{\alpha}$ describes the orientation of a slip system α in the single crystalline material and the rotation tensor $\underline{\omega}_{\alpha}$ describes the rotation of a slip system α due to the rotation of the crystal lattice. Jaumann stress $\underline{Y}_{\alpha}$, orientation tensor $\underline{\mu}_{\alpha}$ of a slip system α, and rotation tensor $\underline{\omega}_{\alpha}$ of a slip system α are given by:

$$Y_{\alpha} = \underline{\underline{C}} : \underline{\mu}_{\alpha} + \underline{\omega}_{\alpha} \cdot \underline{\sigma} - \underline{\sigma} \cdot \underline{\omega}_{\alpha} \tag{18}$$

$$\mu_{\alpha} = \frac{1}{2}\left(s_{\alpha}^{*} m_{\alpha}^{*} + m_{\alpha}^{*} s_{\alpha}^{*}\right) \tag{19}$$

$$\omega_\alpha = \frac{1}{2}\left(s_\alpha^* m_\alpha^* - m_\alpha^* s_\alpha^*\right) \tag{20}$$

where s_α^* is the vector tangent to slip system α while m_α^* is the vector normal to the slip system α.

In the above equations $\underline{\underline{C}} : \underline{D}$ represents the tensor scalar product (which in the index notation is given by $C_{ijkl} : D_{kl}$) while $\underline{\sigma} \cdot \underline{\omega}_\alpha$ is the tensor product (which in the index notation is given by $\omega_{ik}\sigma_{jk}$).

The rate tangent method (explicit method) [90] is employed to determine the increment of the plastic slip (strain) in slip system α. The rate tangent algorithm is based on estimating the change in shear strain rates during the time increment Δ*t*. The rate tangent algorithm assumes a linear relation among the increments of stresses, strains, resolved shear stress, shear strains and strengths in the slip systems. The increment of the plastic slip (strain) in slip system α is given as:

$$\Delta\gamma_\alpha = \left[(1-\Theta)\dot{\gamma}_\alpha^t + \Theta\dot{\gamma}_\alpha^{t+\Delta t}\right]\Delta t \tag{21}$$

where Θ is an integration constant ranging from 0 to 1 depending on the implicit or explicit method: $\Theta = 0$ in equation (21) corresponds to forward Euler integration which is very simple to implement but is unstable for larger time increments. If $0 < \Theta \leq 1$ is used in equation (21) then it becomes a backward Euler integration scheme which is an implicit scheme. The backward Euler integration scheme is more expensive as compared to forward Euler integration scheme because of the iterative solution but has better stability than forward Euler scheme for larger time increments.

The slipping rate $\dot{\gamma}_\alpha$ in general is a function of the resolved shear stress τ^α and the current strength of slip system α, g^α obtained from equation (9) by integration. The Taylor expansion of the slipping rate gives:

$$\dot{\gamma}_\alpha^{t+\Delta t} = \dot{\gamma}_\alpha^t + \frac{\partial\dot{\gamma}_\alpha}{\partial\tau^\alpha}\Delta\tau^\alpha + \frac{\partial\dot{\gamma}_\alpha}{\partial g^\alpha}\Delta g^\alpha \tag{22}$$

where $\Delta\tau^\alpha$ and Δg^α are the increments of resolved shear stress and current strength in slip system α within the time increment Δt, respectively.

Substitution of equation (22) in equation (21) yields the following incremental relation for plastic strain in slip system α:

$$\Delta\gamma_\alpha = \Delta t\left[\dot{\gamma}_\alpha^t + \theta\frac{\partial\dot{\gamma}_\alpha}{\partial\tau^\alpha}\Delta\tau^\alpha + \theta\frac{\partial\dot{\gamma}_\alpha}{\partial g^\alpha}\Delta g^\alpha\right] \tag{23}$$

In order to implement the incremental theory, the increments of shear strain $\Delta\gamma_\alpha$, resolved shear stress $\Delta\tau^\alpha$, and current strength Δg^α in all slip systems must be derived in terms of the strain increments $\Delta\varepsilon_{ij}$ and the time increment Δt. The so called corotational stress increments $\Delta\sigma_{ij} = \overset{\nabla}{\sigma}\Delta t$ should also be expressed in terms of strain increments $\Delta\varepsilon_{ij}$ as the finite element program always calls the subroutine with an increment of strain $\Delta\varepsilon_{ij}$.

From the general hardening equation of crystalline slip, equation (9), the increments of the current hardening function Δg^α are given as:

$$\Delta g^\alpha = \sum_\beta h_{\alpha\beta}\Delta\gamma_\beta \tag{24}$$

Similarly, the increments of resolved shear stress $\Delta\tau^\alpha$ are related to the strain increments $\Delta\varepsilon_{ij}$ through equation (4 - 7), and are given as:

$$\Delta\tau^\alpha = \left[L_{ijkl}\mu_{kl}^\alpha + \omega_{ik}^\alpha\sigma_{jk} + \omega_{jk}^\alpha\sigma_{ik}\right]\left[\Delta\varepsilon_{ij} - \sum_\beta \mu_{ij}^\beta\Delta\gamma^\beta\right] \tag{25}$$

The corotational stress increments $\Delta\sigma_{ij} = \overset{\nabla}{\sigma}\Delta t$ are given as [90]:

$$\Delta\sigma_{ij} = L_{ijkl}\Delta\varepsilon_{kl} - \sigma_{ij}\Delta\varepsilon_{kk} - \sum_\alpha\left[L_{ijkl}\mu_{kl}^\alpha + \omega_{ik}^\alpha\sigma_{jk} + \omega_{jk}^\alpha\sigma_{ik}\right]\Delta\gamma_\alpha \tag{26}$$

The incremental relations from equation (24) and (25) are substituted in equation (23) yielding the following linear algebraic equations:

$$\sum\left\{\delta_{\alpha\beta} + \theta\Delta t\frac{\partial\dot{\gamma}_\alpha}{\partial\tau^\alpha}\left[L_{ijkl}\mu_{kl}^\alpha + \omega_{ik}^\alpha\sigma_{jk} + \omega_{jk}^\alpha\sigma_{ik}\right]\mu_{ij}^\beta - \theta\Delta t\frac{\partial\dot{\gamma}_\alpha}{\partial\tau^\alpha}h_{\alpha\beta}\,sign\left(\dot{\gamma}_\beta^t\right)\right\}\Delta\gamma_\beta$$

$$= \dot{\gamma}_\alpha^t\Delta t + \theta\Delta t\frac{\partial\dot{\gamma}_\alpha}{\partial\tau^\alpha}\left[L_{ijkl}\mu_{kl}^\alpha + \omega_{ik}^\alpha\sigma_{jk} + \omega_{jk}^\alpha\sigma_{ik}\right]\Delta\varepsilon_{ij} \tag{27}$$

Once the incremental plastic strain $\Delta\gamma_\alpha$ in slip system α is known in terms of the strain increments $\Delta\varepsilon_{ij}$, all other increments of resolved shear stresses, normal stresses and shear strains can be found through equations (25 - 27).

3.2 Fracture Mechanics

The field of fracture mechanics is concerned with the quantitative description of the mechanical state of a deformable body containing a crack or cracks, with a view toward characterizing and measuring the resistance of materials to crack growth [139]. The process of

describing the mechanical state of a particular material or a combination of different materials is to devise a mathematical model of it which can predict the deformation behaviour of the system until it fails. The mathematical model typically consists of an idealized description of the geometrical configuration of the deformable body such as using finite element discretization, an empirical relationship, such as Hooke's law, between internal stress and strains in order to describe the deformation behaviour of the material, and the pertinent balance (equilibrium) laws of physics dealing with mechanical quantities such as stresses, strains and damage [139].

Different criteria have been developed in the past to describe the crack propagation behaviour [29, 39, 71, 72, 101]. In general, they can be classified as stress based criteria [39, 40], energy based criteria [11, 101] and strain based criteria [71]. According to stress based criteria, a crack initiates when a certain stress component ahead of the crack tip reaches a critical value. In the case of energy based criteria, a crack initiates when the energy required to increase the crack length by unity reaches a critical value. One of these energy based criteria is termed as energy release rate and the criterion itself is called maximum energy release rate criterion. One of the most important strain based criteria is based on the crack opening displacement behind the crack tip. According to this criterion a crack initiates when the crack opening displacement at a specified distance behind the crack tip reaches a critical value. All these criteria are discussed in more detail in section 3.3.

For all of these criteria, the fracture energy is an important factor to characterize the crack tip behaviour. In the following, different techniques to compute the fracture energy of a cracking sample are described and compared in the next section. For all the analyses J-integral will be finally used to compute the fracture energy.

3.2.1 Global Energy Method

This method is based on the finite crack extension method and follows the assumption that energy is released when a crack propagates [40]. Then a mathematical expression of the energy release rate is given as:

$$G = -\left(\frac{dU}{dA}\right) \tag{28}$$

where, U is the total energy of the specimens and A is the cracking area (area of the newly created cracked surface). The negative sign is to keep the energy release rate G to be always positive.

Let's assume a cracked finite element model with a crack length of a_k and after deformation the crack length is a_l (figure 5).

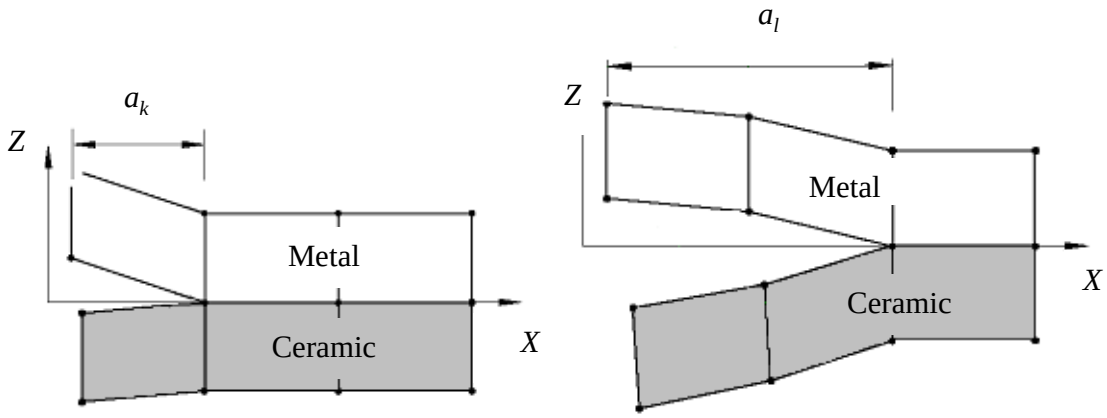

Figure 5: Finite elements with increasing crack length

For this case, the total energy for the specimens with a crack length of a_k is given by:

$$E_{a_k} = \int dt \int dV \sigma_{ij} \dot{\varepsilon}_{ij} \tag{29}$$

From two calculations with a difference in crack length $da = a_l - a_k$, we obtain the energy release rate as follows:

$$G_c = \frac{E_{a_l} - E_{a_k}}{B(a_l - a_k)} \tag{30}$$

3.2.2 Virtual Crack Closure Technique

The virtual crack closure technique (VCCT) is used for computing energy release rates based on results from two and three dimensional finite element analyses to supply the mode separation required when using the energy based mixed-mode fracture criterion [11, 101]. A simple example of such a kind of an energy based fracture criterion is given as (Wang and Suo, 1990; Hutchinson and Suo, 1992):

$$\frac{G_I}{G_I^*} + \frac{G_{II}}{G_{II}^*} = 1 \tag{31}$$

where G_I^* and G_{II}^* are the critical values of the two components of the energy release rates, while G_I and G_{II} are the total areas under the opening and shear traction-separation laws. The two separate components G_I and G_{II} can be calculated by integration of the mode-I and mode-II traction-separation curves (figure 6):

$$G_I = \int_0^{\delta_n} \sigma(\delta_n) d\delta_n \; ; \qquad G_{II} = \int_0^{\delta_t} \tau(\delta_t) d\delta_t \tag{32}$$

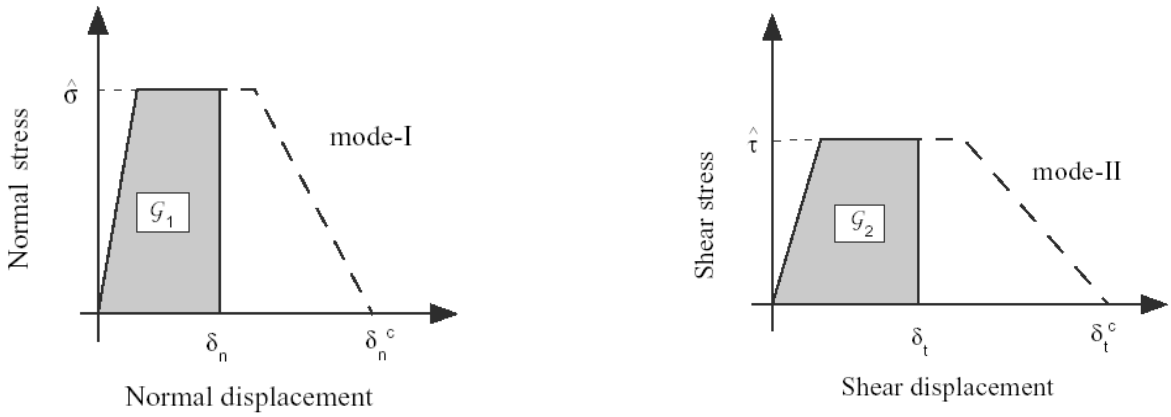

Figure 6: Traction-separation curves for mode I and mode II loading

where δ_n and δ_t denote the normal and tangential displacements.

The method is based on two assumptions:

- The energy released when the crack is extended is identical to the energy required to close the same crack.
- A crack extension of Δa from a+Δa to a+2Δa does not significantly alter the deformation state at the crack tip.

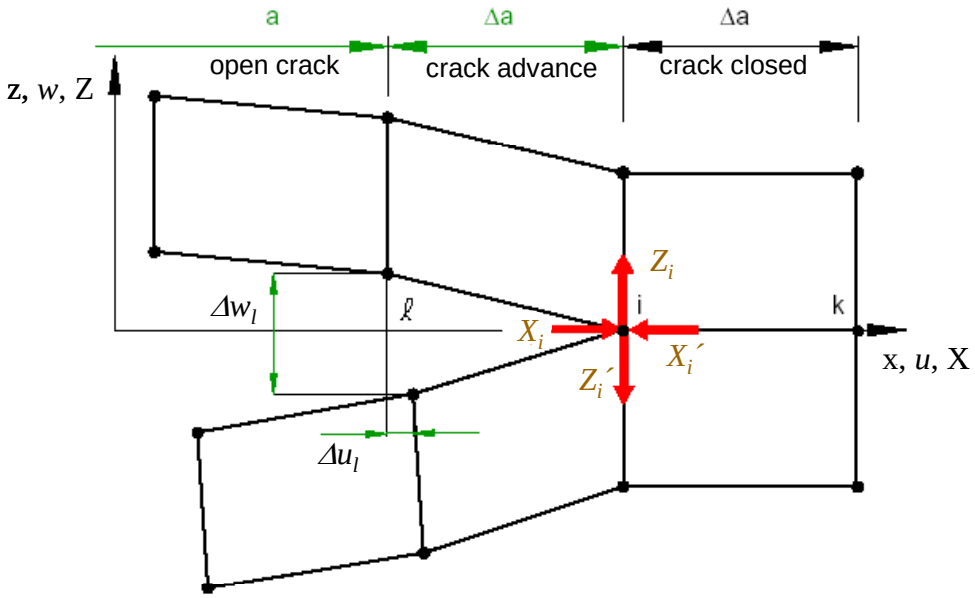

where $X_i' = X_i$ and $Z_i' = Z_i$ from equilibrium

Figure 7: Virtual Crack Closure (VCC) technique

For a crack modelled with two dimensional, four noded elements, as shown in figure 7, the work ΔE required to close the crack along one element sided can be calculated as:

$$\Delta E = \frac{1}{2}\left[X_i \cdot \Delta u_l + Z_i \cdot \Delta w_l\right] \tag{33}$$

where X_i and Z_i are the shear and opening forces at nodal point i, while Δu_l and Δw_l are the shear and opening displacements at node l as shown in figure 7.

For twenty noded solid elements, the equations to calculate the strain energy release rate components at the element corner nodes (location Li) as shown in figure 8 are given below:

$$G_I = -\frac{1}{2\Delta A_L}\left[\frac{1}{2}Z_{Ki}\left(w_{Kl} - w_{Kl^*}\right) + Z_{Li}\left(w_{Ll} - w_{Ll^*}\right) + Z_{Lj}\left(w_{Lm} - w_{Lm^*}\right) + \frac{1}{2}Z_{Mi}\left(w_{Ml} - w_{Ml^*}\right)\right]$$

$$G_{II} = -\frac{1}{2\Delta A_L}\left[\frac{1}{2}X_{Ki}\left(u_{Kl} - u_{Kl^*}\right) + X_{Li}\left(u_{Ll} - u_{Ll^*}\right) + X_{Lj}\left(u_{Lm} - u_{Lm^*}\right) + \frac{1}{2}X_{Mi}\left(u_{Ml} - u_{Ml^*}\right)\right] \tag{34}$$

$$G_{III} = -\frac{1}{2\Delta A_L}\left[\frac{1}{2}Y_{Ki}\left(v_{Kl} - v_{Kl^*}\right) + Y_{Li}\left(v_{Ll} - v_{Ll^*}\right) + Y_{Lj}\left(v_{Lm} - v_{Lm^*}\right) + \frac{1}{2}Y_{Mi}\left(v_{Ml} - v_{Ml^*}\right)\right]$$

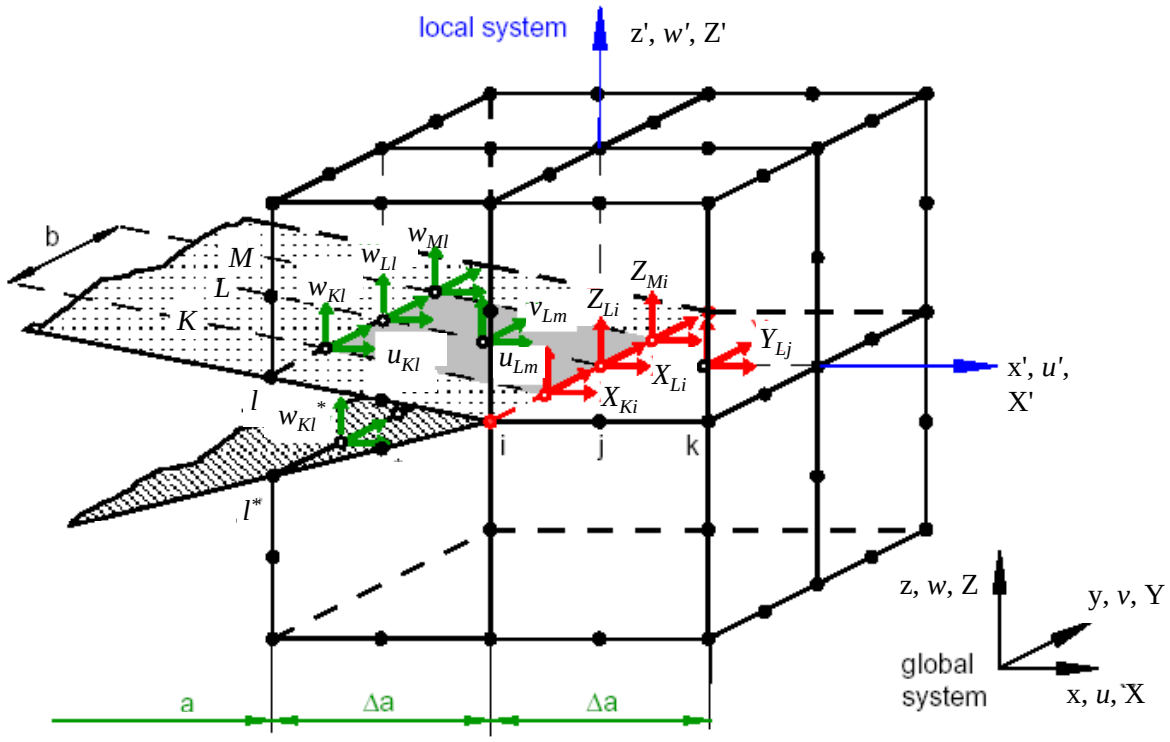

Figure 8: Virtual Crack Closure technique for 20-noded solid elements

3.2.3 J-Integral Method

The J-integral is widely accepted as a fracture mechanics parameter for both linear and nonlinear material response. Cherepanov [12] and Rice [13] introduced path-independent

integrals into fracture mechanics [17]. Rice also showed that this “J-integral” is identical with the energy release rate for a plane crack extension, Δa:

$$J = G = -\left(\frac{\partial U}{\partial a}\right) \tag{35}$$

The J-integral is defined in terms of the energy release rate, i.e., the energy which is released to create a unit area of crack surface, associated with a fictitious small crack advance, Δa, figure 9:

$$J = \frac{1}{\Delta a}\int_{\beta_o}\int \left[\sigma_{ij} u_{j,k} - W\delta_{ik}\right]\Delta x_{k,i}\, dS \tag{36}$$

where Δx_k is the shift of the crack front coordinates from the initial crack tip in x_1 direction, Δa the corresponding increase in crack area and the integration domain β_o is the grey area in figure 9.

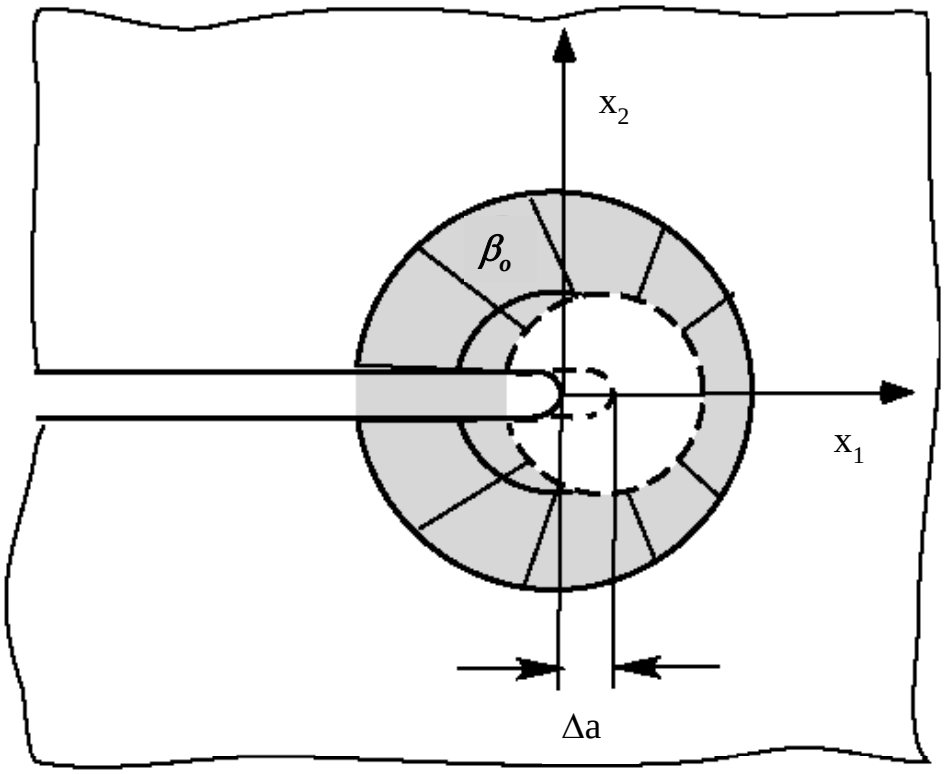

Figure 9: Domain for J-Integral

where i, j, k = 1, 2, 3, W is the external work, σ_{ij} the stress tensor, $u_{j,k}$ the strain, δ_{ik} the Kronecker delta ($\delta_{ik} = 1$ when $i = k$, and $\delta_{ik} = 0$ when $i \neq k$), β_o is the integration domain.

3.3 Crack Growth Criterion

If a critical initiation value of some fracture parameter is exceeded, a crack starts to grow. Crack growth can be simulated by,

- node release techniques, controlled by any fracture mechanics parameter as J-integral, crack tip opening displacement, crack tip opening angle or maximum stress such as the maximum normal stress criterion [39, 40, 71],
- constitutive equations based on damage mechanics concepts like the Gurson model [29, 33], or
- cohesive elements are also being used to simulate the crack growth [72 - 85].

3.3.1 Characteristic Parameters of Node Release Techniques

3.3.1.1 Maximum Stress Criterion

This criteria was introduced by Erdogan [71] for elastic materials, states that the crack propagates in the direction for which the stress is maximum, i.e. when a critical stress criterion at a critical distance ahead of the crack tip is prescribed, then the crack tip nodes are released if the local stress across the interface at a specific distance ahead of the crack tip reaches a critical value [39, 40, 71].

This criterion is typically used for crack propagation in brittle materials [71]. The critical stress criterion is defined as

$$f = \sqrt{\left(\frac{\sigma_n}{\sigma^f}\right)^2 + \left(\frac{\tau_1}{\tau_1^f}\right)^2 + \left(\frac{\tau_2}{\tau_2^f}\right)^2} \tag{37}$$

where σ_n is the normal component of stress carried across the interface at the distance specified; and τ_1 and τ_2 are the shear stress components in shear directions 1 and 2; and σ^f, τ_1^f and τ_2^f are the normal and shear failure stresses.

As mentioned above this criterion is used for crack propagation in brittle materials, thereofore, it is not used for this study as there is always ductility present at the crack tip due to plastic deformation in the metal.

3.3.1.2 Crack tip Opening Displacement Criterion

This criterion is based on the crack opening displacement. The crack tip node is released when the crack tip opening displacement at a specified distance behind the crack tip reaches a critical value.

This criterion is typically used for crack propagation in ductile materials. The crack tip opening displacement criterion is defined as

$$f = \frac{\delta}{\delta_c} \tag{38}$$

where δ is the measured value of the crack tip opening displacement and δ_c is the critical value of the crack tip opening displacement. The crack tip node is released when the fracture criterion reaches the value 1.0.

This criterion can be used in the present study but this does not give any control over the interface strength which is also an important parameter for fracture. It will be shown in this work that macroscopic fracture energy is strongly dependent on the interface strength (maximum stress (σ_c) at which interface fails.

3.3.1.3 Maximum Energy Release Rate Criterion

The strain energy release rate G represents the energy required to increase the crack length by unity. This criterion states that among all admissible crack length displacements, the real increase is the one which maximizes the strain energy release rate [11, 101].

Numerous numerical techniques can be used to compute G. The most commonly used methods are based on global energy release rates [39, 40] and path independent J-integral [12, 13, 17] (see section 3.2.1 & 3.2.3).

3.3.2 Damage Mechanics Approach

Micromechanical modelling of damage and fracture have found increasing interest in order to study the damage in metal matrix composites [29, 33]. The general advantage, compared with classical fracture mechanics, is that, in principle, the parameters of the respective models depend only on the material. Also, it is not even necessary to consider specimens with an initial crack [29].

For crack growth simulations using a damage mechanics approach, the constitutive equations introduce a damage parameter D as a function of stresses and strain. The failure initiates as soon as the damage parameter D becomes unity. Crack propagation is represented in terms of element softening or removal when the damage parameter reaches a critical value.

3.3.3 The Cohesive Model

Cohesive models have found increasing interest to simulate fracture in metallic, polymeric, and ceramic materials and their composites [72 – 85]. Using cohesive models, the fracture can

be simulated for any structure with or without a crack. The idea for the cohesive model is based on the consideration that the fracture mechanics analysis presupposes the existence of an infinitely sharp crack leading to singular crack tip fields. However, in real materials neither the sharpness of the crack nor the stress levels near the crack tip region can be infinite. Barenblatt [72, 73] and Dugdale [74] were the first ones to propose the concept of cohesive model to overcome these difficulties.

Barenblatt [72, 73], who investigated the fracture of brittle materials, defined the traction along the crack path as a function of the crack tip distance along the crack front. The typical traction-crack tip distance is shown in figure 10(a).

Dugdale [74] introduced the finite stress at the crack tip to be the yield stress, which is not true always as the crack-opening stress can be much higher than the yield stress. The typical curve is shown in figure 10(b).

Needleman [75, 76] was the one of the first to use polynomial and exponential types of traction-separation equations to simulate the particle debonding in metal matrices. The exponential fit is used for normal traction while trigonometric fit for shear traction. The traction-separation curves are plotted in figure 10(c). Xu and Needleman [77, 78] further used the above models to study the void nucleation at the interface of particle and matrix metal.

Tvergaard and Hutchinson [79] used a trapezoidal shape of the traction-separation model to calculated the crack growth resistance in elasto-plastic materials. The typical curve is shown in figure 10(d). Tvergaard [80] also extended the the Needleman [75] model of pure normal separation for mixed-mode loading. This is one of the most popular cohesive laws used by many authors (e.g., Chaboche [81]). The typical curve is shown in figure 10(d).

Camacho and Ortiz [82] employed a linear cohesive fracture mode to propagate multiple cracks along arbitrary paths during impact damage in brittle materials. This model predicts failure by both shear and normal separation in tension and by shear separation in compression. The typical curve is plotted in figure 10(f).

Geubelle [83] utilized a bilinear cohesive model to simulate spontaneous initiation and propagation of cracks in thin composite plates subjected to low-velocity impact. The traction separation curves for this model are shown in figure 10(g).

A more versatile cohesive law is proposed in Scheider [84,85], which fulfils the following requirements:

- The initial stiffness of the cohesive element can be varied;
- A region can be defined, where the traction in the cohesive element is kept constant;
- The curve must be continuously differentiable for numerical reasons.

This has been achieved by using two additional parameters δ_1 and δ_2 (figure 10(e)), leading to the following formulation for the function $T(\delta)$:

$$\sigma = \sigma_c \begin{cases} 2\left(\frac{\delta}{\delta_1}\right) - \left(\frac{\delta}{\delta_1}\right)^3 & \delta \le \delta_1 \\ 1 & \delta_1 \le \delta \le \delta_2 \\ 2\left(\frac{\delta - \delta_2}{\delta_c - \delta_2}\right)^3 - 3\left(\frac{\delta - \delta_c}{\delta_c - \delta_2}\right)^2 + 1 & \delta_2 \le \delta \le \delta_c \end{cases} \quad (39)$$

This law is similar to the multilinear cohesive law proposed by Tvergaard and Hutchinson [79], who also introduced two additional parameters, but without requirement that the curve is continuously differentiable.

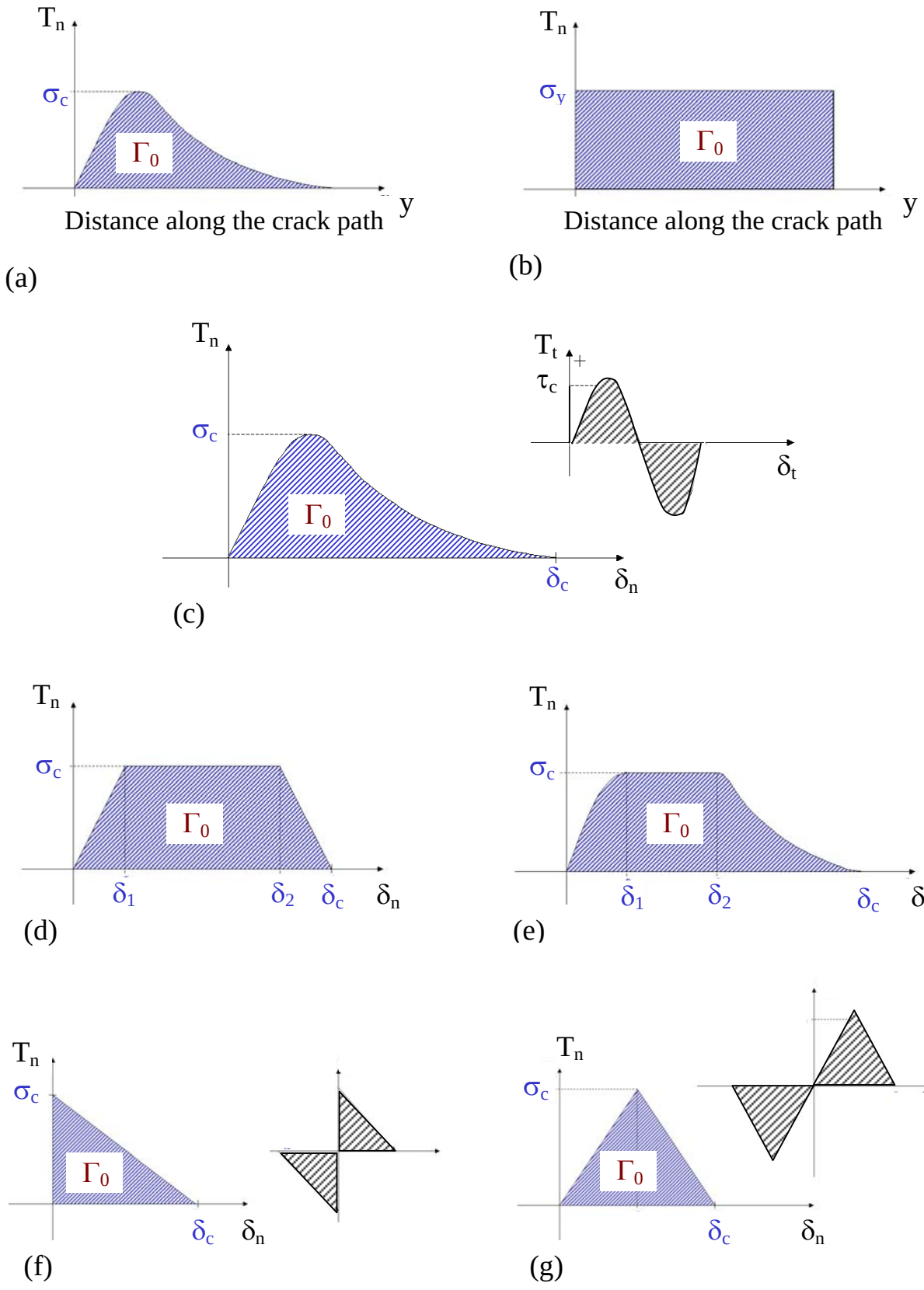

Figure 10: Various cohesive laws proposed by different authors: (a) Barenblatt [72]; (b) Dugdale [74]; (c) Needleman [77]; (d) Tvergaard & Hutchinson [79]; (e) Scheider [84]; (f) Camacho & Ortiz [82]; (g) Geubelle [83]

In all the cohesive models (excluding Dugdale's model and Camacho's model), the traction-separation relations for interfaces are such that with increasing interfacial separation, the traction across the interface reaches a maximum, then decreases and eventually vanishes, permitting complete decohesion. The main difference among all the cohesive models lies in the shape of the traction-separation response, and the constants that are used to describe this shape. The cohesive models can be described by two independent parameters. These parameters may be two of the three parameters, namely the cohesive energy also known as work of adhesion (W_{adh}), and either of the cohesive strength (σ_c) or the separation length (δ_c). Cohesive strength (σ_c) is the maximum stress (traction) value at which damage initiates while separation length (δ_c) is the amount of separation at which the interface completely fails.

Throughout this work δ_1 and δ_2 are chosen by comparing the initial and final slopes of the cohesive law curves of Xu and Needleman [77, 78], as shown in figure 11. This cohesive law curve has been used by Xu and Needleman [78] and Kysar [35, 36] for copper/alumina bicrystal interfaces. These values are found to be $\delta_1 = 0.05\delta_c$ and $\delta_2 = 0.1\delta_c$.

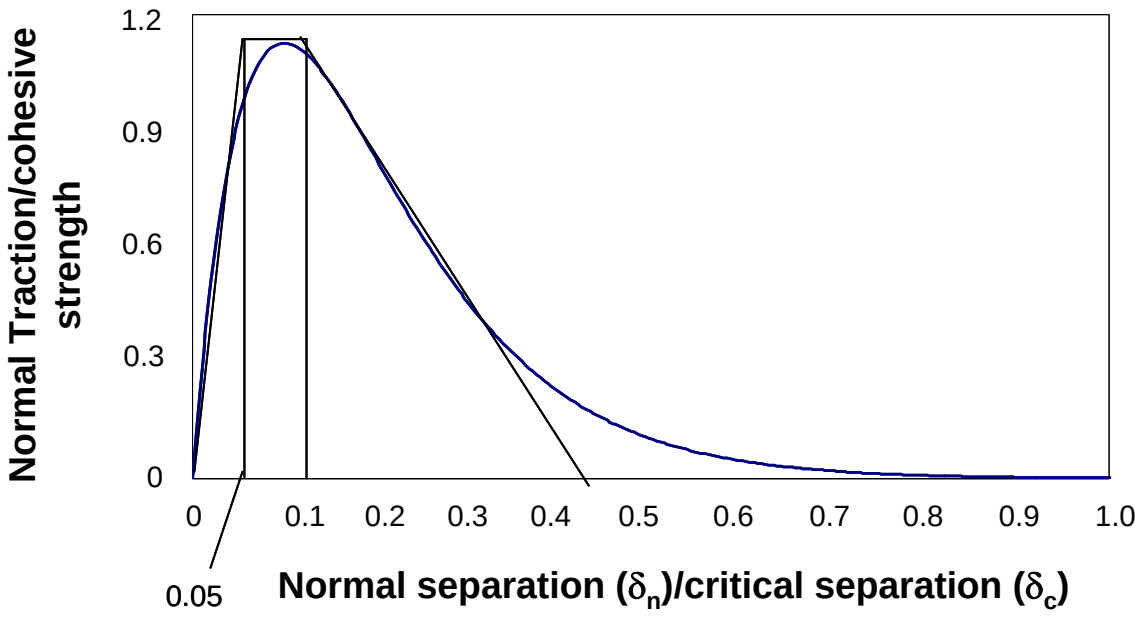

Figure 11: Cohesive law curve of Xu and Needleman [77, 78]

3.4 Finite Element Method (FEM)

The finite element method (FEM) is a general numerical scheme for obtaining approximate solutions to boundary and initial value problems. The FEM is used when no analytical solution exists for a given problem, e.g. for complex geometries or boundary conditions.

Therefore, the basic characteristic of the FEM is the spatial discretization of an arbitrary geometry into an assembly of simply shaped elements which are connected at their common

nodes and which do not overlap. These areas are referred to as finite elements or subdomains. The shape and size of the finite elements may depend on a number of factors, for instance on the geometry of the given sample.

In the following, the finite element method (FEM) is outlined for the case when displacement fields are the primary (master) variables to compute strains and stresses.

As discussed above the spatial domain β_0 is decomposed in finite elements.

In the description of the elements, a displacement field can be obtained using so called shape function $\underline{N}(x)$.

The FE-Ansatz is:

$$\underline{u}(x) = \underline{N}(x)\underline{d}^{e} \tag{40}$$

Where $\underline{d}^{e}$ represents the nodal displacements in the element *e*. The shape functions $\underline{N}(x)$ are related to the nodes and are 1 at the node location and 0 at all neighbouring nodes. Since the finite element method approximates the real course of the considered state variables in each element by a polynomial Ansatz the elements must thus be the smaller the simpler these functions are. The use of higher order polynomials usually allows the employment of larger finite elements. Thus, the element size depends also on the chosen polynomial Ansatz functions. Finally, the element size must be reduced in regions where strong gradients of the primary (master) variable are expected.

The finite element discretization transforms a continuous boundary value problem into an algebraic system of equations for the discrete nodal displacements of a given finite element mesh.

The following four steps are gone through to transform a boundary value problem (BVP) into an algebraic system of equations:

(i) Setup the boundary value problem in its strong form consisting of partial differential equation (PDEs) and boundary conditions (BCs). With the known prescribed displacements (dirichlet boundary condition) the strains that are induced in the structure are computed using kinematic relations given as:

$$\underline{\varepsilon} = \underline{u}' \tag{41}$$

These computed strains are then used to compute the stresses induced in the structure due to deformation by using material equations given as:

$$\underline{\sigma} = \underline{\underline{C}} : \underline{\varepsilon} \tag{42}$$

where $\underline{\underline{C}}$ is the elasticity tensor, and $\underline{\varepsilon}$ are elastic strains.

These stresses $\underline{\sigma}$, the density ρ and the body forces $\underline{b}$ are then used to construct the equilibrium conditions using:

$$\underline{\sigma}' + \rho \underline{b} = \underline{O} \tag{43}$$

(ii) The strong form of the boundary value problem in equation (43) is then used to construct the weak form of the problem by the Galerkin concept. This is done by introducing a field of test functions $\delta u(x)$. A test function $\delta u(x)$ is an arbitrary, vector valued function, and must be chosen in such a way that it obeys any prescribed kinematic constraints, such as displacement boundary conditions. This introduction of $\delta u(x)$ in the strong form of a partial differential equation (43), which describes the equilibrium condition of the structure, yields the Galerkin type weak form of the boundary value problem to simulate the deformation behaviour of the structure.

$$G(u, \delta u) = \int_B \underline{\sigma} \delta \varepsilon dV - \int_B \rho \underline{b} \delta u dV - \int_{\partial B_t} \bar{t} \delta u dA \tag{44}$$

This expression is also called the principle of virtual work. The first term is the total internal energy of the system, the second term is the energy stored due to the body forces and the third term is the work done by the externally applied forces $\bar{t}$, where $\underline{\sigma}$ is the stress tensor, ρ the density, $\underline{b}$ the body forces, $\delta\varepsilon$ the strains obtained from displacement test functions, and δu are the displacement test functions. Also, B represents the domain of the continuum and ∂B_t the traction boundary.

(iii) Discretize the weak form based on FE-Ansatz. The weak form of equation (44) is discretized by inserting the FE-Ansatz:

$$\underline{u}(x) = \underline{N}(x) \underline{d}^e \tag{45}$$

into equation (44) where $\underline{N}(x)$ is the FE-Ansatz, and $\underline{d}^e$ are the nodal displacements. The insertion of above in the weak form (44) gives for a boundary value problem:

$$G(u, \delta u) = \mathop{\mathrm{A}}_{e=1}^{n_{elem}} \delta \underline{d}^{eT} \left\{ \int_{B^e} \underline{B}^T \underline{\sigma} dV - \int_{B^e} \underline{N}^T \rho \underline{b} dV - \int_{\partial B_t} \underline{N}^T \bar{t} dA \right\} = 0 \tag{46}$$

where A denotes the finite element assembly operator. This assembly operator assembles the system of equations, i.e. equation (44) for each element and forms an equation as given in (46).

The terms in equation (46) can be classified as internal and external forces. The first term consists of the forces due to the induced stresses $\underline{\sigma}$ and they are called internal

nodal forces (equation (47) while the forces due to the body forces ρ and traction (forces acting on the surface of the structure) boundary conditions $\bar{t}$ are called external nodal forces (equation (48)):

$$\underline{f}_{\text{int}}^{e} = \int_{B^e} \underline{B}^T \sigma dV \tag{47}$$

$$\underline{f}_{ext}^{e} = \int_{B^e} \underline{N}^T \rho b dV + \int_{\partial B_t} \underline{N}^T \bar{t} dA \tag{48}$$

Using the above representation of internal and external nodal forces, equation (46) simplifies to:

$$\underline{f}_{ext} = \underline{f}_{\text{int}} \tag{49}$$

For static problems, the algebraic finite element equations (47) and (48) provide an equilibrium between internal and external nodal forces (as shown in equation (49)).

(iv) The algebraic system of equations obtained by the FE-method is solved by an iterative scheme, such as Newton's method [86] already discussed in section 3.1.6.

All simulations on niobium/alumina bicrystal specimens during this work are performed with the help of finite element software ABAQUS.

4. Results

4.1 Material Parameter Identification of Single Crystalline Niobium

This section describes the material parameters identification procedure for single crystalline niobium using experimental stress-strain curves. The material parameters identified using crystal plasticity theory (as discussed in section 3.1), are hardening parameters of different slip systems activated during deformation.

4.1.1 Introduction

Due to high ductility, good formability, slow work hardening, and high electrical and thermal conductivity, niobium is frequently used in microelectronic devices, aerospace and automotive industry. Some specific uses are pressure ports in rocket boosters, lighting filaments in sodium vapour lamps and ceramic insulators, and metal wire interfaces in integrated circuits. In all these applications of metal/ceramic interfaces, the metal shows elastic-plastic behaviour due to mechanical or thermomechanical loading. Therefore, for all these applications the deformation behaviour of the metal (niobium) is always important for their performance. The crystallographic approach to study the deformation behaviour of single and polycrystalline materials provides an improved framework with respect to the classical macroscopic models to predict the stress-strain behaviour of crystalline material. Crystal plasticity models have been mostly used for face-centered-cubic (fcc) crystals [63, 91, 94]. The reason behind it is the large number of slip systems. Body centered cubic (bcc) crystals possess 48 slip systems as compared to the 12 slip systems of fcc crystals. Therefore, interdependence of the crystal parameters of each family of slip system for bcc crystal makes the identification of crystal parameters, such as yield stress and strain hardening moduli of slip systems, complicated. In what follows next, we describe a way to identify those parameters.

Conventional crystal plasticity theory [55 - 57] (as discussed in section 3) has been used to study the deformation behaviour of single crystalline niobium. In order to validate the simulated stress-strain-curves and experimental stress-strain-curves of single crystalline niobium, two different hardening models of Peirce, Asaro and Needleman (PAN) [61] and Bassani & Wu (BW) [62 – 63] (as previously discussed in section 3.1.4) for slip system hardening have been used. It will be shown in section 4.1.5 that only the Bassani & Wu (BW) [62 - 63] model is able to simulate the three stage hardening during the deformation of niobium single crystalline material.

4.1.2 Strain Hardening Models

Peirce, Asaro, and Needleman (PAN) [61], proposed a model that provides latent hardening - an effect that is more in accord with the experimental results, while for self hardening they used the mathematical property of the hyperbolic secant function to reach a peak value of hardening and then saturate, i.e. self hardening starts with a higher initial hardening and vanishes after reaching a saturation resolved shear stress (figure 12). The hardening model is given by the following expressions for self and latent hardening:

$$h_{\alpha\alpha} = h(\gamma) = h_o \sec h^2 \left| \frac{h_o \gamma}{\tau_s - \tau_o} \right|$$
$$h_{\alpha\beta} = q h(\gamma) \qquad (\alpha \neq \beta) \tag{50}$$

where, h_0 is the initial hardening modulus, τ_0 the initial shear yield stress, τ_S the shear saturation stress, γ the total shear strain in all slip systems, and q the latent to self hardening ratio.

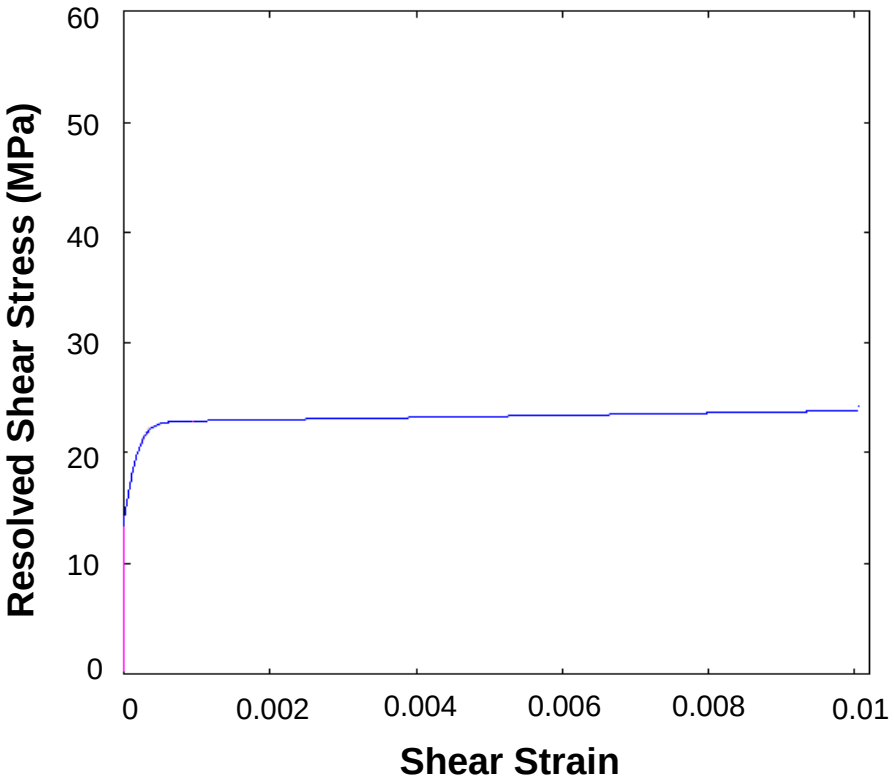

Figure 12: Peirce, Asaro & Needleman (PAN) model for self-hardening of a slip system in single crystalline materials.

Bassani & Wu (BW) [62 - 63] used different expressions for the hardening moduli to describe the three stages of hardening of crystalline materials. This model is based upon the analytical cha-

racterization of the hardening moduli at any stage (I, II and III) during deformation (figure 13). This hardening law can model all three stages of hardening during the deformation of a single crystalline material.

The expressions for self and latent hardening depend on the shear strains γ^{α} of all slip systems α:

$$h_{\alpha\alpha} = \left\{ (h_o - h_s)\sec h^2 \left[\frac{(h_o - h_s)\gamma^{\alpha}}{\tau_s - \tau_o} \right] + h_s \right\} G\left(\gamma^{\beta}; \beta \neq \alpha\right)$$

$$h_{\alpha\beta} = q h_{\alpha\alpha} \qquad (\alpha \neq \beta) \tag{51}$$

$$G\left(\gamma^{\beta}; \beta \neq \alpha\right) = 1 + \sum_{\beta \neq \alpha} f_{\alpha\beta} \tanh\left(\gamma^{\beta} / \gamma_o \right)$$

where, $g^{(\alpha)}$ is the total shear strain in system α, h_S the hardening modulus during stage I deformation, $f_{\alpha\beta}$ the interaction strength between slip system α and β during stages II and III hardening (see figure 13), and γ^{β} is the total shear strain in slip system β.

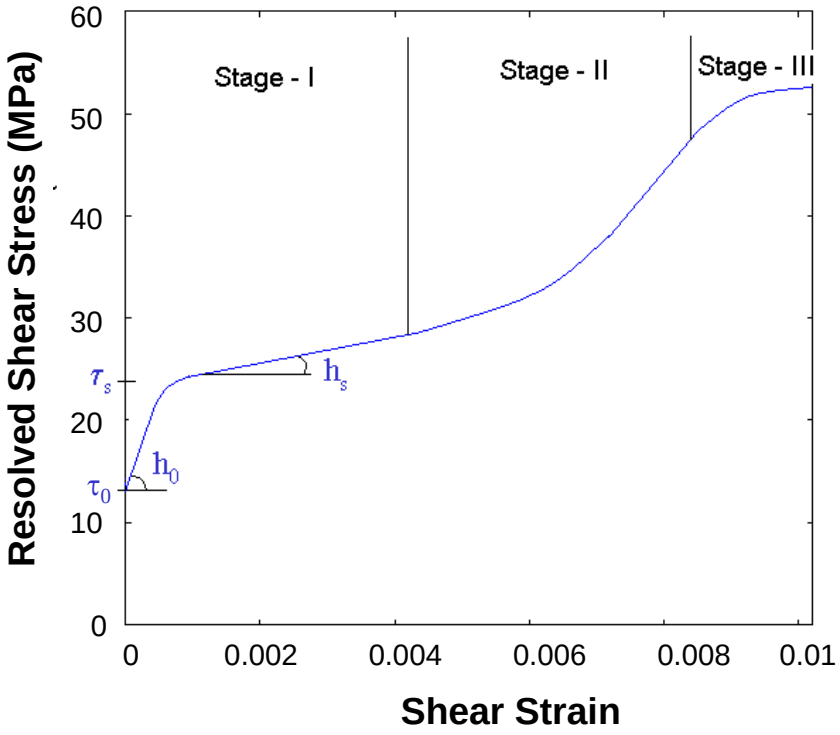

Figure 13: Bassani & Wu (BW) model for self-hardening of a slip system in single crystalline materials.

The hardening moduli are described with an initial hardening (h_0) which saturates after reaching the resolved shear stress (τ_s). After the diminishing of the hyperbolic secant term, the saturation hardening term (h_s) specifies that each slip system possesses a finite hardening rate

equal to h_s. The function G deals implicitly with cross-hardening that occurs between slip systems during stages II and III hardening.

As mentioned in section 3.1.6, the crystal plasticity theory along with the two hardening laws by Peirce, Asaro and Needleman (PAN) [61] and Bassani & Wu (BW) [62 - 63], respectively has been implemented numerically within the UMAT written by Huang [90]. This UMAT subroutine has been used with the finite element package ABAQUS [86] for the present work.

4.1.3 Deformation Behaviour of Niobium Single Crystals

Niobium in single crystalline form exists as a body-centered-cubic (bcc) crystal (see figure 14(a)). It is a well known fact that bcc crystals generally possess three families of slip systems, i.e., (110)[111]-type, (112)[111]-type and (123)[111]-type in which plastic slip can occur during plastic flow. The slip systems are shown in figures 14 (b - d).

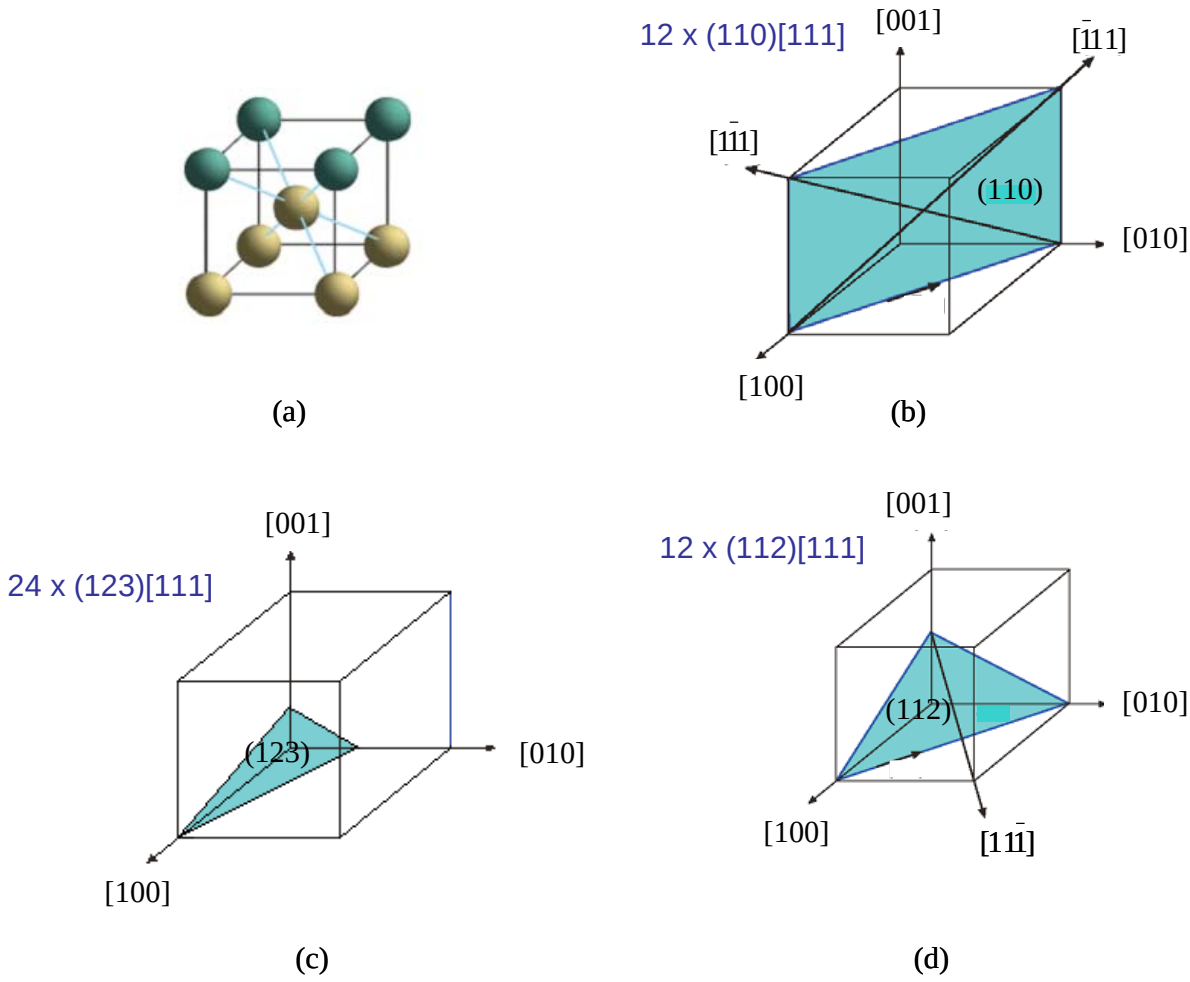

Figure 14: (a) Body centered cubic (bcc) crystal with (b - d) three types of glide planes and 48 slip systems in total

Experimental studies of the deformation behaviour of niobium single crystals have been performed by many researchers. Mitchell [92] showed that a niobium single crystal shows the

three stage hardening like face-centered-cubic (fcc) crystals. He studied the deformation behaviour of niobium single crystals for various orientations, as well as effects of impurities, temperature and strain rate. His results show that an increasing volume fraction of impurities increases the initial flow stress, a decreasing temperature increases the initial flow stress and an increasing strain rate increases the initial flow stress.

Bowen [88], Duesbery and Foxall [89], Anglada and Guiu [87] also studied the deformation behaviour of niobium single crystals and concluded the same results. Moreover, in all cases studied plastic slip was observed in the (110)[111] and (112)[111] slip systems while slip in the (123)[111] system is only promoted in the case when substitutional impurities such as oxygen, aluminium, copper, etc were present. Resolved shear stress vs. shear strain curves [88] for (-101)[111] and (-211)[111] slip systems are plotted in figure 15 for two different tensile axis orientations. Figure 15 (a) shows the resolved shear stress vs. shear strain curve for tensile axis orientation BI (Or BI) for which the (-101)[111] slip system is the primary activated slip system. figure 15 (b) shows the plot of resolved shear stress vs. shear strain curve for tensile axis orientation BII (Or BII) for which the (-211)[111] slip system is the primary activated slip system.

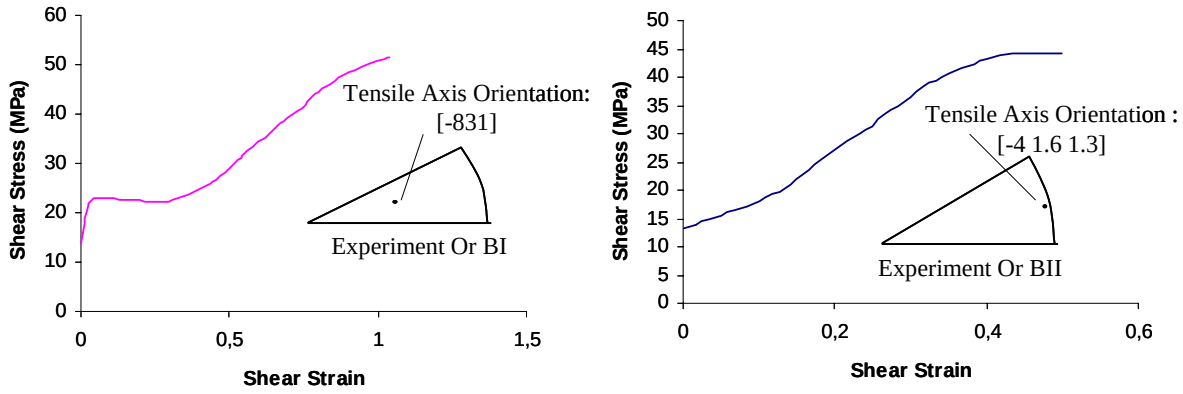

(a) (b)

Figure 15: Resolved shear stress vs. shear strain for (a) (-101)[111] and (b) (-211)[111] slip system

4.1.4 Modelling

All simulations are done using the crystal plasticity theory [55 - 57] implemented in the finite element method (as discussed in section 3.4). Finite element simulations are performed by constructing a finite element model of the specimens used in experimental studies with 2nd order, reduced integration elements (C3D20R), which is available in ABAQUS [86] (figure 16). The crystal plasticity theory [55 - 57] as described in section 3.1 and implemented as user subroutine [90] in the finite element package ABAQUS [86] is used for all the simulations.

Tension tests are simulated using displacment controlled analysis with the same strain rate (1.3×10^{-3} sec^{-1}) as used in experiments.

For introducing the tensile loading boundary conditions, a constant displacement rate is specified in the axial direction for all nodes on one of the circular surfaces of the rod shaped specimens, e.g. on the right of the mesh (3-direction). At the left of the specimens mesh, the axial displacements are constrained to be zero. The lateral displacements on both left and right are not constrained (with the exception of one node on the left constrained to have zero lateral displacement in order to ensure uniqueness of the solution).

The elastic properties of niobium single crystals are defined using bcc symmetry (Table V).

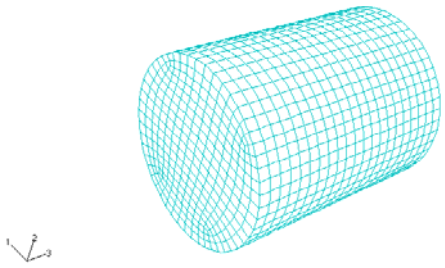

Figure 16: Finite element mesh of a niobium specimens

Table V: Elastic Properties of single crystalline niobium

	C_{11} (MPa)	C_{12} (MPa)	C_{44} (MPa)
Nb Single Crystal	245500	134000	28700

4.1.5 Results and Discussion

The identification of the hardening parameters of single crystalline niobium is based on the assumption that each family of slip systems possesses the same σ-ε-behaviour. For the Peirce, Asaro and Needleman [61] type hardening model the material parameters involved are h_o, τ_o, and τ_s for each family of slip systems and as for the case of niobium single crystals there will be two sets of parameters, i.e. one set of three prameters for the (110)[111] slip system and a second set of three parameters for the (112)[111] slip system. Therefore, altogether six parameters will be required for niobium single crystals. These six parameters can directly be read from the resolved shear stress vs. shear strain curves of each (110) and (112) type slip system, if available.

The simulation results of the uniaxial tension test (described in section 4.1.4) using the Peirce, Asaro and Needleman (PAN) [61] model is shown in figure 17 for the orientation where the (-101)[111] slip system is activated. The slip system is activated when the resolved shear stress

in slip system (-101)[111] becomes 13.7 MPa. The set of parameters used for the two families, i.e. (110)[111] and (112)[111] is given in table VI:

Table VI: Parameters used for the Peirce, Asaro and Needleman (PAN) [61] model

	τ_o (MPa)	τ_s (MPa)	h_o (MPa)
(110)[111]	13.7	16.4	292.26
(112)[111]	7.88	9.1	49.03

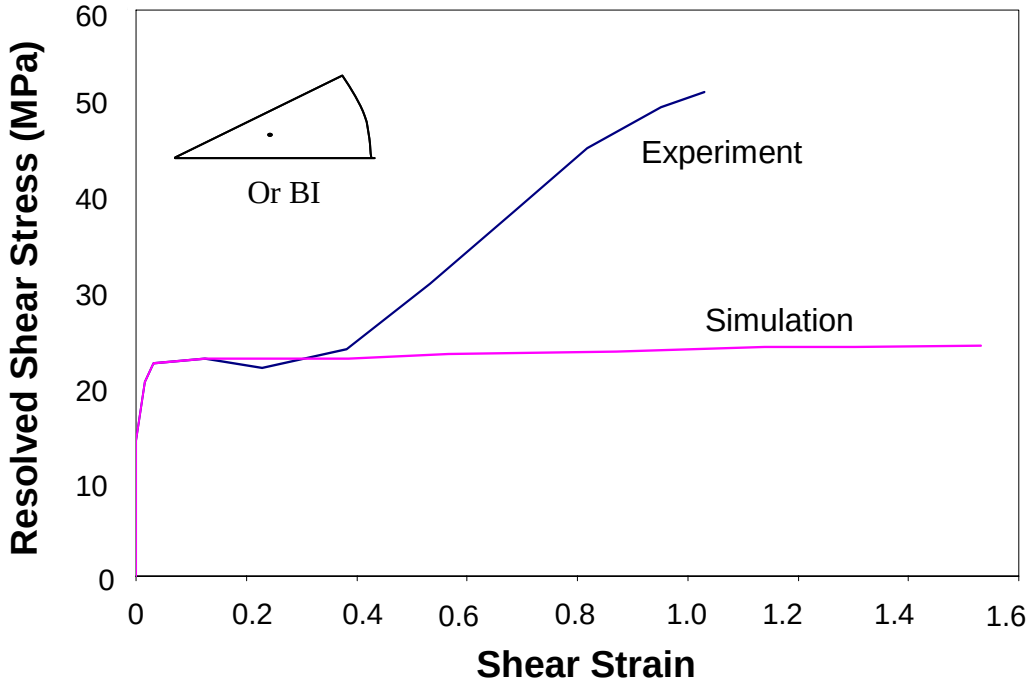

Figure 17: Hardening curves for the (-101)[111] slip system

As discussed before and as it is also evident from the above result the resolved shear stress saturates after a specific value of plastic slip γ. Therefore, this hardening model can only be used if the maximum deformation state is in a single glide region, i.e. no secondary slip system is activated.

To simulate three stage hardening, the Bassani & Wu (BW) model is used (see section 3.1.4). There were 10 material parameters identified for each family of slip systems, i.e. h_o, h_s, τ_o, τ_s, γ_o, γ_{oI}, $f_{\alpha\beta}$, $f_{\alpha\beta I}$, q, q_I. In total, 20 parameters are identified for both (110) and (112) type slip systems. h_o, h_s, τ_o, τ_s (see figure 13) are identified directly from the single crystal stress strain curves in figure 15. The rest of the six parameters (γ_o, γ_{oI}, $f_{\alpha\beta}$, $f_{\alpha\beta I}$, q, q_I) include four interaction parameters (γ_o, γ_{oI}, $f_{\alpha\beta}$, $f_{\alpha\beta I}$) of each family of slip systems when it interacts with a slip system of the same family (γ_o, $f_{\alpha\beta}$) or with a slip system of the other family (γ_{oI}, $f_{\alpha\beta I}$).

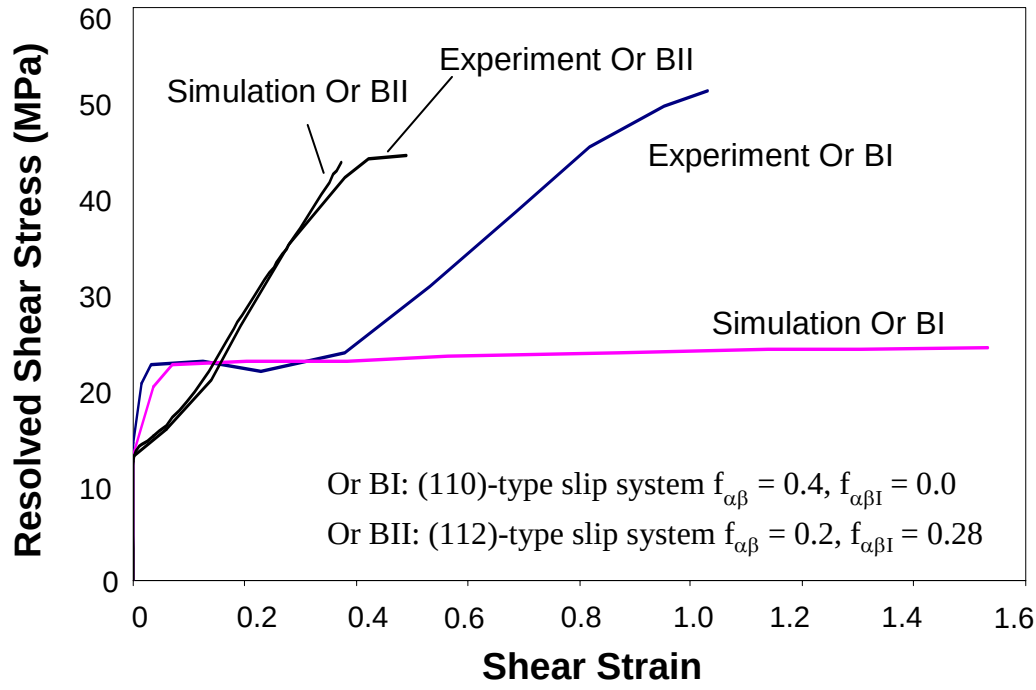

(a)

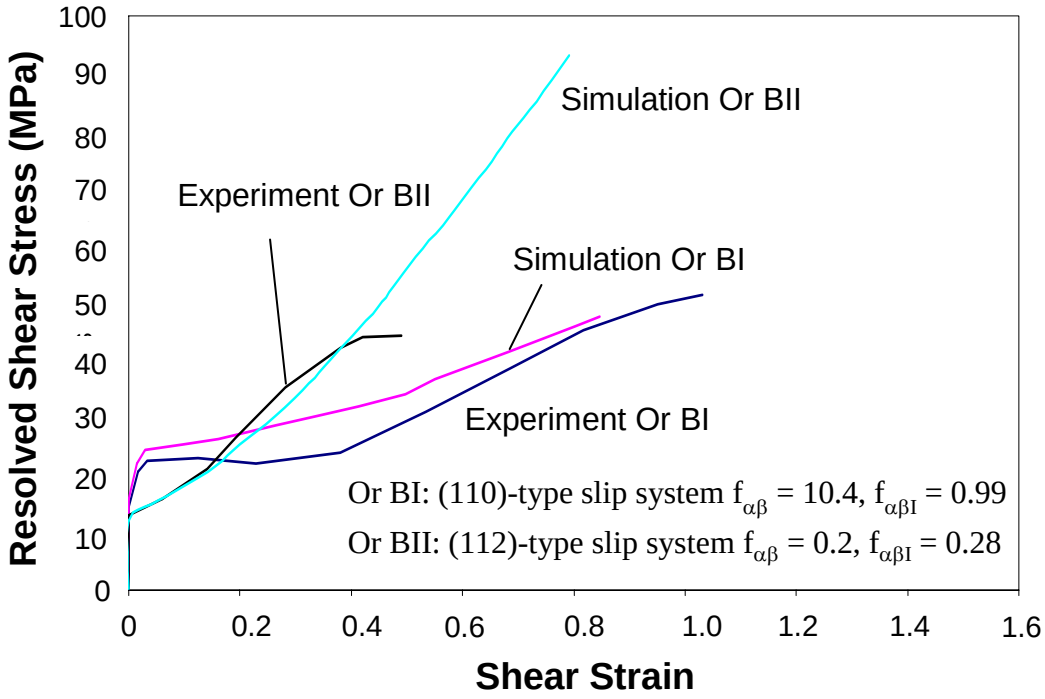

(b)

Figure 18: Interdependency of parameters (a) $f_{\alpha\beta}$ = 0.4, $f_{\alpha\beta I}$ = 0.0 (b) $f_{\alpha\beta}$ = 10.4, $f_{\alpha\beta I}$ = 0.99

The other two parameters are q and q_I which are latent to self hardening ratio based on the assumption that all the slip systems in one slip family behave similarly. Therefore, to find these parameters, two simulations are run simultaneously; one with the crystal orientation wh en primary slip system activated is of the (110)-type and the second one with a crystal

orientation such that the primary slip system activated is of the (112)-type. The interdependency of hardening parameters of different families of slip systems is evident from figure 18. It can be seen that the interaction parameters ($f_{\alpha\beta}$) of the (-101)[111] slip system effect the hardening of the (-211)[111] slip system.

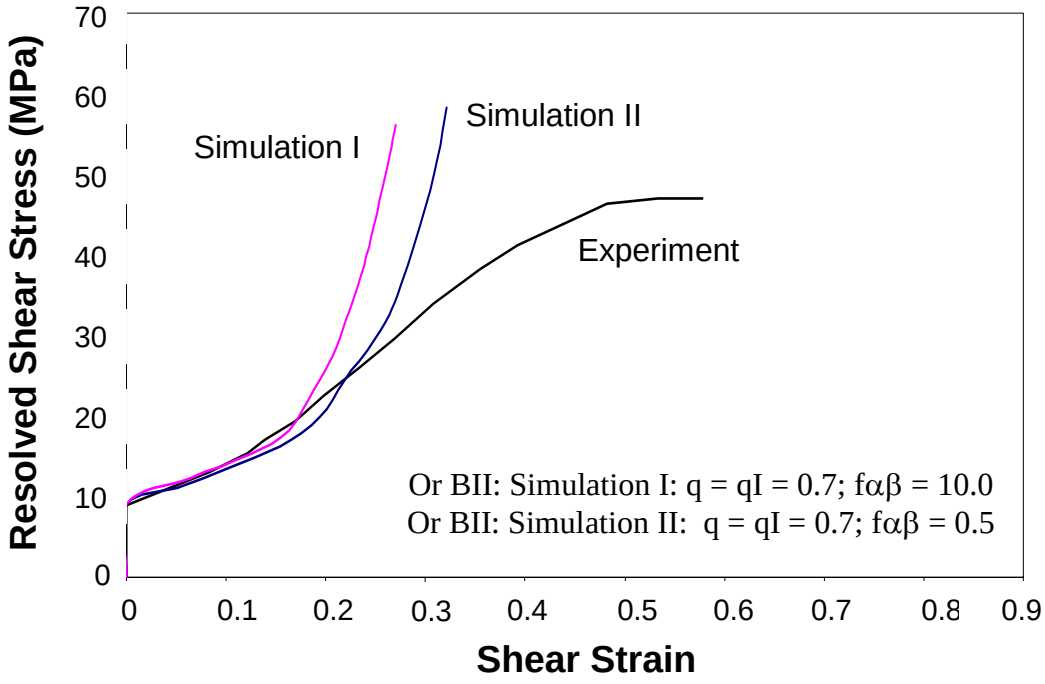

Figure 19: Effect of interaction parameter $f_{\alpha\beta}$

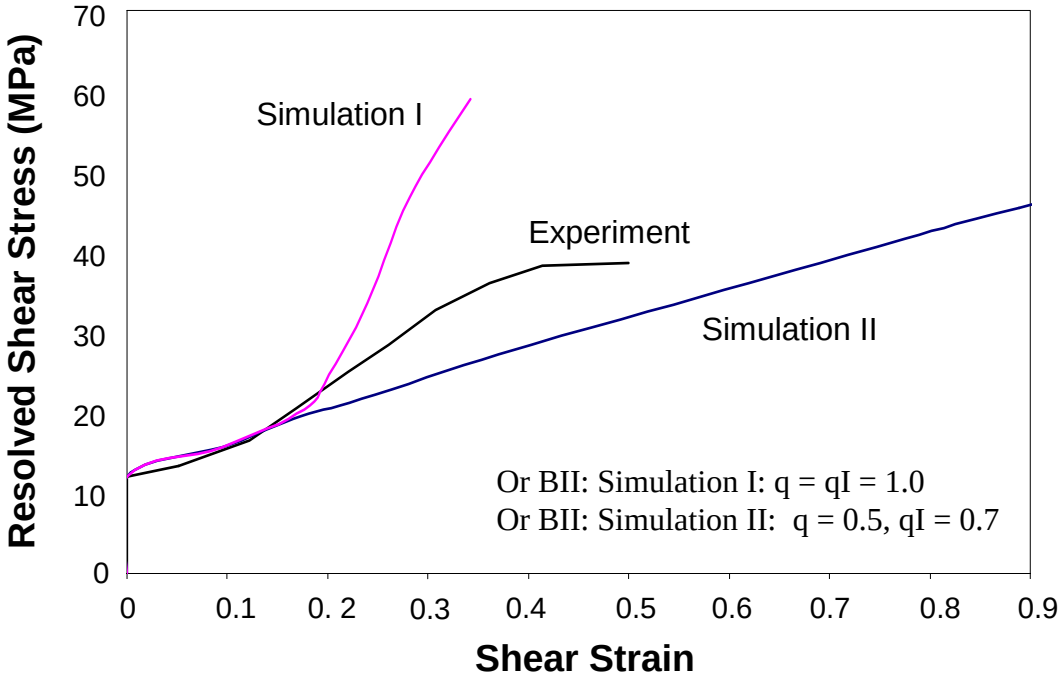

Figure 20: Effect of self to latent hardening ratio (q)

It is also seen that q and q_I have more severe effects than the other four terms ($f_{\alpha\beta}$, $f_{\alpha\beta I}$, γ_0, γ_{0I}) (Figs. 19, 20). As off diagonal terms of the $h_{\alpha\beta}$ matrix are more sensitive to the latent to self hardening ratio, this ultimately increases the current strength of the slip system $g^{(\alpha)}$.

Experimental results of Bowen [88] have been simulated to identify the hardening parameters. Simulation results are presented in figure 21 for two different crystal orientations. A compromised set of parameters is given in Table VII. It should be noted that here only diagonal hardening is considered by taking q = 0. There is no experimental proof of this assumption, but even with this assumption the three stage hardening curve is obtained and good agreement with experimental results (figure 21) are obtained for orientation BII (Or BII), when the (-211)[111] slip system is activated, but for the case of the (-101)[111] slip system the differences between the simulation result and experimental curves are high.

Table VII: Hardening parameters identfied for the Bassani & Wu (BW) model for diagonal hardening

	τ_o (MPa)	τ_s (MPa)	h_o (MPa)	h_s (MPa)	γ_o	γ_{oI}	$f_{\alpha\beta}$	$f_{\alpha\beta I}$	q	q_I
(110)[111]	13.7	16.4	292.262	1.4	0.25	0.25	10.0	9.9	0.0	0.0
(112)[111]	13.07	16.344	49.03325	39.2266	0.1	0.1	0.34	0.3	0.0	0.0

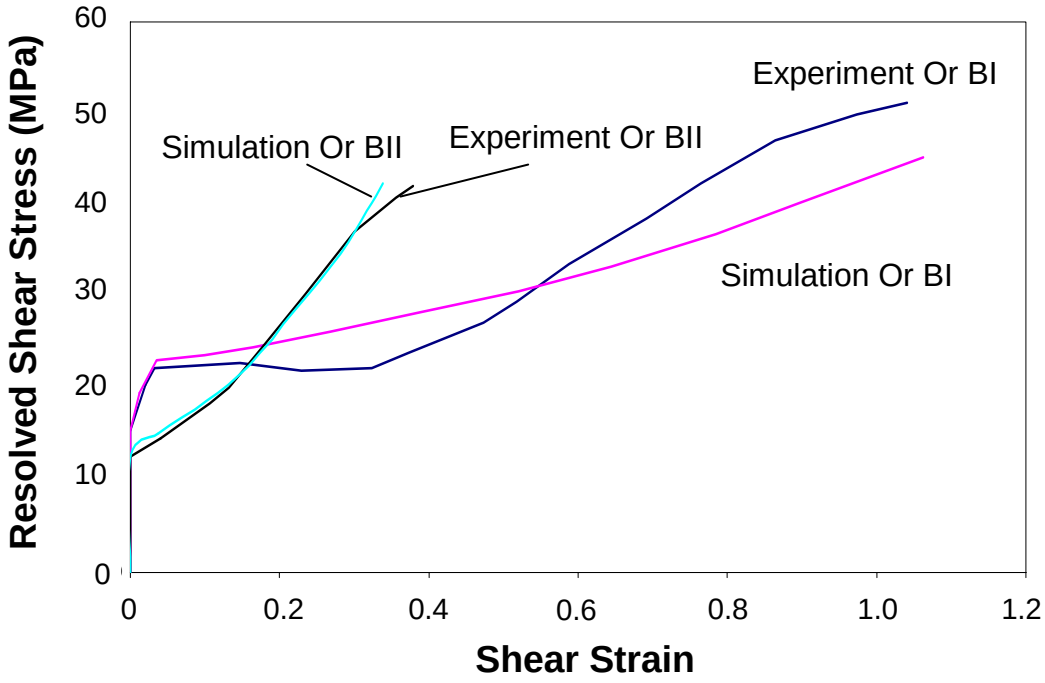

Figure 21: Hardening curve of Or BI (-101)[111] and Or BII (-211)[111] slip systems for single crystalline niobium

In what follows next, the crystal plasticity model has been interfaced with an optimization code (MINUIT) to find the set of hardening parameters discussed before for each family of slip systems. This not only reduces the computation time but also it is never easy to find 20 parameters manually.

This method is generally composed of an optimisation tool, a material model and an interface between the optimisation tool and the material model.

The problem is classically defined by a function which evaluates, for a given set of parameters, the discrepancy between the model prediction and the experimental data. The formal expression for the function is:

$$L_n(P) = \frac{1}{d\varepsilon}\int \left\| R^*(\varepsilon) - R(P,\varepsilon) \right\| dt \tag{52}$$

where dε is the length of observation (strain increment), $R^*(\varepsilon)$ is the experimental data of uniaxial test (true stress), R(P, ε) is the simulation result of uniaxial test (true stress) and $[R^*(\varepsilon)-R(P,\varepsilon)]$ is the difference between experimental data and calculation result from a given set of model parameters. The procedure is described in figure 22.

During the simulation, it has been seen that secondary slip systems activate before reaching the experimental stage-II deformation. Therefore, the simulation result gives higher hardening values during stage-I (figure 21) as compared to the experimental result. To avoid this higher hardening response during stage-I, interaction parameters are only activated at the end of the single slip region, i.e. stage-I.

Using this technique the material parameters (h_o, h_s, τ_o, τ_s, γ_o, γ_{oI}, $f_{\alpha\beta}$, $f_{\alpha\beta I}$, q, q_I) for the two orientations Or BI and Or BII are identified. 10 parameters for each family of slip systems are identified using the optimization tool and the following set of parameters give good agreement with the experimental results as shown in figure 23.

Table VIII: Parameters identified for the Bassani & Wu (BW) model of uniaxial tension test Bowen [88]

	τ_o (MPa)	τ_s (MPa)	h_o (MPa)	h_s (MPa)	γ_o	γ_{oI}	$f_{\alpha\beta}$	$f_{\alpha\beta I}$	q	q_I
(110)[111]	13.7	18.4	292.262	0.001	0.0075	0.4807	3.3	1.6623	0.2891	0.2315
(112)[111]	13.07	10.344	25.03325	24.2266	0.04	0.039	0.49	0.14	0.01	0.011

As discussed previously the interdependency of interaction parameters of one family of slip systems significantly effects the hardening of the other family of slip systems. Therefore, the

identification of hardening parameters has been done by running both simulations simultaneously.

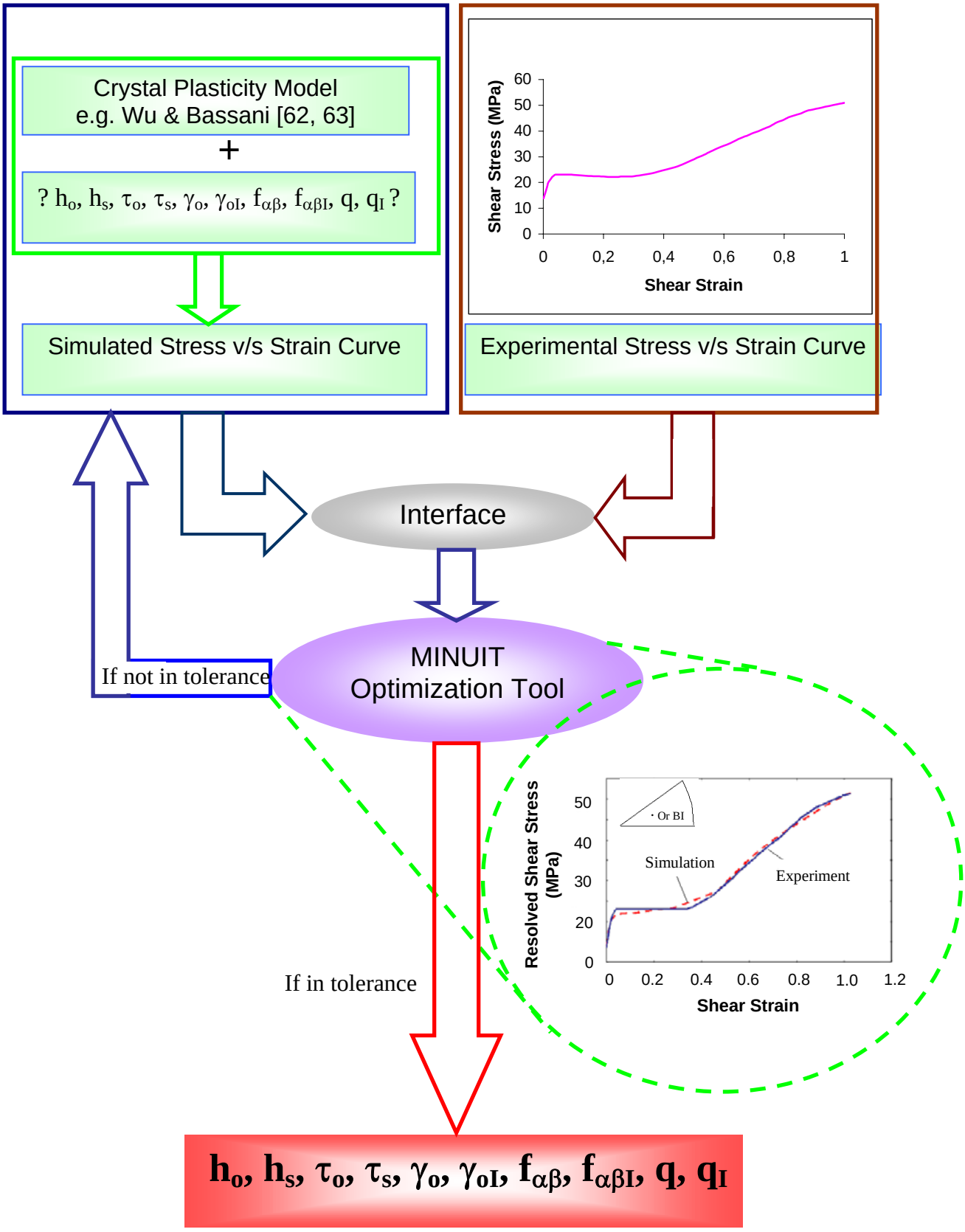

Figure 22: Automatic identification procedure

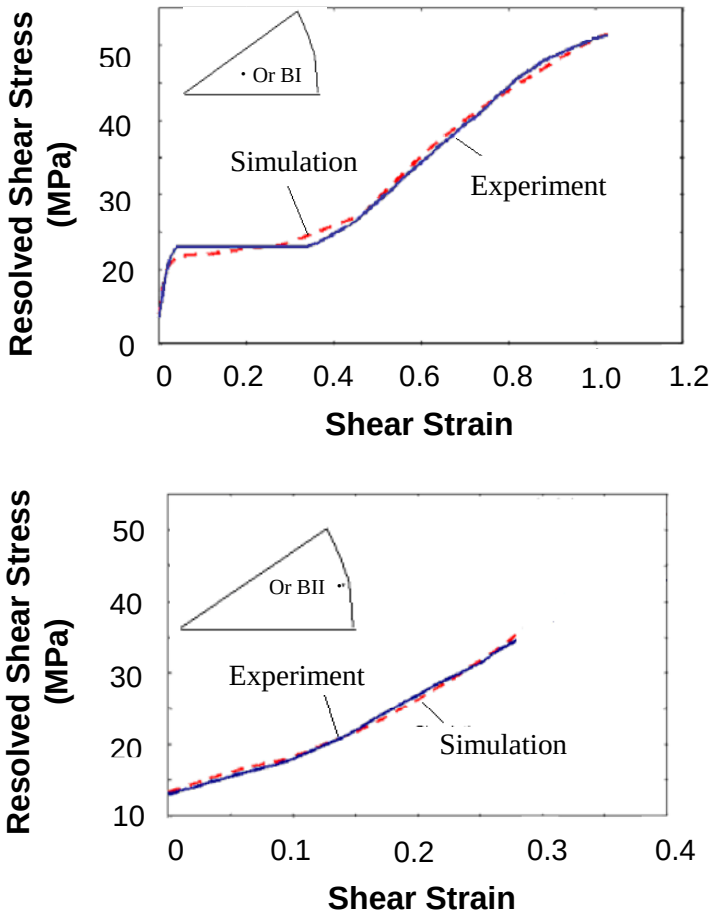

Figure 23: Hardening curves for Or BI (-101)[111] and Or BII (-211)[111] systems

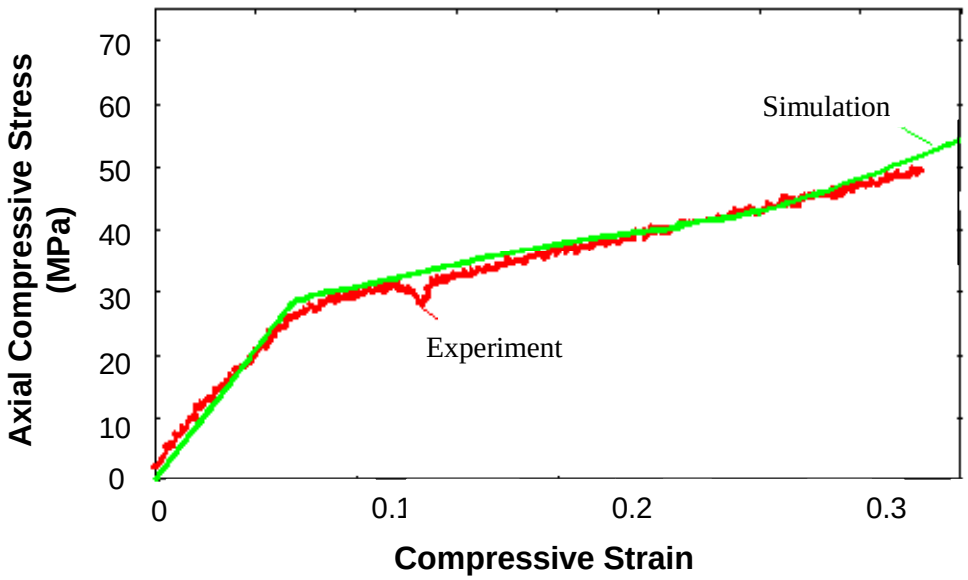

Figure 24: Comparison of stress vs. strain curve of compression test for the [214]-orientation

After the identification process, a compression test is simulated for a [214] loading axis orientation [101]. The experiments are performed at 20°C with a strain rate of 0.54 mm/min. Experimental and simulated results are in good agreement as shown in figure 24.

The sets of identified parameters are given in table IX. The parameters found show that the interaction parameters (γ_o, γ_{oI}, $f_{\alpha\beta}$, $f_{\alpha\beta I}$, q, q_I) are more or less the same as found for previous simulations - only the initial resolved shear stress and the saturation stress are different. Possible reasons could be the amount of impurities (hydrogen, nitrogen, oxygen), slip systems behave differently during compression when compared with tension and a different strain rate as compared to the experimental results simulated previously in figure 23, which changes the initial yielding behaviour of niobium [88].

Table IX: Crystal plasticity hardening parameters identified for the Bassani & Wu (BW) model of uniaxial compression test [101] of single crystalline niobium

	τ_o (MPa)	τ_s (MPa)	h_o (MPa)	h_s (MPa)	γ_o	γ_{oI}	$f_{\alpha\beta}$	$f_{\alpha\beta I}$	q	q_I
(110)[111]	6.99	8.4	292.262	0.001	0.0075	0.48	3.3	1.6	0.3	0.2
(112)[111]	6.99	8.38	25.03325	24.2266	0.04	0.039	0.49	0.14	0.01	0.011

4.1.6 Summary

The presented results show that the Bassani & Wu (BW) model can be used to simulate the hardening of niobium single crystals. The results from different hardening models (Peirce, Asaro and Needleman (PAN) [61], and BW model [62, 63]) are discussed. Only the BW model provides a way to simulate e the three stage hardening by taking into account the interaction of slip systems during the stages II and III of the deformation. It is also shown that interaction parameters of one slip system family influence the hardening of other systems. Therefore, in order to identify parameters for two families of slip systems, a compromise between the two parameter sets have to be found. Handling of identification of a larger number of parameters is a time consuming work. To resolve this problem an interface has been created between an optimization tool and ABAQUS to perform automatic identification of these parameters. By using this automatic identification procedure good agreement with experimental single crystalline uniaxial stress-strain curves of niobium is obtained.

4.2 Crystal Orientation Effects of the Metal on the Crack Initiation Energies of a Bimaterial Interface (Nb/Al_2O_3)

This section presents the results obtained from crystal plasticity finite element simulations without crack propagation. The crystal orientation effects on the crack initiation energy of niobium/alumina joints are studied. Three different techniques namely, global energy method, J-integral method, and virtual crack closure technique have been applied to compute the energy release rate of the niobium/alumina joints. Simulations have been performed by using two different theories, i.e. deformation plasticity theory and crystal plasticity theory. The deformation plasticity theory is used to show the consistency of the energy release rates computed with above mentioned techniques. Crystal plasticity theory is used to examine orientation effects of the niobium single crystal on the energy release rate. Differences in the computed energy release rates are explained based on the plastic slip (strain) induced in different slip systems during deformation. A qualitative comparison of the crystal plasticity simulations with the experiments of [22, 23] is also been presented.

4.2.1 Introduction

Metal/ceramic bimaterials with a mismatch in mechanical properties are frequently encountered in engineering applications. In many of these situations, cracks initiate at interfaces and advance along or away from the interfaces. The safety of such components inevitably requires a thorough understanding of their behaviour under load.

Three different methods will be used to find the energy release rate of the system: J-integral method [103, 107], global energy method [39, 113] and virtual crack extension technique [101].

The J-integral method is widely used in rate-independent quasi-static fracture analyses to characterize the energy release rate associated with crack growth [107]. The J-integral method was introduced by Rice [103] in 1968, since then J-based elastic plastic fracture mechanics became also an issue of numerical computations [112, 113]. In the beginning the user were left to their own codes, which gave rise to additional uncertainties and errors. Scheider [103] explained the procedure to obtain reliable values of J-integral when used in ABAQUS.

The global energy method was used in [39, 108] for bimaterial interfaces. It was also applied to separate the energy release rate in elastic and plastic parts.

The virtual crack extension technique [101] is widely used to compute the energy release rates of delamination in composite structures. The main advantage of this technique is the mode

separation of energy release rates when using the mixed mode fracture criterion [101]. Ingraffea [114] and Krueger [101] described a procedure to compute energy release rates by using the virtual crack extension method from continuum (2D) and solid (3D) finite element analyses.

All of these three methods, i.e., the global energy method, J-integral method and virtual crack closure technique are discussed in section 3.2.

4.2.2 Finite Element Model

The finite element model is based on the experiments performed in [22, 23], in which the influence of orientation and impurities on the fracture behaviour of Nb/sapphire interfaces were studied using notched bending tests. The specimens to perform four-point bending test experiments in [22, 23] were prepared by diffusion bonding single crystals of niobium and alumina in an ultra high vacuum furnace for different interface orientations. It was found that for undoped bicrystals bonded at 1400 °C, the computed interfacial fracture energy ranged from 77 to 2100 J/m^2 depending on the interface planes of Nb and sapphire. For fracture evaluation, interfacially notched bending test specimens of dimensions 2 x 4 x 36 mm^3 were prepared. The specimens is shown in figure 25. The notch length is 0.4 mm. The specimens is loaded to the fracture load F_c in a four-point bending tests device at a crosshead speed of 96.8 µm/min. The load F and the crosshead deflection at the load points v are simultaneously recorded.

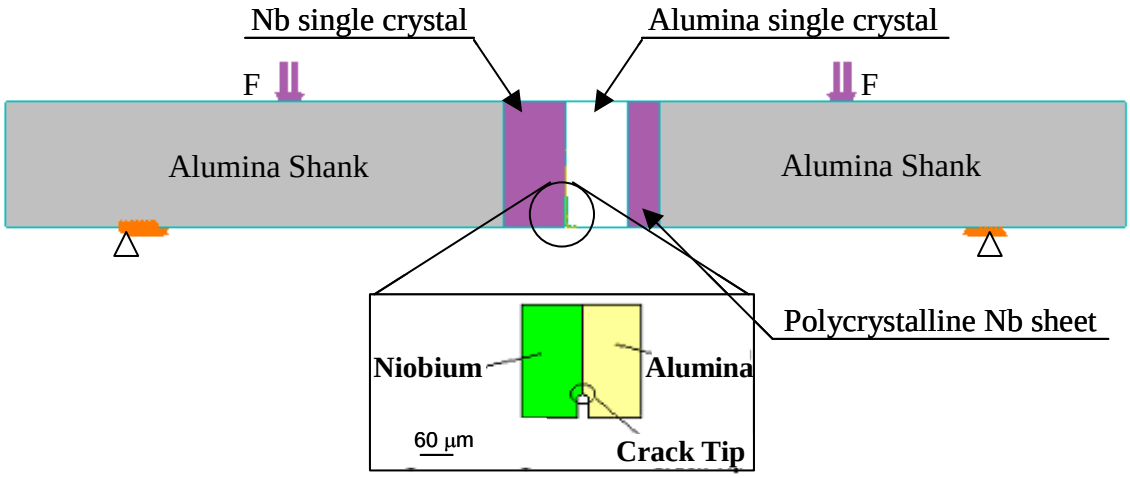

Figure 25: Four point bending test specimens

The finite element model is constructed based on the information provided in [22, 23]. As shown in figure 25, the finite element model of a niobium single crystal is bonded to alumina using bond option available in ABAQUS. Finite element models of alumina shanks and a polycrystalline niobium sheet were joined with the corresponding niobium single crystal finite

element model and alumina finite element model using tie constraints available in ABAQUS. The tie constraint is used because the studies reported in this chapter are performed for a stationary crack tip, i.e. no crack propagation is allowed. In this constraint, nodes of the two adjoining surfaces are fixed to each other to ensure that two surfaces are always bonded during the simulations.

4.2.3 Finite Element Analysis

Finite element simulations were performed in a step by step fashion. Starting from a two dimensional analysis for a bimaterial interface, we move to three dimensional analyses for the same bimaterial interface to check the consistency of the methods used to compute the fracture energies of the interface including crystal plasticity effects.

Two dimensional analyses are performed to check the consistency of the three methods (global energy method, J-integral method, and virtual crack closure technique) described above. Then more realistic three-dimensional analyses are used to study the effects of elastic anisotropy while crystal plasticity is included in the model in a subsequent step in order to take orientation dependent plasticity effects into account.

The finite element mesh for the case of two-dimensional analyses consists of plane-strain eight-node quadratic reduced integration elements. The total number of elements is 12172. The mesh is shown in figure 26.

For the case of the three-dimensional analyses, the finite element mesh consisted of twenty-noded quadratic reduced integration elements. The total number of elements in the model is 17208. The mesh is shown in figure 27.

For all two- and three-dimensional simulations, both outer Alumina shanks (ceramic) and Alumina single crystal at the middle of the specimens were treated as purely elastic with a Young's modulus of 390 GPa and a Poisson's ratio of 0.27. The polycrystalline niobium sheet is always modelled with an elastic-plastic constitutive law. The Young's modulus and the Poison's ratio for polycrystalline niobium sheet were the same for all simulations (E = 104.9 Gpa, ν = 0.397). These elastic and plastic data are adjusted to alumina and niobium, respectively in [39, 108, 109]. The plastic behaviour of the stress-strain curve of the polycrystalline niobium sheet is approximated by a Ramberg-Osgood relation [110], which is described in the one-dimensional case by the following equation:

$$E_c \varepsilon = \sigma + \alpha \left(\frac{\sigma}{\sigma_0} \right)^{n-1} \sigma \tag{53}$$

Here, n denotes the hardening exponent, α the yield offset and σ_0 the yield stress. This material law is nonlinear from the beginning, but for commonly used hardening exponents ($n \geq 5$) the divergence from linearity is only slight for stresses below σ_0. The chosen plasticity theory is the deformation plasticity theory (for details see [111] and references therein), which describes not a plastic material behaviour, but a nonlinear elastic material. This means, that no unloading criterion exists. The parameters of the above equation are adjusted to the niobium stress-strain curves in [40]. The parameters used are $n = 6$, $\sigma_0 = 180$ MPa and $\alpha = 0.3$.

The single crystal niobium part is modelled as isotropic material, using the same mechanical properties as the polycrystalline niobium sheet for two- and three-dimensional isotropic simulations, using the same set of parameters as used above for the polycrystalline niobium sheet.

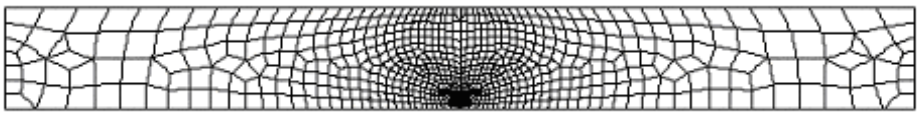

Figure 26: Finite element mesh of two-dimensional bimaterial specimens

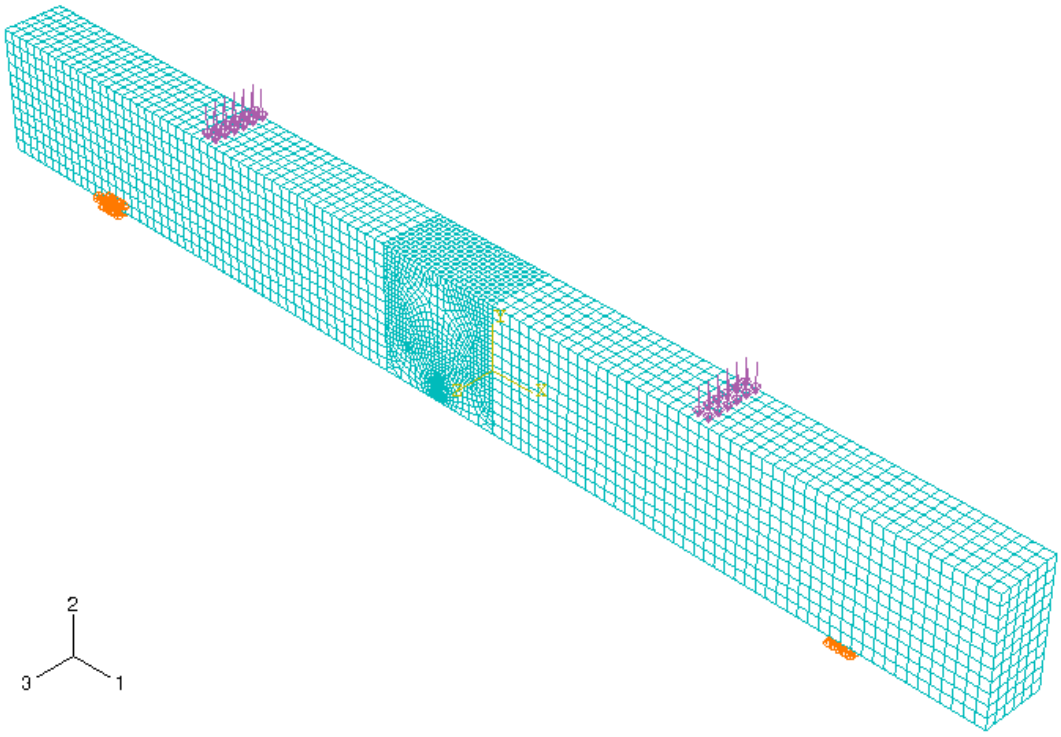

Figure 27: Finite element model of four point bending test specimens

For the case of crystal plasticity the single crystal niobium is modelled using the hardening law of Bassani & Wu (BW) [63, 62]. The hardening parameters for each slip system are derived in [104] and have already been discussed in detail in section 4.1. The hardening

parameters used for each family of slip system, i.e., (110)[111] and (112)[111], are given below (Table X):

Table X: Hardening parameters for Bassani & Wu (BW) hardening law

	τ_o (MPa)	τ_s (MPa)	h_o (MPa)	h_s (MPa)	γ_o	γ_{oI}	$f_{\alpha\beta}$	$f_{\alpha\beta I}$	q	q_I
(110)[111]	13.7	8.4	292.26	0.001	0.0075	0.48	3.3	1.66	0.289	0.2315
(112)[111]	13.07	10.34	25.033	24.227	0.04	0.039	0.49	0.14	0.01	0.011

A four point bending test has been modelled three-dimensionally and simulated with the boundary conditions as shown in figure 27. The displacement of 30 μm is applied stepwise (increasing linearly with time) at the loading points.

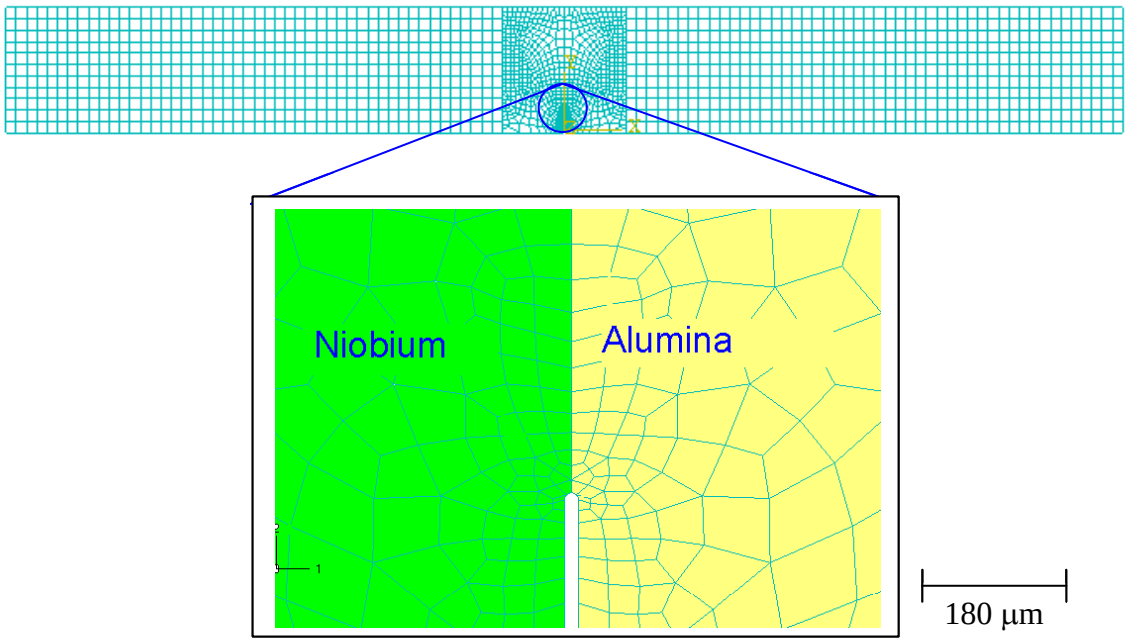

Figure 28: Three dimensional finite element mesh of bimaterial specimens

4.2.4 Results and Discussion

The energy release rates for two-dimensional analyses (without crystal plasticity) computed using three different techniques, i.e., the virtual crack closure technique, global energy method and J-integral method are shown in figure 29. All three approaches provide consistent results. The difference in the computed values of energy release rates are almost negligible. A comparison of the energy release rates of two- and three-dimensional simulations (without crystal plasticity) is shown in figure 30, values of the computed energy release rates are identical.

As mentioned in the previous section, the crystal plasticity theory is included by modelling the niobium as single crystals using the Bassani & Wu (BW) [62, 63] hardening law. The set of hardening parameters used is given in table VIII. A polycrystalline niobium sheet is modelled as isotropic elastic-plastic material using a Ramberg-Osgood hardening law [110], while Alumina shanks and Alumina single crystals are always modelled as isotropic elastic material.

Five different orientations of niobium single crystals have been used for the simulation (see table XI). The orientations I, II and III are the same as were studied by Korn et al, [22, 23] where a strong orientation effect on the fracture energy was found by changing the orientation of single crystalline niobium. Orientations IV (see section 4.1.4, Or BI) and V (see section 4.1.4, Or BII) are the ones for which the crystal plasticity hardening parameters have been identified using the single crystalline experimental results on niobium of Bowen [88] in order to study the effect of these orientations on the fracture energy, although no experimental comparison has been made for orientation IV and V, as experimental fracture energy data are not available for these two orientations.

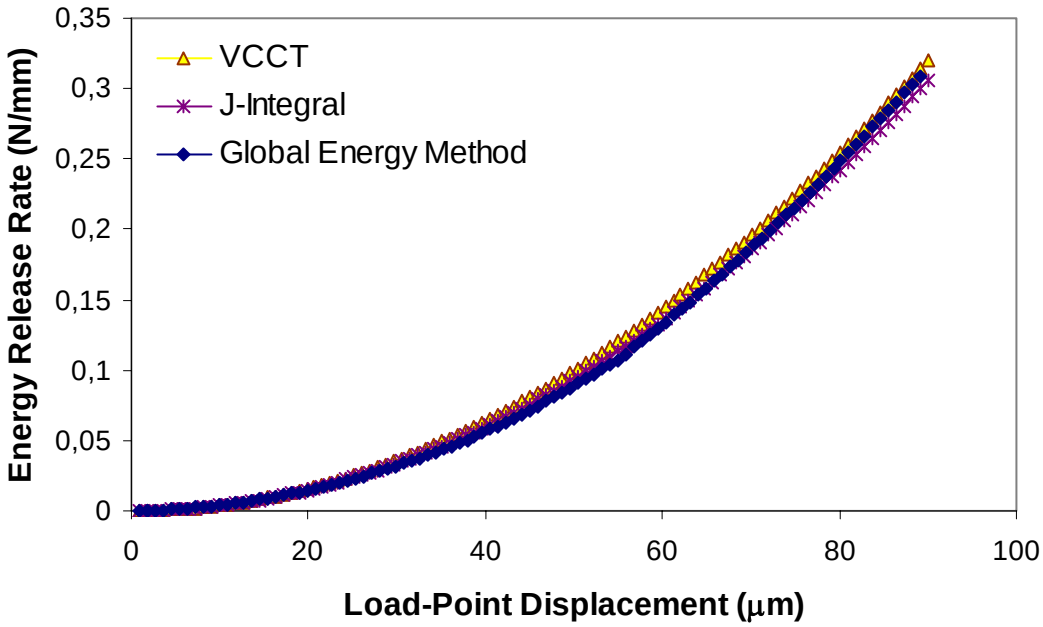

Figure 29: Energy release rate comparison among different methods of two-dimensional analyses (plane strain)

In the following, the results of the energy release rate, strain distribution around the stationary crack-tip along with the plastic slip (strain) near the stationary crack-tip are discussed for different orientations of the metal while the ceramic was kept identically oriented.

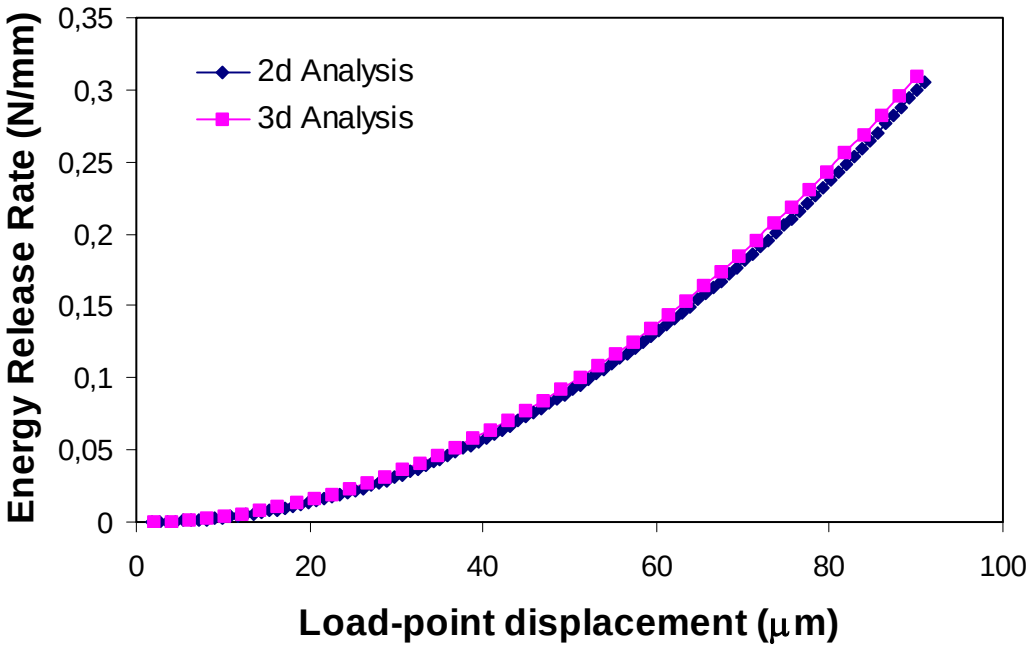

Figure 30: Comparison for energy release rates for 2D and 3D analyses

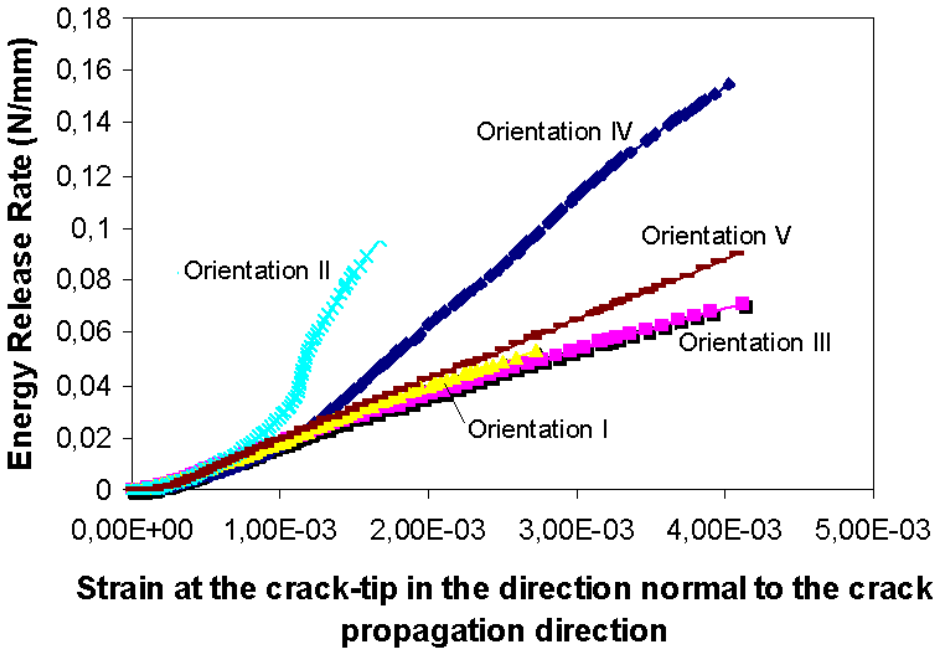

Figure 31: Total energy release rate versus the strain at the crack tip for various orientations

The energy release rates for the five different orientations I - V (Table XI) have been plotted against the strain at the stationary crack-tip in figure 31. The results depict that the change in crystal orientation significantly influences the energy release rates only after the plastic deformation in the metal part has started. The start of the plastic deformation is the point

where the resolved shear stress of the most favourably oriented slip system exceeds the initial yield stress τ_o, which can be monitored during the simulation run.

Table XI: Orientations of niobium single crystals used for simulations

Symbol	Orientation relationship
Orientation I	Nb(100)[001]|Sp(11-20)[0001]
Orientation II	Nb(110)[001]|Sp(11-20)[0001]
Orientation III	Nb(111)[-1-1-2]|Sp(11-20)[0001]
Orientation IV (Or BI)	Nb(-0.146 -0.94 0.3)[0.4 –0.33 -0.85]|Sp(11-20)[0001]
Orientation V (Or BII)	Nb(-0.23 -0.94 0.25)[0.6 –0.34 -0.7]|Sp(11-20)[0001]

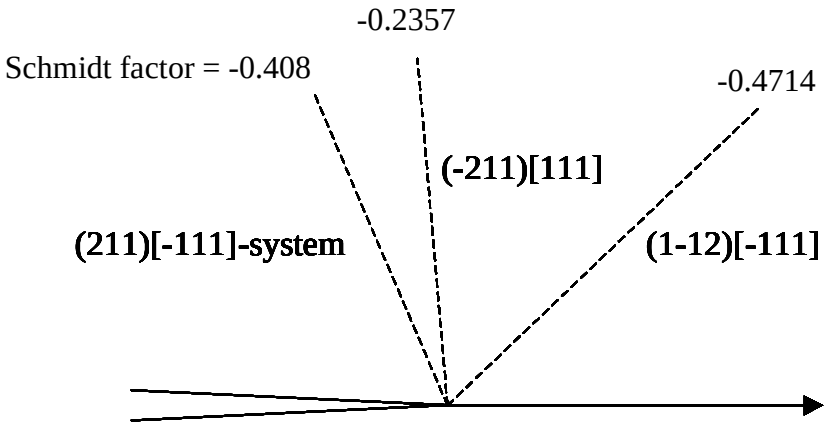

Figure 32: Slip systems with highest Schmidt factors for orientation II

The highest energy release rate is found for orientation II, which is a multiple slip orientation with (1-12)[-111], (-211)[111] and (211)[-111] systems playing a major role in the total plastic slip and eventually in the plastic strain (see figure 31). The reason is the highest Schmidt factor for these (1-12)[-111], (-211)[111] and (211)[-111] systems, i.e. ~ -0.4714, -0.2357 and -0.408, respectively (as shown in figure 32), while other slip systems have smaller Schmidt factor ~ -0.2 or even less. Figure 33 shows the relative magnitudes of the slip activity, where the slip activity at a radius of 15 µm (it is a reasonable distance from the crack tip where influence of all the activated slip system was seen during the simulations; distances other than 15 µm give similar results, i.e. same slip systems contributing in total accumulated slip but only the magnitude of plastic strain changes) from the crack tip is plotted for each of the activated slip systems relative to the polar angle φ; 0° coincides with the prolongation of the crack and 180° coincides with the single crystal niobium crack flank. It can be easily identified which slip system is contributing the highest amount of plastic slip in different regions around the crack tip. Figure 33 shows that the maximum contribution of plastic slip

comes from the slip system (1-12)[-111] for the polar angle φ range of 0° - 60° while the contribution of slip systems (-211)[111] and (211)[-111] is maximum for the range of 60° - 120°.

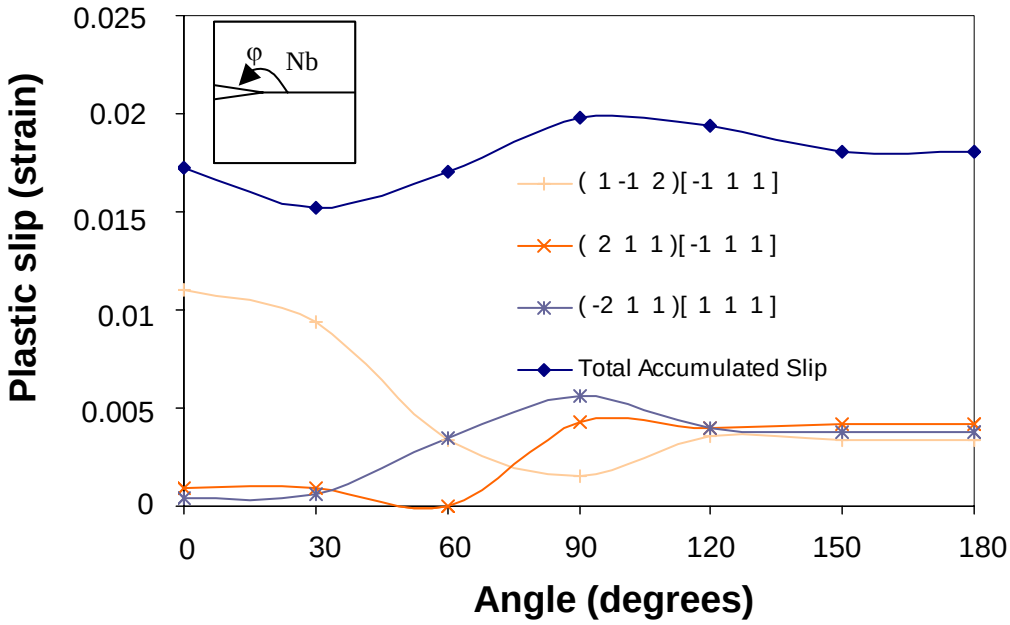

Figure 33: Plastic strain on slip systems at 15 μm radius from the tip of a stationary crack for orientation II

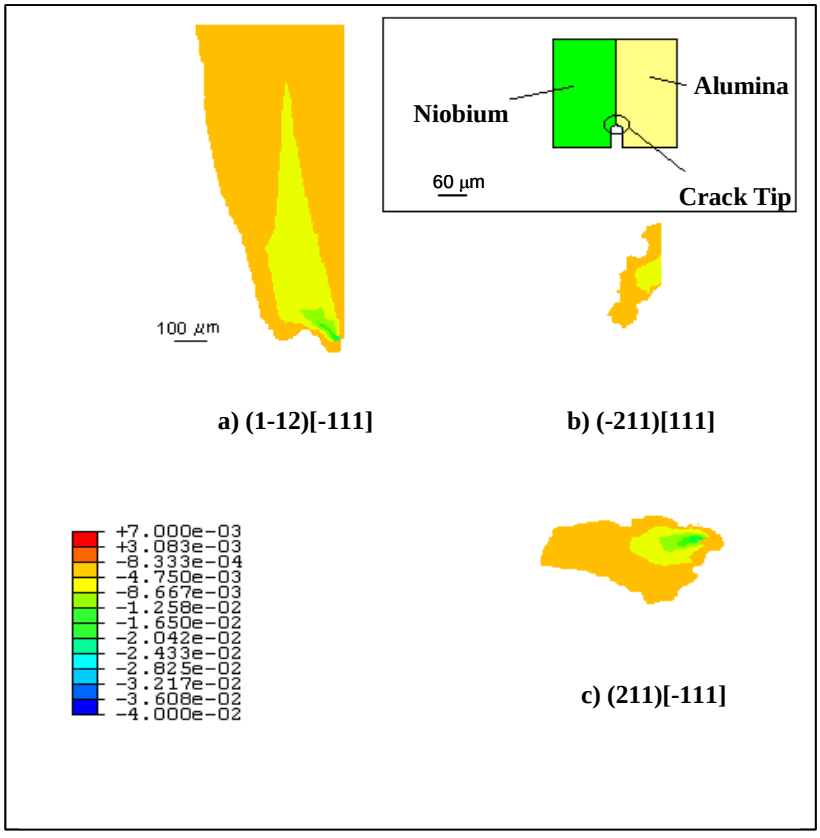

Figure 34: Plastic strain on various slip systems at the tip of a stationary crack for orientation II

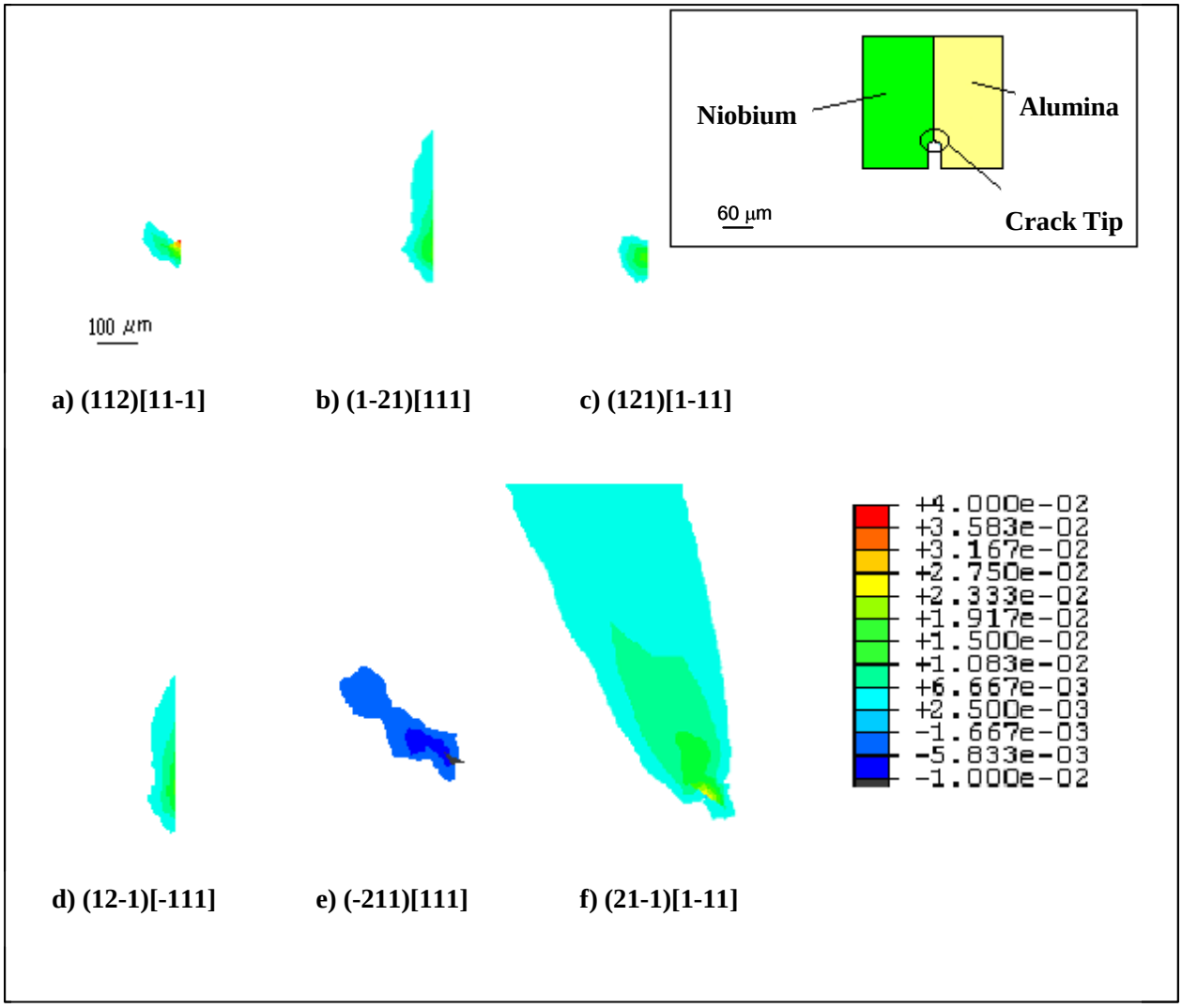

Figure 35: Plastic strain on various slip systems at the tip of a stationary crack for orientation I

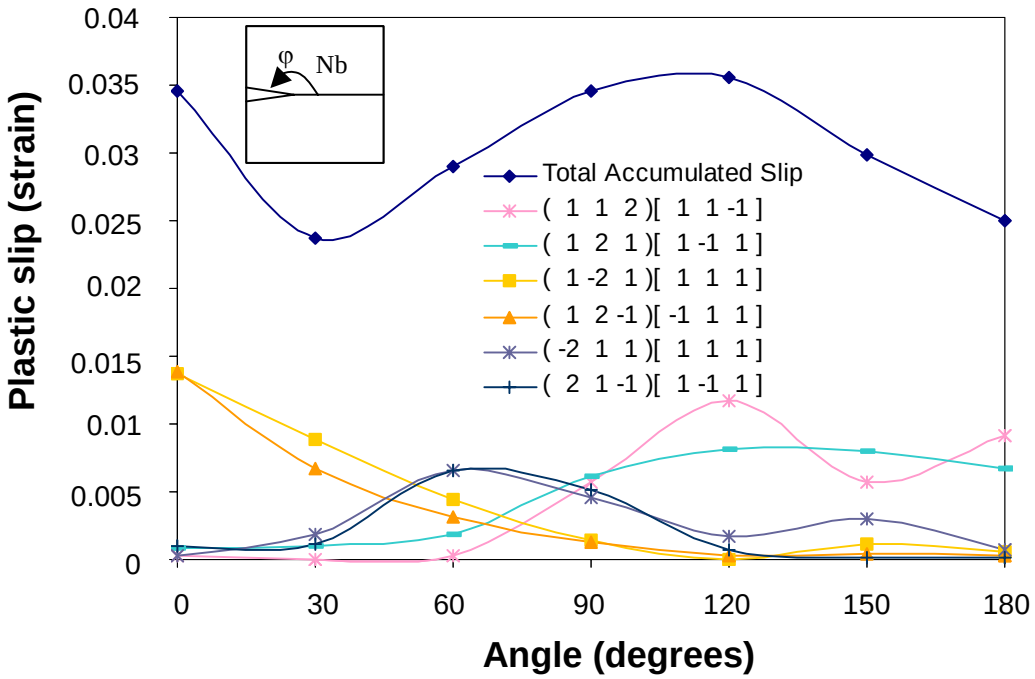

Figure 36: Plastic strain on slip systems at 15 μm radius from tip of a stationary crack for orientation I

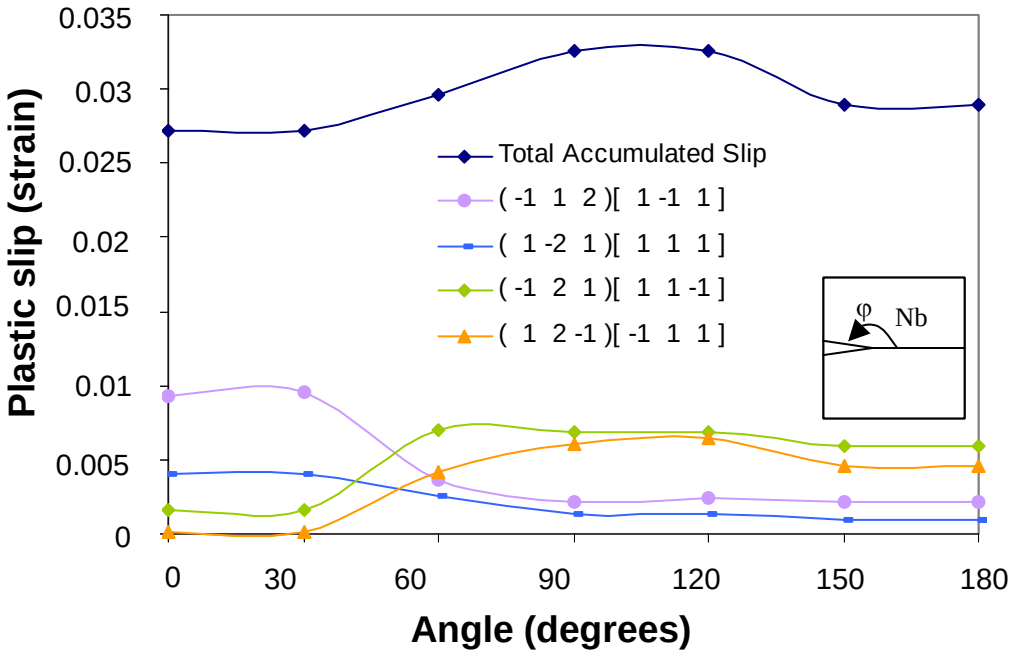

Figure 37: Plastic strain on slip systems at 15 μm radius from tip of a stationary crack for orientation III

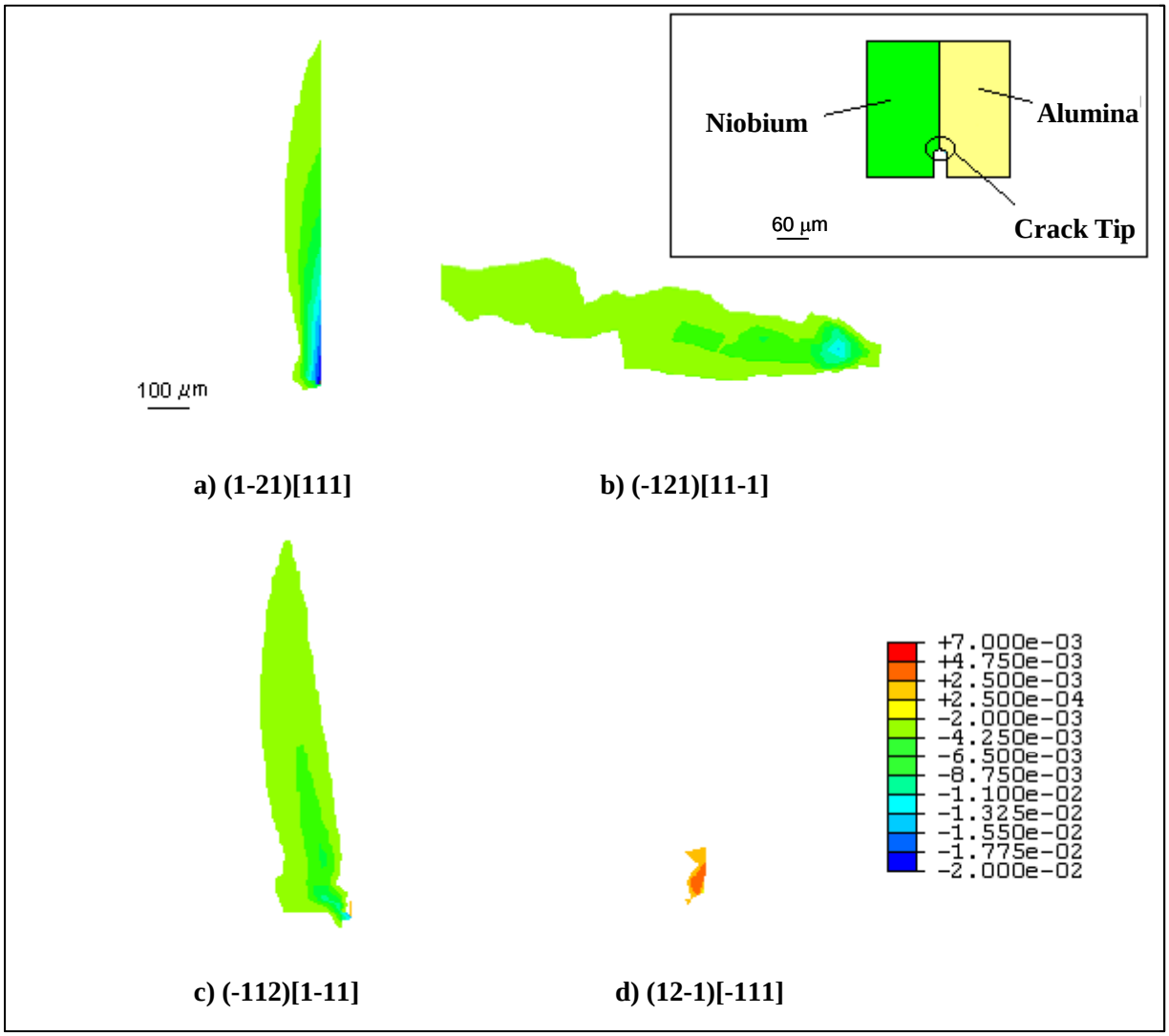

Figure 38: Plastic strain on various slip systems at the tip of a stationary crack for orientation III

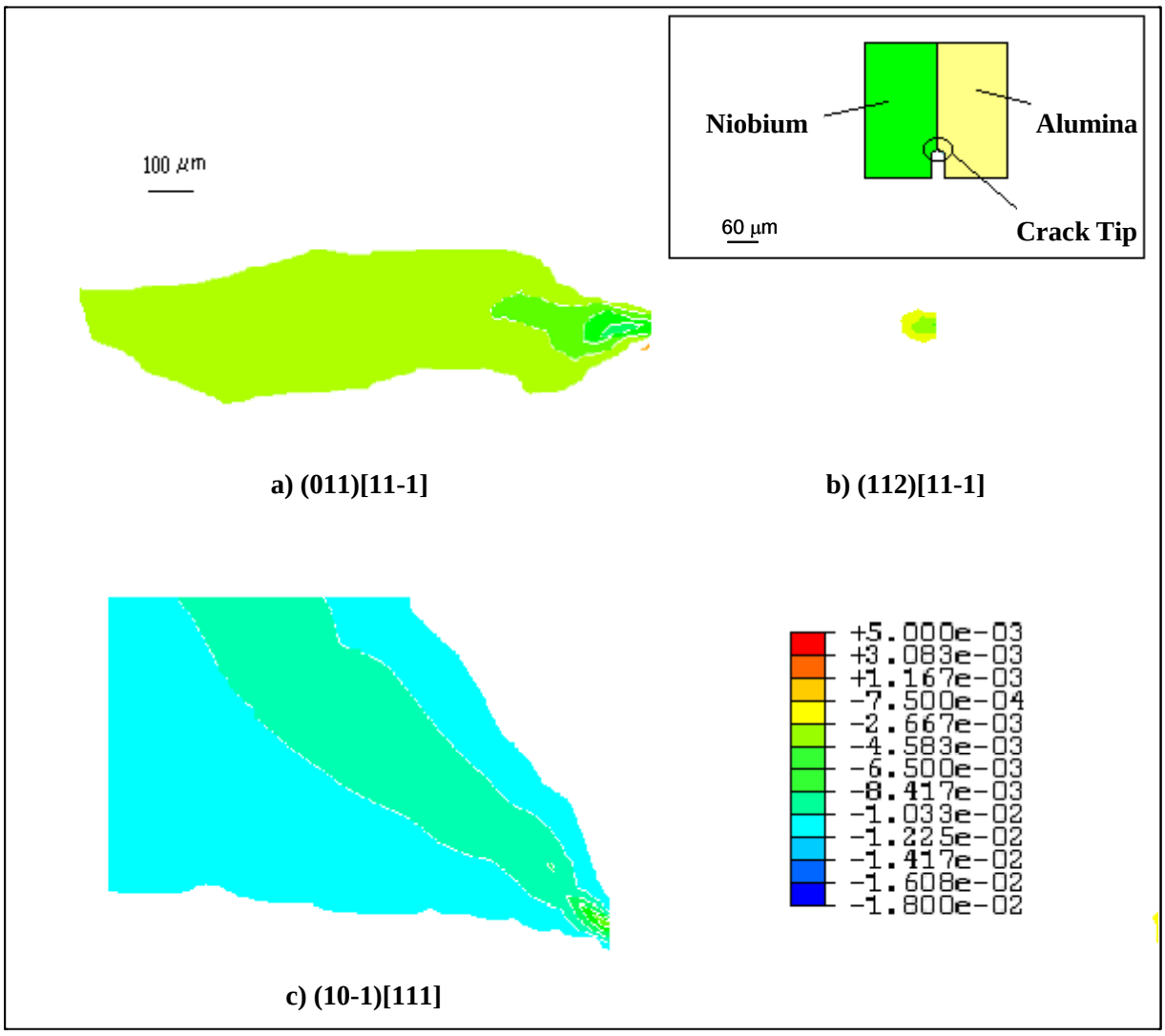

Figure 39: Plastic strain on various slip systems at the tip of a stationary crack for orientation IV

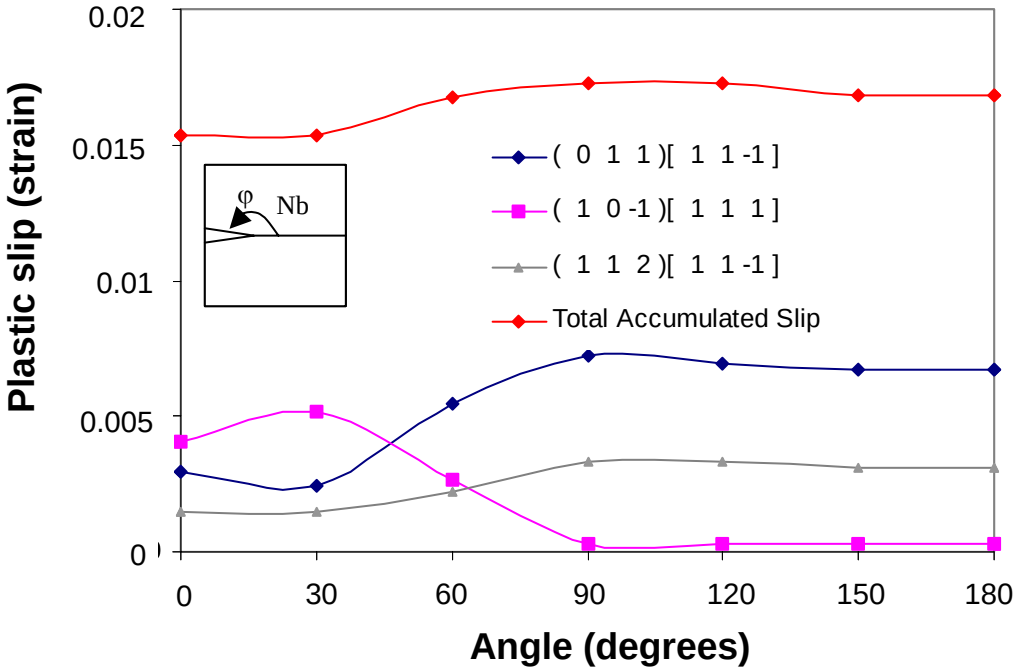

Figure 40: Plastic strain on slip systems at 15 μm radius from tip of a stationary crack for orientation IV

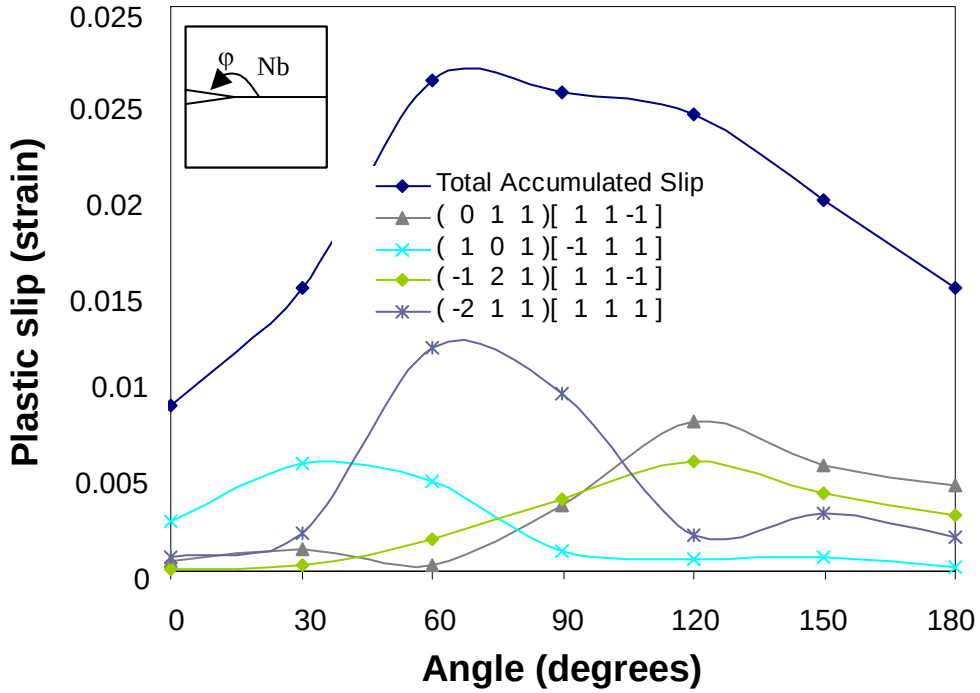

Figure 41: Plastic strain on slip systems at 15 μm radius from tip of a stationary crack for orientation V

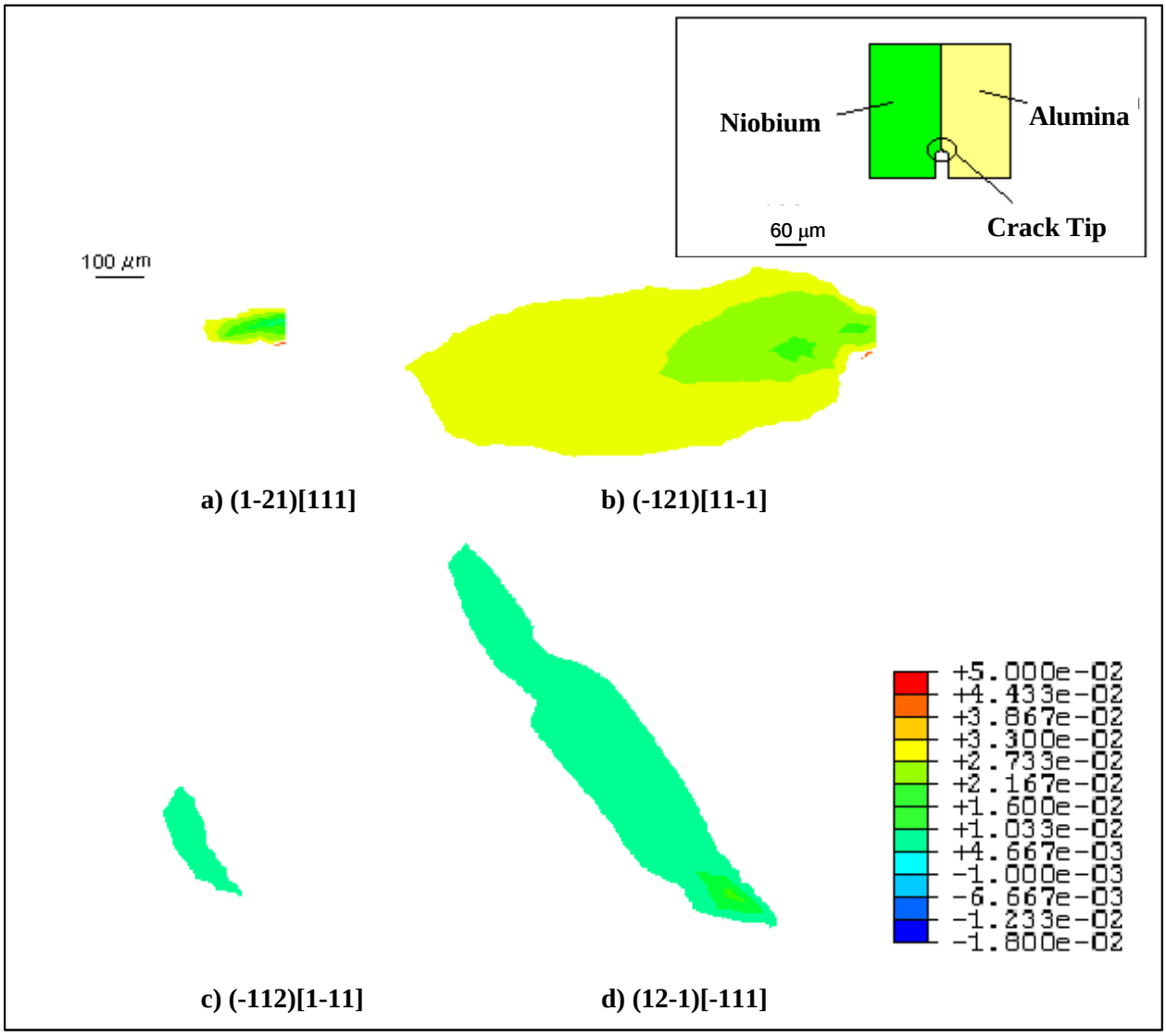

Figure 42: Plastic strain on various slip systems at the tip of a stationary crack for orientation V

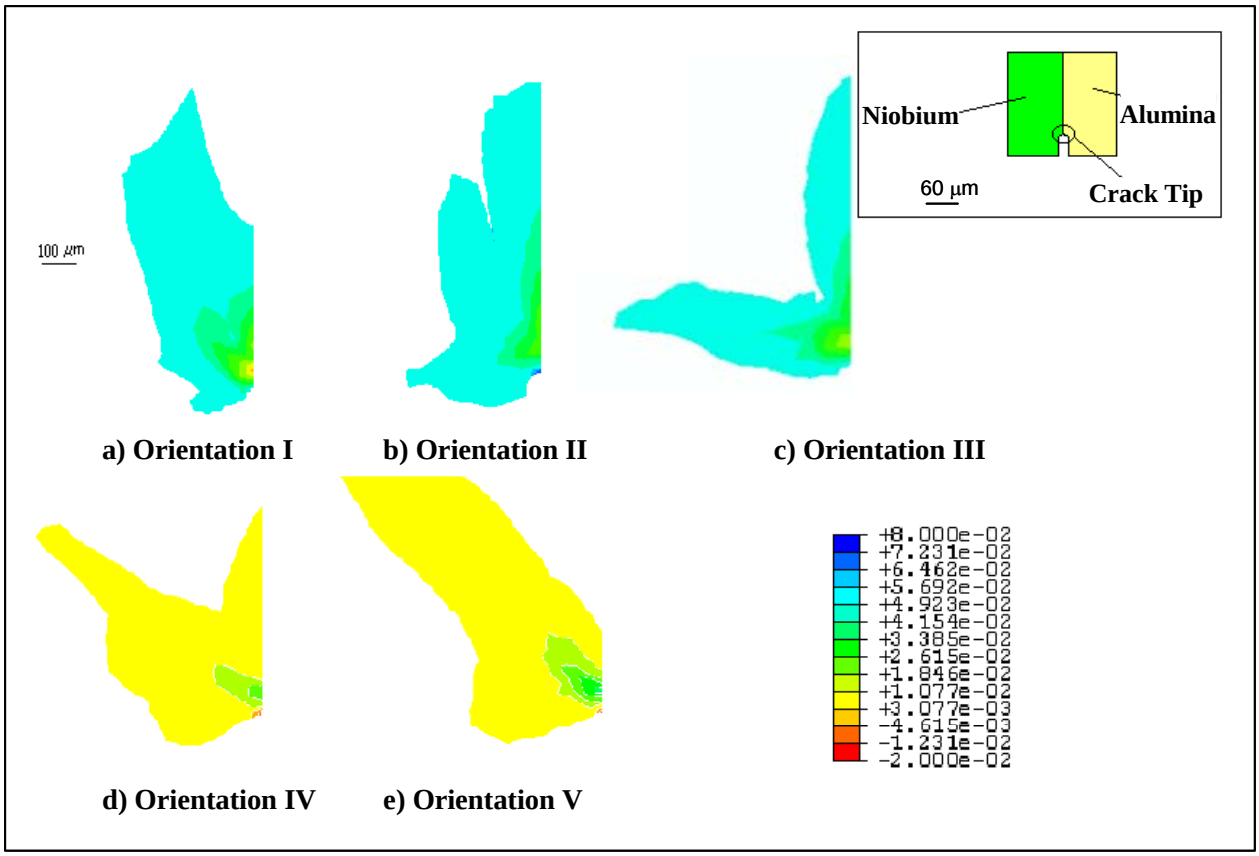

Figure 43: Plastic cumulative slip (strain) on all slip systems at the tip of a stationary crack for various orientations

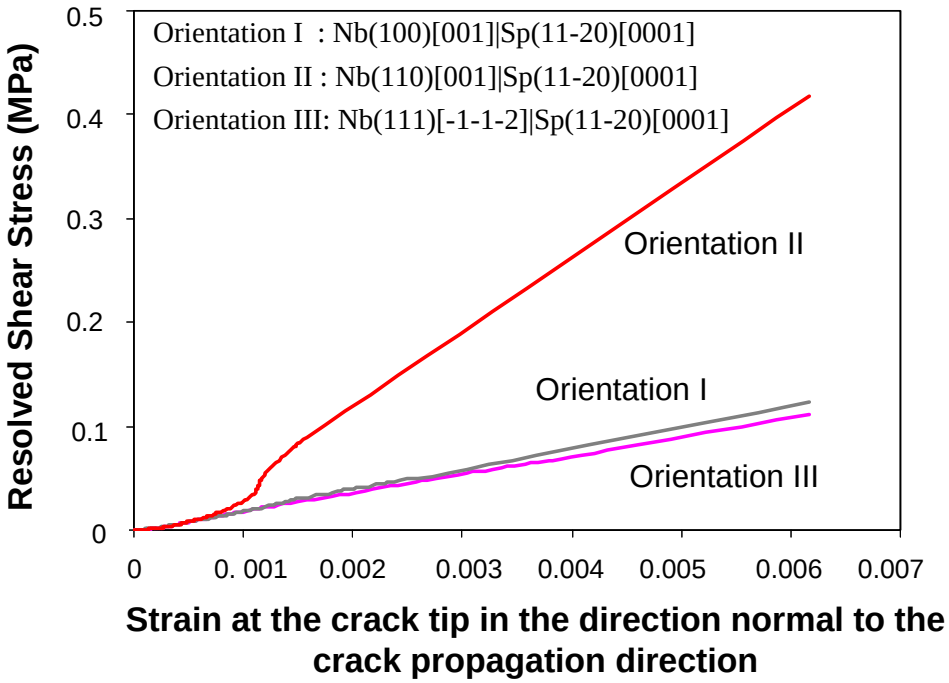

Figure 44: Comparison of energy release rates for three orientations I, II and III

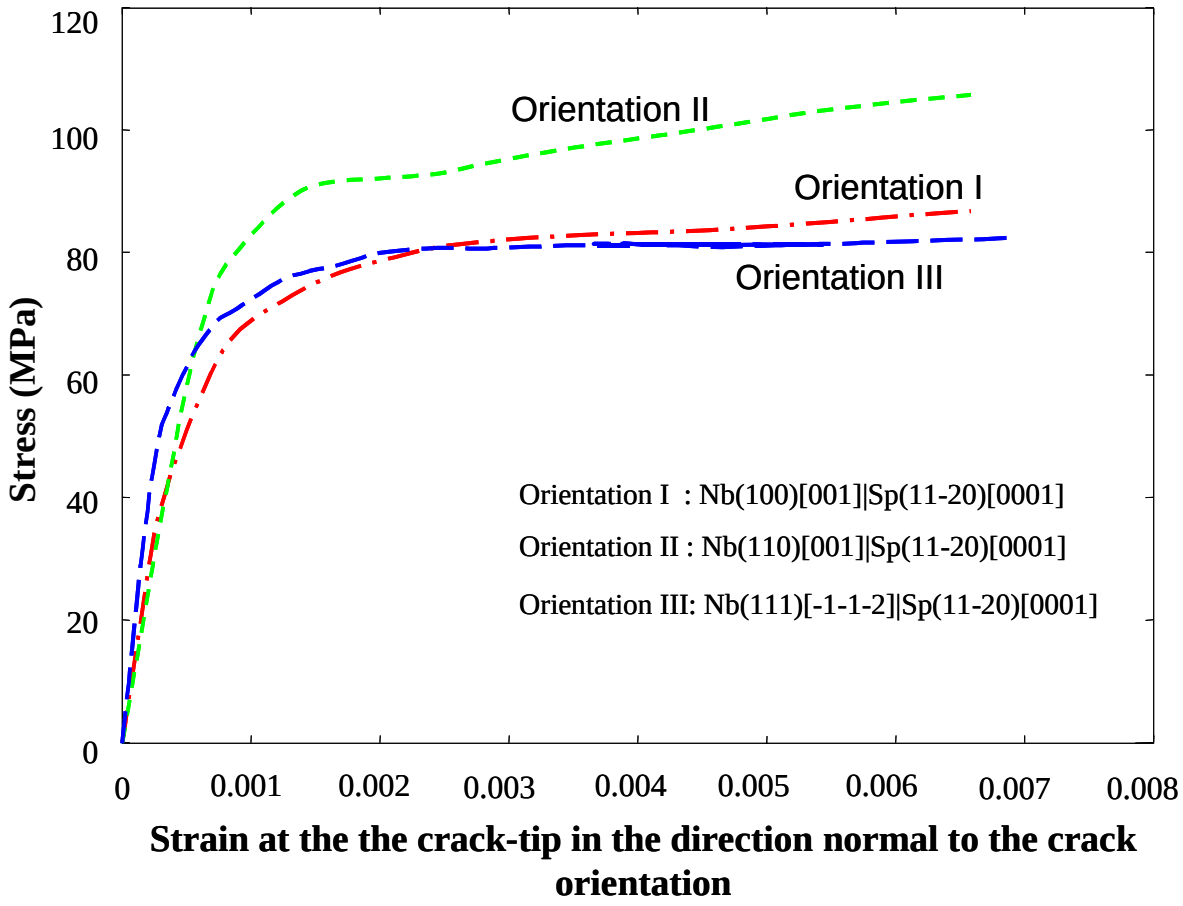

Figure 45: Stress-strain curves for orientations I, II and III of uniaxial simulation for a stationary interface crack

It can also be inferred from figure 34(a) that the plastic region developed due to plastic slip in the (1-12)[-111] system is the largest one and the plastic slip in this slip system dominates the total plastic slip (strain) region (figure 43(b)).

The orientations I and III were found to have the lowest energy release rates (see figure 31). For orientation I, the major contribution to the total slip comes from (112)[11-1], (121)[1-11], (1-21)[111], (12-1)[-111], (-211)[111] and (21-1)[1-11] slip systems (see figure 35). Similar to the procedure discussed above for orientation II (figure 31), the contribution of different slip systems in various regions around the crack tip can be identified from figure 36 for orientation I. Figure 36 shows that the maximum contribution from the polar angle range φ of 0° - 30° comes from the (1-21)[111] and (12-1)[-111] slip systems. For the polar angle range of 30° - 90° the major contribution to the plastic slip comes from (-211)[111] and (21-1)[1-11] while the contribution to the plastic slip of slip systems (112)[11-1] and (121)[1-11] is maximum for the polar angle range of 90° - 180°. The contour plots of slip on these systems along with the total accumulated slip are plotted in figures 35(a - f), and 43(a) to indicate the

activated slip system. The results on angular variation of slip (figure 36) can be seen in figure 35(a - f) for the individual slip systems, i.e. the variation of plastic slip is seen in detail for the above discussed six slip systems pointed out in figure 36. The plastic region developed due to the plastic slip in the (21-1)[1-11] system is the largest one (figure 35(f)) and the plastic slip in this slip system dominates the total plastic slip (strain) region (figure 43(a)). The large plastic slip in the (21-1)[1-11] system is due to its favourable orientation with respect to the crack front with the highest Schmidt factor of ~ -0.47 while other slip systems have smaller Schmidt factors ~ -0.408 and -0.237.

For orientation III, the major contribution to total slip comes from the (1-21)[111], (12-1)[-111], (-112)[1-11] and (-121)[11-1] slip systems (see figure 37). The major contribution of slip systems (1-21)[111] and (-112)[1-11] is in the range of 0° - 60°, while the major contribution of slip systems (-121)[11-1] and (12-1)[-111] starts from 30° and ends at 180°. The reason is the favourable orientation of the slip systems (1-21)[111] and (-112)[1-11] in the range of of 0° - 60° with highest Schmidt factor of -0.47 in this region which changes relative to loading direction to 0.21 in the range of 30° - 180°. That is why the major contribution of the slip systems (1-21)[111] and (-112)[1-11] is larger in the polar angle range of 0° - 60°. The contour plots of the slip on the above four slip systems, as well as the total slip for orientation III are plotted in Figs. 37(a - d), and 43(c) to indicate the radial variation of slipping. The contour plots in figure 38(a - d) show the same angular dependence of the plastic slip region developed around the crack tip in the four slip systems as shown in figure 37 at a radial distance of 15 μm.

The orientations IV and V, which are originally single slip orientations always had one slip system activated at the start of plastic deformation. The orientation IV always had (011)[11-1] system as primary activated slip system while orientation V always had (-211)[111] system activated as primary slip system. Figure 40 shows the major contribution to the total slip coming from (011)[11-1], (10-1)[111], (112)[11-1] systems for orientation IV where (10-1)[111] and (112)[11-1] are secondary slip systems which are activated in stage II of loading because of lower Schmidt factor ~ -0.44 as compared to the Schmidt factor of the primary system (011)[11-1] ~ -0.497. It is also prominent that the contribution of the primary slip system (011)[11-1] is the highest one. The energy release rate for orientation IV (see figure 31) shows that the slope of the increase in the energy release rate as a function of applied strain is steeper as compared to orientations I, III and V. The energy release rate for orientation V (see figure 31) has almost the same trend as orientations I and III. Figure 42 shows that the major contribution to the total slip comes from (011)[11-1], (101)[-111], (-

121)[11-1] and (-211)[111] systems for orientation V and the contribution of the primary slip system (-211)[111] is the highest one. The contour plots of the slip on the different activated slip systems, as well as the total slip are plotted in figures 39(a - c), and 43(d) for orientation IV and figures 42(a-d), and 43(e) for orientation V. For orientation IV the major plastic zones are developed due to the plastic slip in the (011)[11-1] and (10-1)[111] systems (figures 39(a) and 39(b), respectively). The plastic slip in these two systems dominates the total plastic slip (strain) zone (figure 43(d)). For orientation V the major plastic slip zones are developed due to plastic slip in the (-121)[11-1] and (-211)[111] slip systems (figures 42(b) and 42(d), respectively). The plastic slip in these two systems plays a dominating role in the total plastic slip (strain) zone (figure 43(e)).

In order to qualitatively compare the finite element results discussed above, with the experimental results of [22, 23], we consider the first three orientations, i.e. orientation I, II and III and compare the energy release rate trends with the experiments of [22, 23]. No experimental results are available for orientations IV and V, therefore, only orientations I, II and III are compared with experimental fracture energy values. The experimental results showed that the energy release rate of orientation II was always higher than that of the other two orientations I and III. The calculated energy release rate values for the three orientations I, II and III were found to be 115 J/m^2, 370 J/m^2 and 112 J/m^2, respectively, at a bonding temperature of 1400 °C. The results obtained here can be extended to other bonding temperatures, such as for 1300 °C. This can be done by using the appropriate stress-strain-curves from experiments which will require the identification of the crystal plasticity hardening parameters for these cases (as discussed in section 4.1). The studies for 1300 °C are not done here due to unavailability of stress-strain curves for this bonding temperature.

Figure 44 shows the same trend as experimentally found in [22, 23] with the highest energy release rate found for orientation II while orientations I and III were almost having the same energy release rate values during deformation. It has also been found that orientation I has slightly higher values of energy release rate than orientation III which again is in agreement with the experimental findings [22, 23].

In order to understand the phenomena involved behind this difference in energy release rates for three orientations I, II, and III, uniaxial tension test simulations were performed. Based on crystal plasticity theory the stress-strain curves of the uniaxial tension test simulations for the three orientations I, II and III are plotted in figure 45 which shows that the orientation of niobium single crystals changes the stress-strain behaviour and one can eventually see that for a specific strain value, higher stresses are induced for the case of orientation II than

orientation I and III. These higher stresses cause the higher total energy of the niobium single crystals which is given by the area under the stress-strain curve. Similar results were obtained in [142, 143] where it was found that for different specimens of stainless steel the specimens with higher uniaxial stress-strain cuves give higher fracture energies for stationary and growing cracks. It is also found in the present work that the stresses induced around the crack tip for orientation II were higher than for orientations I and III. This ultimately ends up with a higher J-integral value as shown in figure 44. The high value of induced stress for orientation II is due to the low Schmidt factor of the slip systems activated during deformation, i.e., it requires higher stresses to activate a slip system with low Schmidt factor than the slip system with high Schmidt factor. It is also found that the total slip induced in the niobium single crystals for the three orientations depict that orientation I and III always had higher plastic slip (strain) than orientation II for the same loading conditions (figures 33, 36, 37). This in fact is due to the orientation of the slip systems as the slip systems for orientation I and III have higher Schmidt factors 0.47 and 0.447 (as discussed above) and, therefore, they tend to slip more easily than the orientation II with Schmidt factor 0.408.

4.2.5 Summary

Different techniques to compute the fracture energy of an interface crack in a bimaterial specimens have been applied. A comparison of fracture energies computed with three different methods, i.e., global energy method, J-integral method and virtual crack closure technique has been made. The computed values showed the consistency in the results. Bimaterial specimens was also simulated using isotropic plasticity and crystal plasticity theory. The crystal plasticity results are compared with the experimental results and show that there is a variation in fracture energy for different orientations as measured in experiments. This is due to the plastic anisotropy of the single crystalline materials which cannot be captured by the continuum deformation plasticity theory. Based on the contribution of the plastic slip (strain) of the activated slip systems for various orientations the difference in the energy release rate has been explained. The finite element analyses results show the same trend of computed fracture energy as found in the experiments [22, 23] for three different orientations.

4.3 Effect of Thermal Residual Stresses

This section presents the results obtained from crystal plasticity finite element analyses including thermal residual stress effects. Thermal residual stresses which are induced during high temperature bonding can play a role during the fracture process as discussed below. In this section, the effect of thermal residual stresses is being studied. A comparison has been made between conventional simulations (without thermal residual stresses) and simulations with induced thermal residual stresses.

4.3.1 Introduction

By definition, the residual stress in a body is (normally) the stress remaining in that body when there are no external forces applied on the body.

Significant differences in the thermal and mechanical properties of ceramics and metals make it extremely difficult to obtain ceramic-to-metal joints with adequate mechanical integrity [115].

The reason behind it is, the mismatch in thermal and mechanical properties, induces large tensile and shear residual stresses in the region around the edge and near the interface of metal and ceramic, when cooled from the joining temperature [116]. This sometimes causes the crack to propagate out from an interface and continue to travel parallel with the interface. As mentioned above, this may be due to elastic anisotropy mismatch, which directs a crack out from the interface by kinking or bending [117, 118], it is perhaps most often caused by thermal expansion mismatch, resulting in residual normal stresses in planes normal to the interface.

In order to see the amount of thermal residual stresses induced in the bicrystal test specimens, coupled temperature-displacement analyses have been performed.

4.3.2 Finite Element Model

The finite element model is based on the experiments performed in [22, 23], as discussed in section 4.2.2. The specimens to perform four-point-bending test experiments in [22, 23] were prepared by diffusion bonding of single crystals of niobium and alumina in ultra high vacuum furnace.

The finite element model is constructed based on the information provided in [22, 23] (as discussed in section 4.2.2), but without a notch. As shown in figure 46, the finite element model of a niobium single crystal is bonded to alumina (using the bond option available in ABAQUS). Finite element models of alumina shanks and a polycrystalline niobium sheet

were joined with the corresponding niobium single crystal finite element model and an alumina finite element model using the tie constraints option available in ABAQUS.

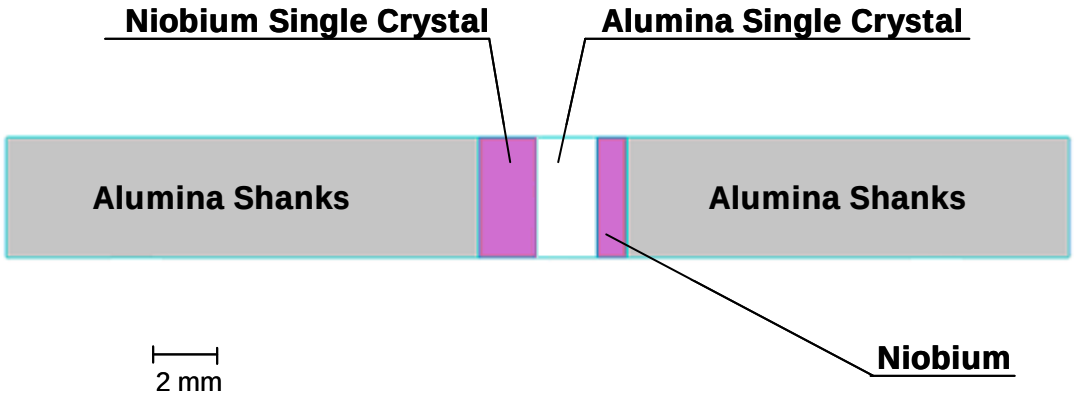

Figure 46: Four point bending test specimens without a notch during bonding

4.3.3 Finite Element Analysis

Finite element analyses were performed in two steps based upon the procedure involved in bonding of four-point bending test specimens for experimental studies.

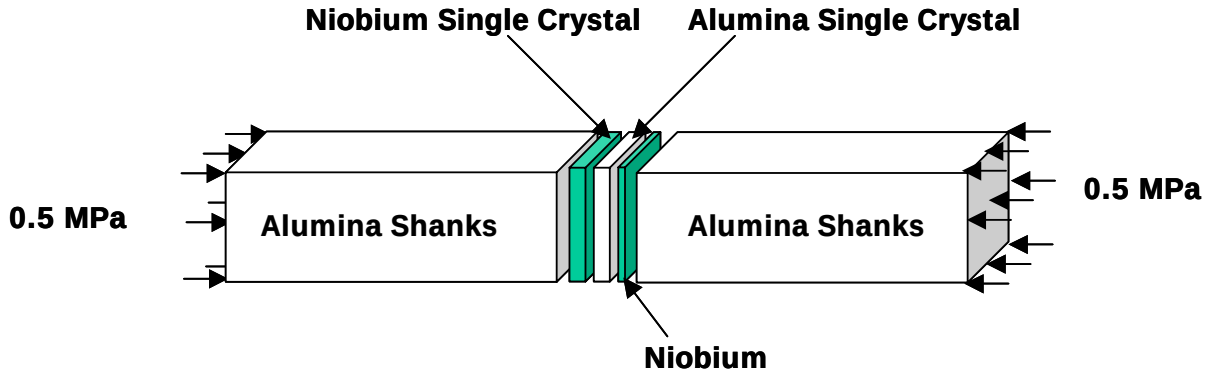

Figure 47: Four point bending test specimens without a notch stacked in the press anvil

The experimental specimens in [22, 23] were produced by diffusion bonding of single crystals of niobium and alumina in ultra high vacuum furnace. As shown in figure 47, single crystal niobium, single crystal alumina and shanks of polycrystalline alumina were stacked with an initial uniaxial pressure of 0.5 MPa. The whole stack is then placed into the ultra high vacuum furnace where the temperature was maintained up to 1400 °C. The pressure at the bonding temperature is 10 MPa.

A similar procedure has been used in finite element simulations in two steps. The first step consisted of thermo-mechanical analyses, in which the specimens is heated to a temperature of 1400 °C, simultaneously a pressure (as shown in figure 47) is applied which increased linearly from 0.5 MPa – 10 MPa with time and is controlled in such a manner that at 1400 °C the pressure was 10 MPa, as was the same as during bonding of the real structure [22, 23].

A second step consisted of thermo-mechanical analyses in which the specimens is cooled down to room temperature keeping the pressure to be 10 MPa [22, 23].

The thermo-mechanical analysis is used to compute the thermal and mechanical stresses. Thermal stresses are computed using the following relation equation (54) [98]:

$$\sigma^{th} = -E\alpha\Delta T \tag{54}$$

where E is Young's modulus, α is the thermal expansion coefficient and ΔT is the change in temperature ($\Delta T = T_{current} - T_{previous}$) with $T_{current}$ is the temperature at the current time increment while $T_{previous}$ is the temperature at the previous time increment.

The temperature at the current time increment $T_{current}$ is obtained from the energy balance, given by equation (55):

$$Q_{\sup plied} = Q_{conducted} + Q_{stored} \tag{55}$$

where $Q_{supplied}$ is the heat energy supplied to the material while $Q_{conducted}$ is the heat energy conducted through the material ($Q_{conducted} = -\varpi A\frac{\Delta T}{\Delta x}$) with ϖ is thermal conductivity, A the surface area of the material, ΔT the change in temperature, and x is the position in the material. Q_{stored} is the heat energy stored in the material ($Q_{stored} = \rho V\zeta\Delta T$) with ρ the density of the material, ζ the specific heat and V is the volume of the material.

Material properties used for the thermo-mechanical analysis are the same as described in section 4.2.3. Thermal properties for niobium are the coefficient of thermal expansion $\alpha_{Nb} = 7.3x10^{-6}K^{-1}$, thermal conductivity $\varpi_{Nb} = 53.7W\cdot m^{-1}\cdot K^{-1}$, density $\rho_{Nb} = 8.57g/cm^3$ and specific heat $\zeta_{Nb} = 268J\cdot kg^{-1}\cdot K^{-1}$, while, thermal properties of alumina are, coefficient of thermal expansion $\alpha_{Al_2O_3(0001)} = 5.8x10^{-6}K^{-1}$, thermal conductivity $\varpi_{Al_2O_3} = 35.W\cdot m^{-1}\cdot K^{-1}$, density $\rho_{Al_2O_3} = 3.985g/cm^3$ and specific heat $\zeta_{Al_2O_3} = 750J\cdot kg^{-1}\cdot K^{-1}$. The thermal properties are needed in equations (54 – 55), i.e. thermal conductivity ϖ is needed to compute $Q_{conducted}$, thermal expansion coefficient α is required to compute thermal stresses while density ρ, and specific heat ζ, is needed to compute Q_{stored}.

Due to the anisotropy in the coefficients of thermal expansion of alumina, two different thermal expansion coefficients have been used. The first one is for the (0001) orientation and the second one is for the (11-20) orientation. The thermal expansion coefficients are $\alpha_{Al_2O_3(0001)} = 5.8x10^{-6}K^{-1}$ and $\alpha_{Al_2O_3(11-20)} = 6.8x10^{-6}K^{-1}$.

At the end of the second step, residual stresses were obtained from the above analysis using the URDFIL subroutine available in ABAQUS. These stresses were then prescribed as the initial stress in the four point bend test specimens with a notch. After the inclusion of the induced thermal residual stresses a final deformation step was performed in which the finite element model with induced thermal residual stresses is deformed with an applied bending loading of 100 MPa (as shown in figure 27).

4.3.4 Results and Discussion

Usually, the niobium-sapphire interface serves as a model system as the thermal expansion coefficients of niobium and sapphire are nearly the same. In order to see the effect of thermal residual stress, the current analyses were done as discussed in the sections 4.3.1 - 4.3.3.

Figure 48, shows the J-integral versus applied load curve and as can be seen that there is a small variation in the values of J-integral through out the deformation process for the three cases, i.e., without thermal residual stress, with thermal residual stress for alumina (0001) orientation and with thermal residual stress for alumina (11-20).

If the two cases of alumina (0001) and alumina (11-20) are compared, the J-integral value is always larger at every point of the deformation for alumina (11-20) than alumina (0001). But as mentioned above the difference is really small.

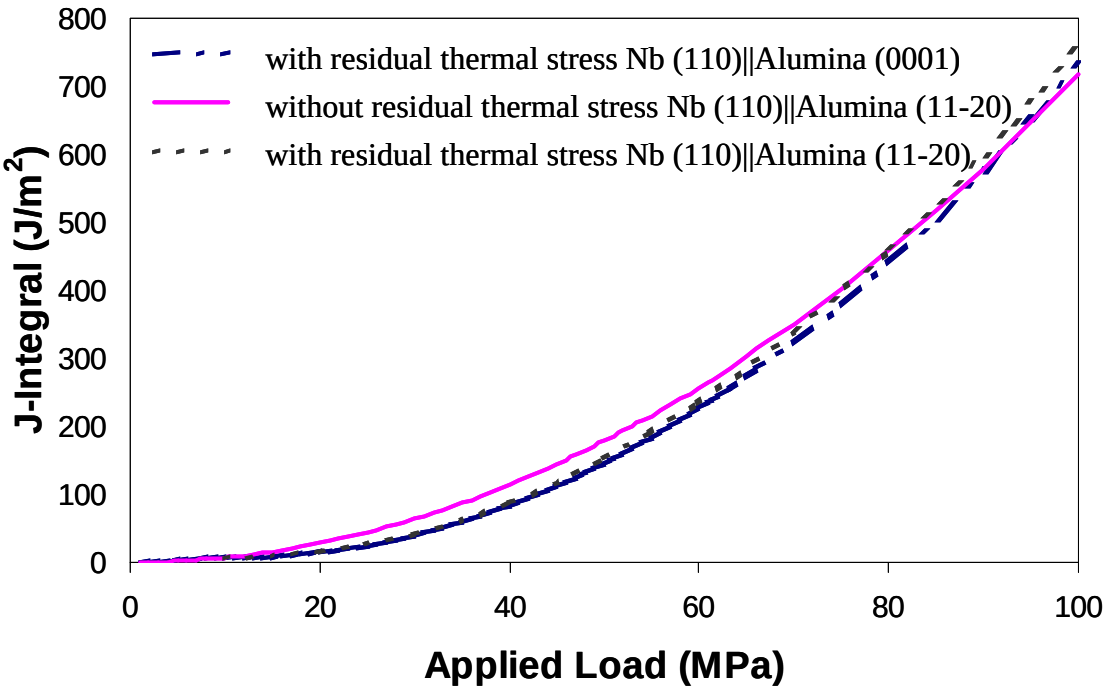

Figure 48: Effect of thermal residual stresses on J-integral value

As mentioned above the difference in thermal expansion coefficients is not so high for the niobium/alumina system up to the temperatures used for diffusion bonding, i.e. α_{Nb} = 7.3 x 10^{-6} K^{-1} while for two different orientations of alumina $\alpha_{Al_2O_3(0001)} = 5.8x10^{-6}K^{-1}$ and $\alpha_{Al_2O_3(11-20)} = 6.8x10^{-6}K^{-1}$. The ratio of α_{Nb} = 7.3 x 10^{-6} K^{-1} to $\alpha_{Al_2O_3(11-20)} = 6.8x10^{-6}K^{-1}$ is small ~ 1.073. Also, the anisotropy of the thermal expansion coefficient α of sapphire does not play a significant role in the present analyses as the ratio of $\alpha_{Al_2O_3(11-20)} = 6.8x10^{-6}K^{-1}$ to $\alpha_{Al_2O_3(0001)} = 5.8x10^{-6}K^{-1}$ is small ~1.17. Due to such small mismatch in thermal expansion coefficients (as discussed above) no significant effect of thermal residual stresses on the J-integral value is found for the niobium/alumina system.

4.3.5 Summary

The effect of thermal residual stress on J-integral has been studied in this section. As the mismatch in the thermal expansion coefficients is very small, therefore, heating of the specimens from room temperature to 1400 °C and then cooling back to room temperature did not induce high thermal residual stresses. Therefore, no significant effect on the J-integral value was found for the niobium/alumina system. It is also found that anisotropy of the thermal expansion coefficient of sapphire does not effect the J-integral values because of small differences in thermal expansion coefficients of the two different orientations.

However, for the metal/ceramic joints where this mismatch in the thermal expansion coefficients is high, e.g., in copper/alumina (ratio $\alpha_{Cu}/\alpha_{Al_2O_3} \cong 2.9$) or aluminum/alumina (ratio $\alpha_{Al}/\alpha_{Al_2O_3} \cong 4.1$) thermal residual stress effects should be taken into account using the procedure described above.

4.4 Interface Fracture Analyses Using a Cohesive Modelling Approach

This section presents the results of interface fracture of a bicrystal specimens obtained from the crystal plasticity theory based finite element simulations using a cohesive modelling approach. The effect of different cohesive law parameters, such as, cohesive strength and work of adhesion will be studied. The section also discusses the influence on fracture energy of local mode mixity, T-stresses and stress triaxiality at the interface of the bicrystal specimens. A relation will be derived to interlink the local adhesion capacity and macroscopic fracture energies.

4.4.1 Finite Element Model

The finite element model applied in the present study is based on the experiments performed in [22, 23], as already discussed in section 4.2.2. The finite element mesh consisted of 39508 plane strain four-noded quadrilateral elements. The crack propagation along the interface has been modelled by four-noded rectangular cohesive elements with zero thickness in the direction normal to the direction of crack propagation. The cohesive law used for this study is proposed by Scheider [84, 85] as already discussed in section 3.3.3.

For all simulations, both outer alumina shanks (ceramic) and the alumina single crystal at the middle of the specimens were treated as purely elastic with a Young's modulus of 390 GPa and a Poisson's Ratio of 0.27. The polycrystalline niobium sheet is always modelled with an elastic-plastic constitutive law. Young's modulus and the Poisson's Ratio for the polycrystalline niobium sheet were the same for all simulations (E = 104.9 Gpa, ν = 0.397). These elastic and plastic data are adjusted to alumina and niobium, respectively in [18, 19, 20]. The plastic behaviour of the stress-strain curve of the polycrystalline niobium sheet is approximated by a Ramberg-Osgood relation [21], which is described in the one-dimensional case by the following equation (57):

$$E_c \varepsilon = \sigma + \alpha \left(\frac{\sigma}{\sigma_0} \right)^{n-1} \sigma \tag{56}$$

Here, n denotes the hardening exponent, α the yield offset and σ_0 the yield stress. This material law is nonlinear from the beginning, but for commonly used hardening exponents ($n \geq 5$) the divergence from linearity is only slight for stresses below σ_0. The chosen plasticity theory is the deformation plasticity theory (for details see [22] and references therein), which describes not a plastic material behaviour, but a nonlinear elastic material. This means, that no unloading criterion exists which limits this theory only for monotonic loading cases. Selection

of this theory is not crucial in the current study as during all the presented simulations the niobium polycrystalline sheet is found to behave elastically (which was also the case during the experiments [22, 23]). The parameters of the above equation are adjusted to the niobium stress-strain curves in [23]. The parameters used are n = 6, σ_0 = 180 MPa and α = 0.3.

For the case of crystal plasticity, single crystalline niobium is modelled using the hardening law of Bassani & Wu (BW) [62, 63]. The hardening parameters for each slip system are derived in [14] and have already been discussed in detail in section 4.1. The hardening parameters used for each family of slip systems, i.e. (110)[111] and (112)[111], are given below.

Table XII: Hardening parameters for the Bassani & Wu (BW) hardening law

	τ_o (MPa)	τ_s (MPa)	h_o (MPa)	h_s (MPa)	γ_o	γ_{oI}	$f_{\alpha\beta}$	$f_{\alpha\beta I}$	q	q_I
(110)[111]	13.7	8.4	292.26	0.001	0.0075	0.48	3.3	1.66	0.289	0.2315
(112)[111]	13.07	10.34	25.033	24.227	0.04	0.039	0.49	0.14	0.01	0.011

Finite element analyses of crack growth have been performed for three different cases, i.e. when niobium (110)[001] is bonded with alumina (11-20)[0001], niobium (100)[001] is bonded with alumina (11-20)[0001], and niobium (111)[-1-12] is bonded with alumina (11-20)[0001]. Parameteric studies have been performed to study the effect of cohesive law parameters, such as, cohesive strength and cohesive energy (also known as work of adhesion).

4.4.2 Results and Discussion

4.4.2.1 Effect of Cohesive Law Parameters on Fracture Energy

Cohesive law parameters are selected based on the reported values in [26, 27, 28, 42, 119, 120] for the niobium/alumina system. An approximated work of adhesion value of 1 J/m^2 was reported in [119] while a value ranging from 1 - 4 J/m^2 was reported in [42, 120]. Ab-initio calculations performed on Nb(111)/Alumina(0001) in [26 - 28] reported the value of work of adhesion to be 9.8 J/m^2. This shows that a variety of values of work of adhesions have been reported by different researchers. Therefore, it is necessary to perform parameter studies in order to see the influence of the different reported values of work of adhesion in the range of 1 – 10 J/m^2.

In the following, crack growth analyses are performed with different sets of values of cohesive law parameters, such as, cohesive strength and work of adhesion. We firstly study the effect of cohesive strength on the J-resistance curves of niobium (110)[001]/alumina (11-

20)[0001] bicrystal specimens. Later we also compare the results for the case when the cohesive strength is kept constant while the cohesive energy is varied. The ultimate goal of this parametric study is to find a correlation between the local adhesion capacity and the macroscopic fracture energy for the metal/ceramic orientations analyzed.

Three different values of cohesive energy (work of adhesion) reported in [26, 27, 28, 42, 118, 120] have been used, i.e., 1 J/m^2, 4 J/m^2, and 9.8 J/m^2.

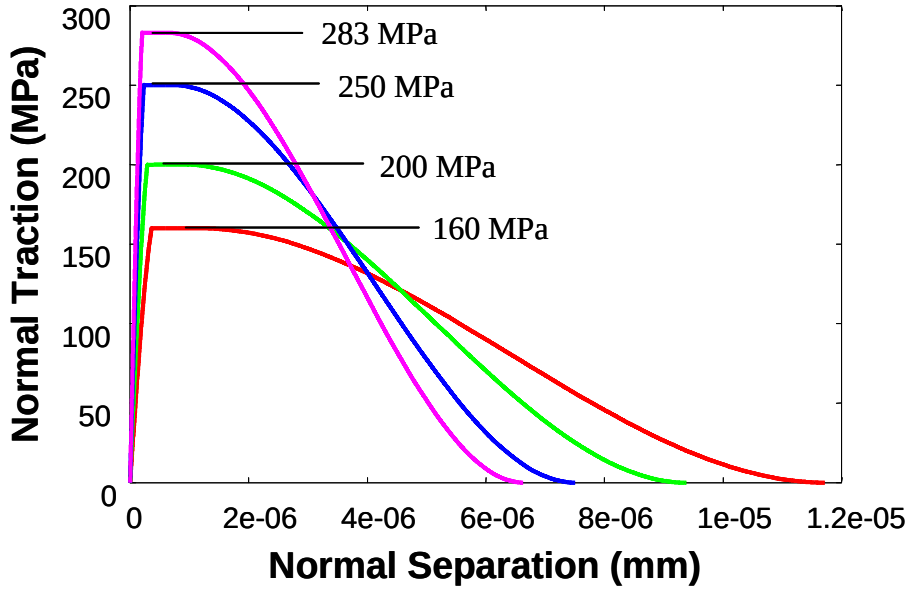

Figure 49: Cohesive law curve of various values of cohesive strength for constant work of adhesion (Γ_0 = 1 J/m^2)

The effect of cohesive strength on fracture energy has been studied by keeping the work of adhesion constant. The cohesive law curves for various values of cohesive strength at a constant work of adhesion are plotted in figure 49. The J-resistance curves for the work of adhesion of 1 J/m^2 are shown in figure 50. The results clearly show that by increasing the cohesive strength value while keeping the cohesive energy constant, the fracture resistance increases. This is due to the higher plastic energy dissipation around the crack tip. It is also found that the amount of crack length to reach the steady state crack growth increases with increasing cohesive strength. This behaviour can also be explained in terms of the stress level or traction (normal force per unit surface area acting between the niobium and alumina surfaces) ahead of the crack tip, i.e., for higher cohesive strength values, the traction (normal stress) required at the crack front to advance the crack is higher, and hence a larger applied load is required. On the other hand, a lower cohesive strength corresponds to a smaller applied load required to advance the crack.

The plastic dissipation rate as a function of normalized crack length for various cohesive strength values is plotted in figure 51. For all positions of crack tip the plastic dissipation rate is computed by the following equation (57) [39]:

$$G_{pl} = \frac{\left(E_{a_k}^{pl} - E_{a_l}^{pl}\right)}{Bda} \tag{57}$$

where G_{pl} is the plastic dissipation rate, $E_{a_k}^{pl}$ and $E_{a_l}^{pl}$ are the plastic energies at crack lengths a_k and a_l while Bda is the crack front area.

The plastic dissipation rate increases as the cohesive strength increases. It is also shown in figure 51, that the plastic dissipation rate is initially high and decreases as the steady state crack growth is reached. This decrease in plastic energy dissipation increases as the cohesive strength increases. This is due to the fact that during the initial stage of crack growth when the crack tip is sharp, a higher amount of plastic dissipation is present which decreases eventually as the crack tip starts to blunt. Also, in terms of stress level, the higher the cohesive strength (peak of the cohesive law curve, as shown in figure 49) meaning higher normal stress (the stress at any point of the cohesive law curve) at the crack tip causing higher plastic energy dissipation rates during the initial stages of crack growth.

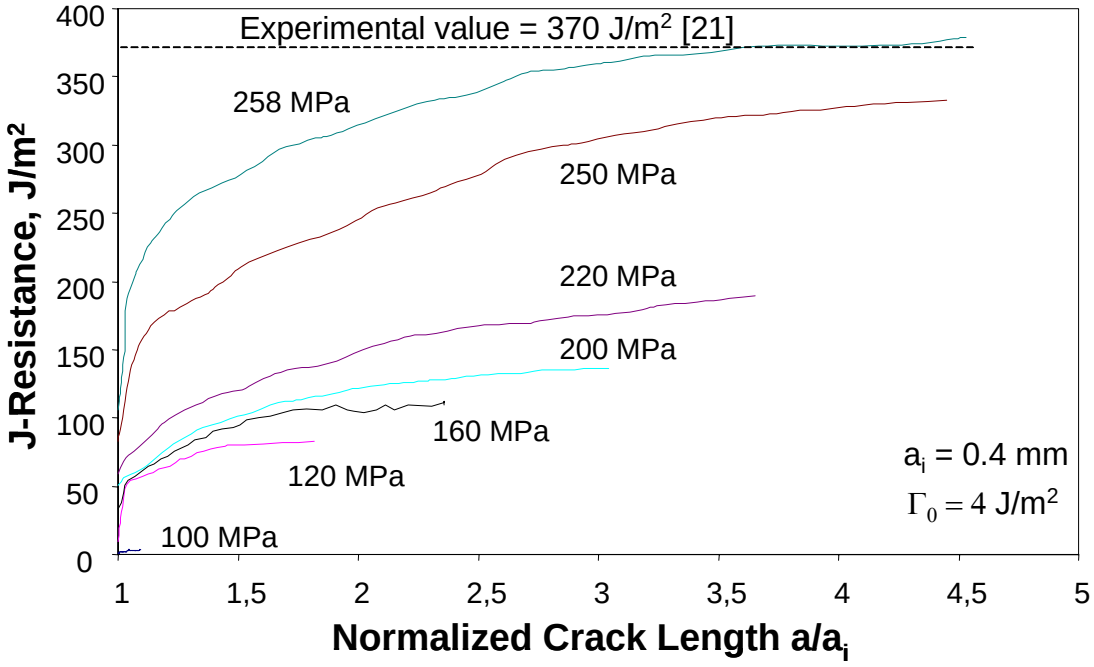

Figure 50: J-resistance curves for different values of cohesive strength ($\Gamma_0 = 4$ J/m^2)

As shown in figure 50, the experimental fracture energy value of 370 J/m^2 is reached when the cohesive strength was assumed to be 258 MPa for the work of adhesion value of 4 J/m^2.

Similar studies are done for the work of adhesion value of 1 J/m^2 and 9.8 J/m^2. The cohesive law parameters identified for the three different values of work of adhesion are given in Table XIII:

Table XIII: Cohesive model parameters for Nb(110)[001]|Al_2O_3(11-20)[0001]

Work of adhesion [J/m^2]	Cohesive strength [MPa]	Steady state fracture energy, J_c [J/m^2]
1	283	370.6
4	258	371
9.8	225	372

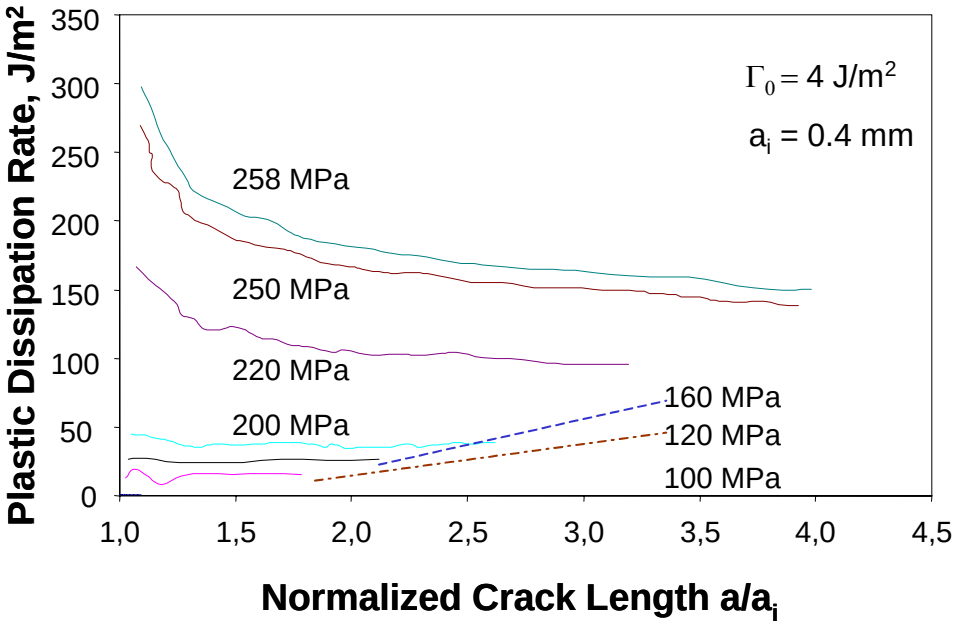

Figure 51: Plastic dissipation rate vs. normalized crack length (Γ_0 = 4 J/m^2)

Fracture energies as a function of cohesive strength to yield stress ratio (σ_c/σ_y) have been plotted in figure 52 for three different work of adhesion values at steady state crack growth. These curves show that as the cohesive strength to yield stress ratio (σ_c/σ_y) increases the fracture energy at the steady state crack growth also increases. This increase is gradual until the cohesive strength to yield stress ratio (σ_c/σ_y) is approx. 4.4. As soon as this value is reached the slope of the fracture energy curve increases which is due to the high plastic energy dissipation according to the higher number of activated slip systems. As discussed in section 4.2.4, the reason for the higher number of activated slip systems is that, as the cohesive strength is increased the resolved shear stress of the slip systems with lower Schmidt factor also increases until it reaches the yield stress of such slip system. As soon as the resolved shear stress becomes equal to the yield stress, the slip systems with lower Schmidt factor are activated. This can also be seen in figure 32, where slip systems with the highest Schmidt factor (1-12)[-111], (-211)[111] and (211)[-111] systems with Schmidt factors ~

-0.4714, -0.2357 and -0.408, respectively, are shown. Due to the highest Schmidt factor ~ -0.4714 of (1-12)[-111] system, it is the first slip system which is activated. As the deformation process still continues, stresses around the crack tip also increase, causing other slip systems to activate, e.g. (-211)[111] and (211)[-111] slip systems. This activation of slip systems continues as the stresses around the crack tip increase.

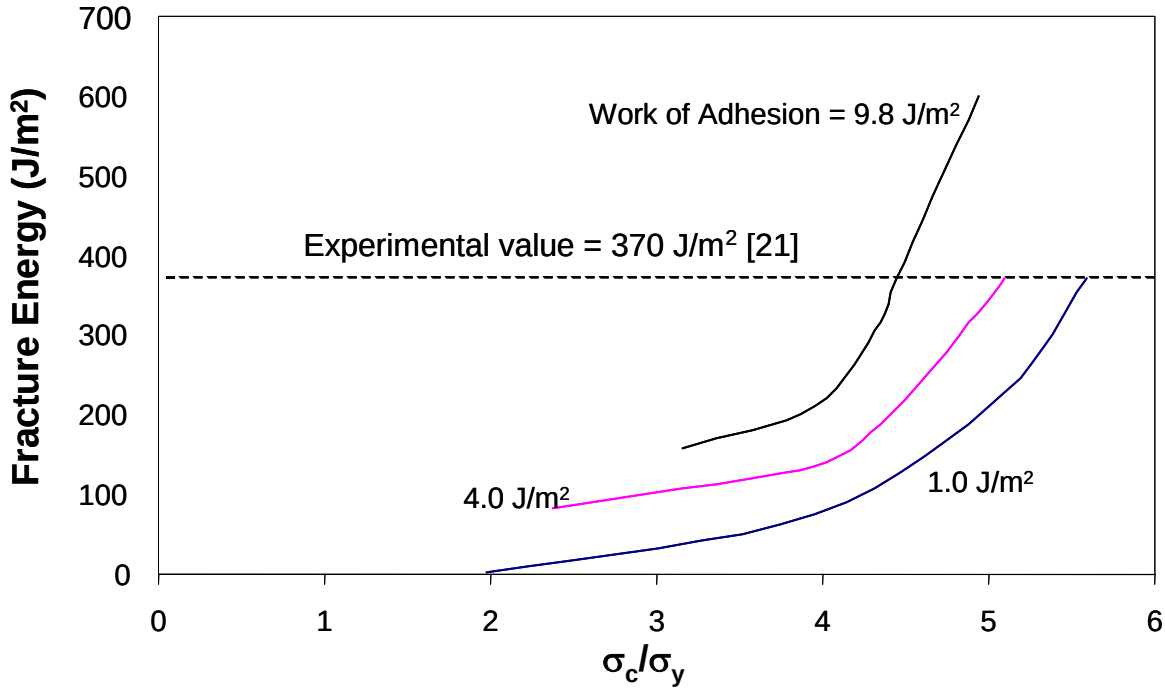

Figure 52: Fracture energy vs. cohesive strength (σ_c) to yield stress (σ_y) ratio at steady state crack growth for different work of adhesion, Γ_0 (Nb(110)[001]|Al_2O_3(11-20)[0001])

In order to reach up to the experimental results, different work of adhesion values yield different cohesive strength to yield stress ratios (σ_c/σ_y). The values of cohesive strength to yield stress ratio (σ_c/σ_y) were found for three different work of adhesion values, 1 J/m^2, 4 J/m^2, and 9.8 J/m^2 to be 5.59, 5.095, and 4.443, respectively. In a similar fashion the fracture energy is plotted as a function of the work of adhesion for different values of cohesive strength at steady state crack growth, as shown in figure 53. It shows that a linear relation exists between fracture energy and work of adhesion. These results show that fracture energy depends more strongly on the cohesive strength than on work of adhesion.

Similar studies have been done for the other two orientations, i.e., when niobium (100)[001] is bonded with alumina (11-20)[0001] and niobium (111)[-1-12] is bonded with alumina (1-20)[0001]. Figures 54 and 56 show the plots of the fracture energies as a function of cohesive strength for three different values of work of adhesion at steady state crack growth. Figure 54 shows the fracture energy results for a niobium (100)[001]|alumina (11-20)[0001] interface and figure 56 for the niobium (111)[-1-12]|alumina (11-20)[0001] interface. The plot in figure

54 shows that as the cohesive strength increases the fracture energies are almost linear and when the value of the cohesive strength reaches the range of 200 - 210 MPa (i.e., $\sigma_c/\sigma_y \cong 5$) the slopes of the fracture energy curves increase. As discussed before, the reason is higher plastic energy dissipation due to the higher number of slip systems being activated. The similar (as seen in figure 52) trend is depicted from figure 56 for niobium (111)[-1-12]|alumina (11-20)[0001] interfaces and the change in the slope of the fracture energy curve is again due to the higher number of slip systems being activated. As discussed before, the reason for the higher number of activated slip systems is that, as the cohesive strength is increased the resolved shear stress of the slip systems with lower Schmidt factor also increases until it reaches the yield stress of such slip systems.

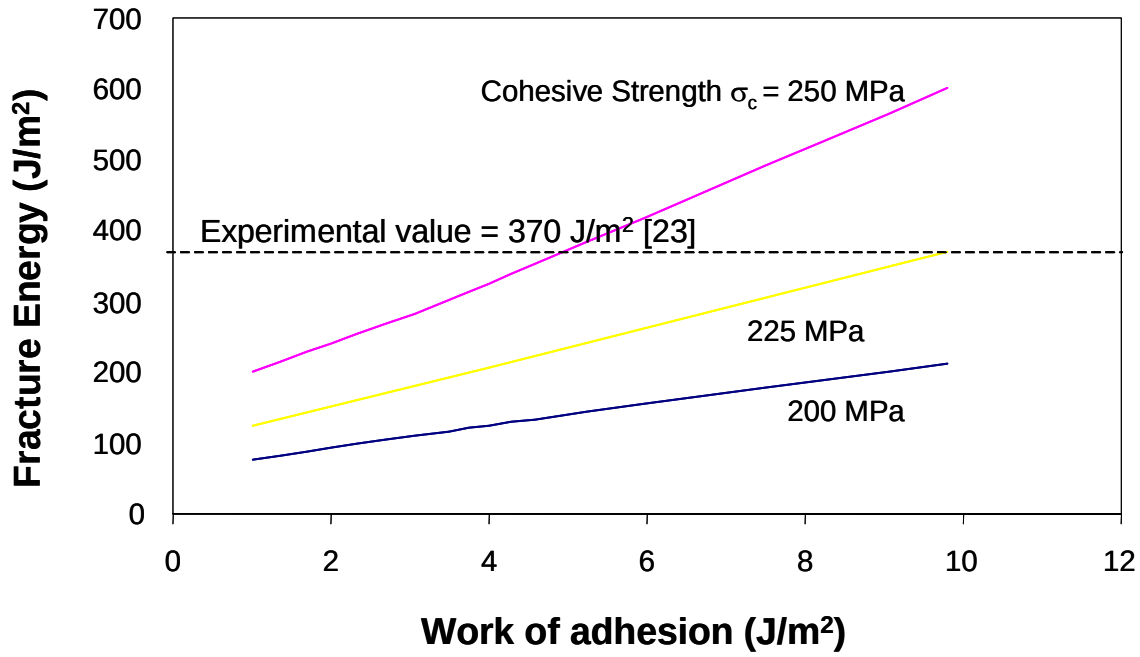

Figure 53: Fracture energy vs. work of adhesion at steady state crack growth for the Nb(110)[001]|Al_2O_3(11-20)[0001] interface crack

The fracture energy is replotted as a function of the work of adhesion for different values of cohesive strength at steady state crack growth in figure 55 for niobium (100)[001]| Al_2O_3 (11-20)[0001] interface and in figure 57 for niobium (111)[-1-12]| Al_2O_3 (11-20)[0001] interface. As the work of adhesion increases, the fracture energy also increases but the change is gradual when compared to the increase in fracture energy due to a change in cohesive strength.

These results show that the fracture energy is more sensitive to cohesive strength than to the work of adhesion. It is also found that as the cohesive strength increases the fracture energy increases. It is also seen during the simulations that the slope of the fracture energy curve increases when the number of activated slip systems increases. The reason for the higher number of activated slip systems is that, as the cohesive strength is increased the resolved

shear stress of the slip systems with lower Schmidt factor (e.g., ~ -0.2) also increases until it reaches the yield stress of the slip system. Therefore, as soon as the resolved shear stress becomes equal to the yield stress, the slip systems are activated. And as explained before, this activation of slip systems continues as the stresses around the crack tip increase.

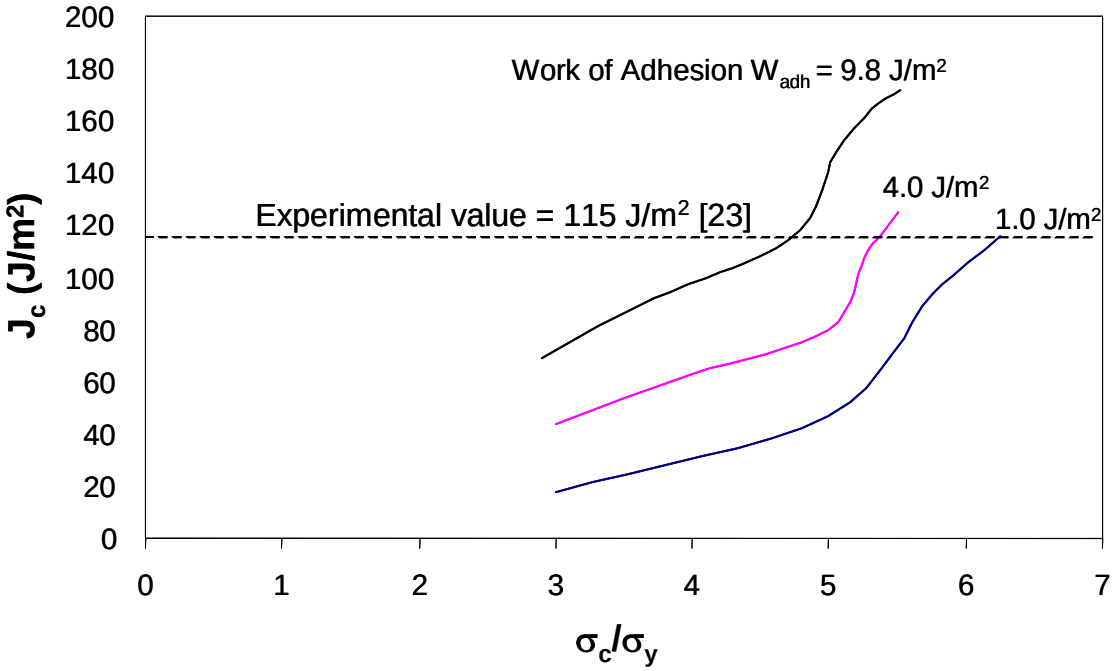

Figure 54: Fracture energy vs. cohesive strength (σ_c) to yield stress (σ_y) ratio at steady state crack growth for different values of work of adhesion, W_{adh} for the Nb(100)[001]|Al_2O_3(11-20)[0001] interface crack

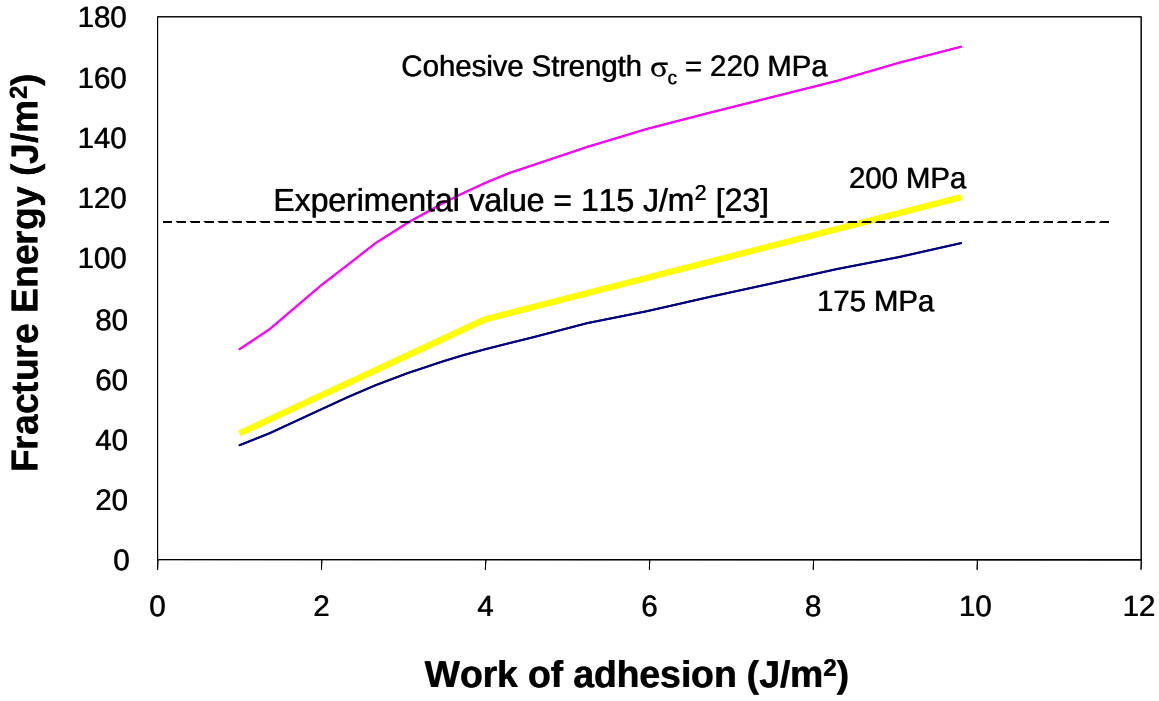

Figure 55: Fracture energy vs. work of adhesion at steady state crack growth (Nb(100)[001]|Al_2O_3(11-20)[0001])

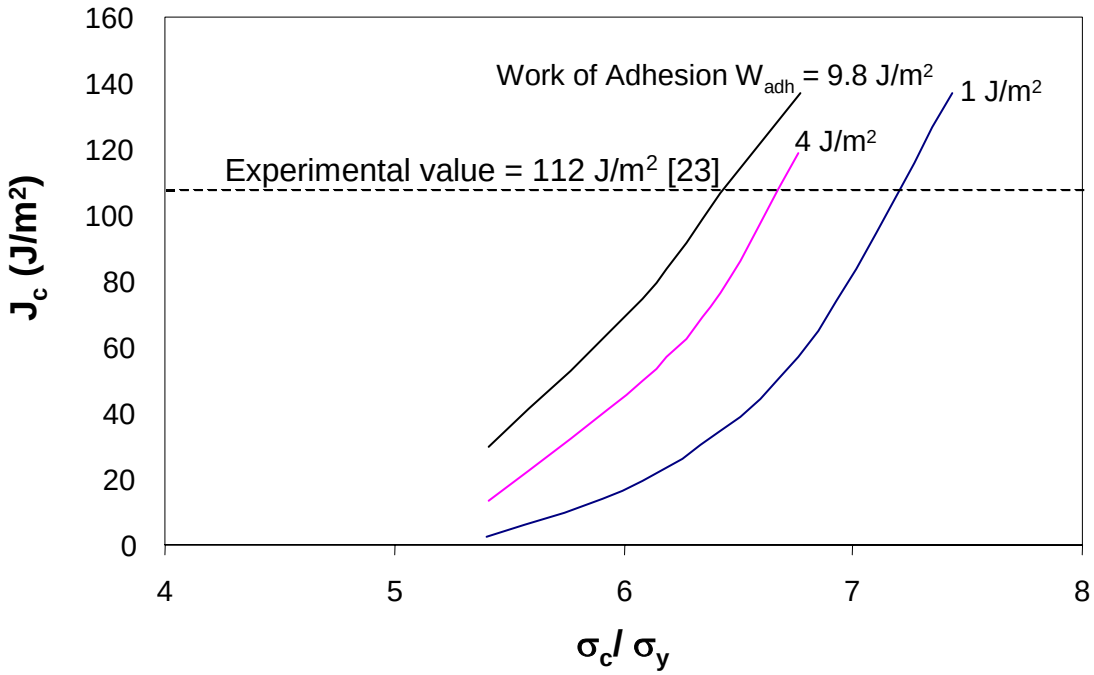

Figure 56: Fracture energy vs. cohesive strength (σ_c) to yield stress (σ_y) ratio at steady state crack growth for different values of work of adhesion, W_{adh} for the Nb(111)[-1-12]|Al_2O_3(11-20)[0001] interface crack

The cohesive law parameters identified for the three different values of work of adhesion are given in Table XIV for niobium (100)[001]|Al_2O_3(11-20)[0001] interfaces [see captions below].

Table XIV: Cohesive model parameters for the system Nb(100)[001]|Al_2O_3(11-20)[0001]

Work of adhesion (J/m^2)	Cohesive strength (MPa)	Steady state fracture energy J_c (J/m^2)
1	250	116
4	215	115.8
9.8	190	114.8

The results in Table XIV show that as the work of adhesion increases the cohesive strength required to reach the experimental fracture energy value decreases. The values of cohesive strength for the niobium (100)[001]|Al_2O_3(11-20)[0001] interface crack are found to be 250 MPa, 215 MPa, and 190 MPa for three different work of adhesion values of 1 J/m^2, 4 J/m^2 and 9.8 J/m^2, respectively.

Table XV: Cohesive model parameters for Nb(111)[-1- 12]|Al_2O_3(11-20)[0001] system

Work of adhesion (J/m^2)	Cohesive strength (MPa)	Steady state fracture energy J_c (J/m^2)
1	214	112
4	198	111.8
9.8	193	113

The cohesive law parameters identified for the three different values of work of adhesion are given in Table XV for the niobium (111)[-1-12]|alumina (11-20)[0001] interface.

In this section the effect of cohesive law parameters, such as cohesive strength and work of adhesion on fracture energy is presented. The results show a stronger influence of the cohesive strength on fracture energy as compared to work of adhesion. It is also seen in the simulations that the slope of fracture energy increases as the number of activated slip systems increases (see figure 52) causing higher plastic energy dissipation. The results presented in this section provide insight in the role of cohesive strength and work of adhesion with respect to the fracture energy which will help experimentalists in order to design improved bimaterial interfaces by varying cohesive strength and work of adhesion. One example of such studies has been presented in the experimental work [136] where the influence of impurities on the fracture energies of the niobium/alumina interface was studied: The work of adhesion was varied by doping elements, such as silver, at the interface. It was found that as the fraction of doped silver increases at the interface, the work of adhesion decreases causing the fracture energy to decrease also.

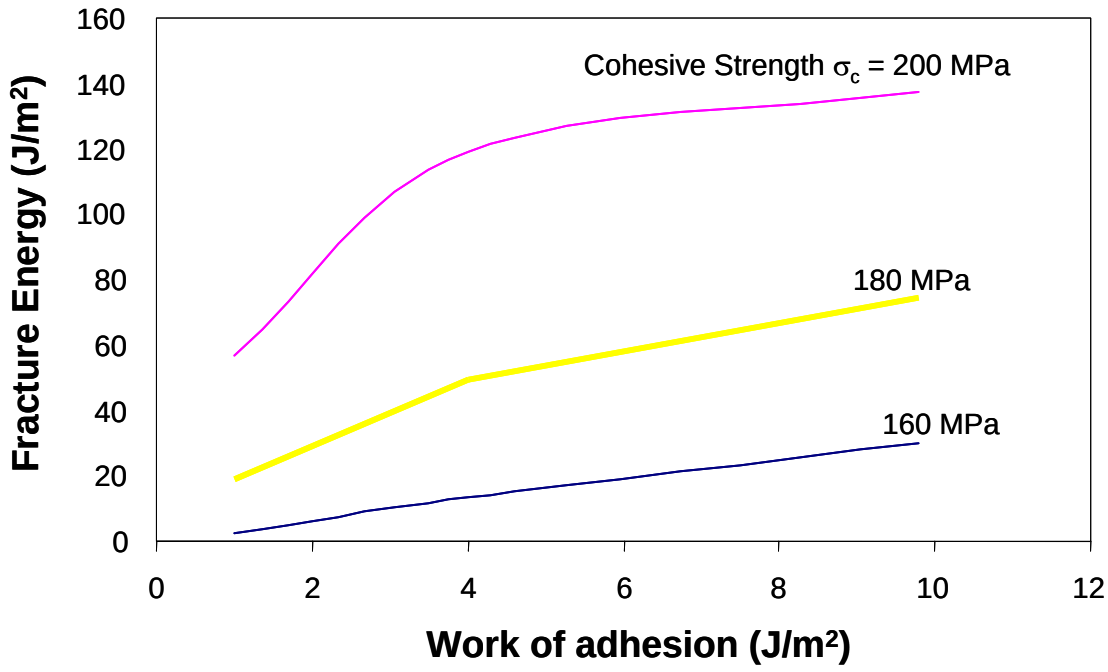

Figure 57: Fracture energy vs. work of adhesion at steady state crack growth along a Nb(111)[-1-12]|Al_2O_3(11-20)[0001] interface

In this work, the effect of different cohesive law parameters, such as work of adhesion (W_{adh}) and cohesive strength (σ_c) on fracture energy is studied. As discussed before, the work of adhesion (W_{adh}) values were varied in the range of 1 - 9.8 J/m^2 while cohesive strength (σ_c) values were found to be in the range of 190 – 283 MPa with corresponding critical normal separation (δ_c) at complete failure in the range of 6.625 – 83 nm for three different orien-

tations of the niobium/alumina single crystalline interfaces. Xu & Needlemann [38, 78] and Kysar [35, 36] have performed studies on copper/alumina bicrystal interfaces fracture and have used similar cohesive law parameters. The parameters used were, work of adhesion (W_{adh}) equals to 1.0 while cohesive strength (σ_c) was in the range of 122 – 250 MPa with corresponding normal separation (δ_c) at complete failure being in the range of 15 – 76.2 nm.

In the following, a correlation among cohesive strength (σ_c), work of adhesion (W_{adh}) and yield stress (σ_y) has been obtained by using least square surface fitting technique (available in MATLAB [141]) to estimate the cohesive strength (σ_c) for three differently oriented niobium/alumina interfaces. A surface has been plotted in figure 58 using cohesive strength (σ_c) and work of adhesion (W_{adh}) given in tables XIII, XIV and XV, and yield stress (σ_y) for each orientation, i.e. 40 MPa for Nb(100)[001]|Al_2O_3(11-20)[0001], 50.98 for Nb(110)[001]|Al_2O_3(11-20)[0001], and 29,6 for Nb(111)[-1-12]|Al_2O_3(11-20)[0001]-interfaces.

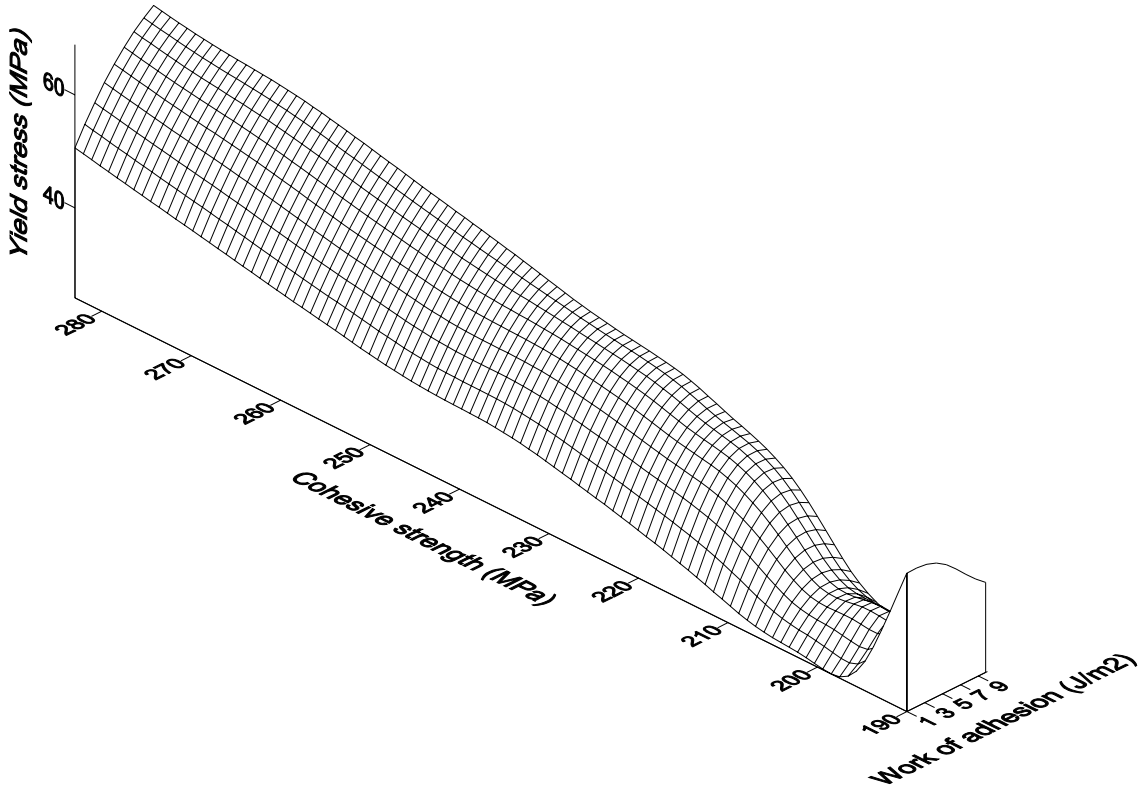

Figure 58: Surface plot of fracture energy vs. work of adhesion and cohesive strength for three different orientations of niobium/alumina-interfaces

In figure 58 it can be seen that there exists a saddle point when cohesive strength is in the range 190 – 200 MPa. This is due to the fact that for orientation II, i.e. the case when yield stress (σ_y) is 50.98 MPa, the cohesive strength values were always found to be higher than 225 MPa for different values of work of adhesion (see table XIII) . Therefore, the surface plot

in figure 58 shows such a saddle point, this is due to the extrapolation of cohesive strength for orientation II below 225 MPa. This saddle point neither has any significance in reality nor any effect on current calculations during the present study.

This correlation has been derived for three different orientations of niobium/alumina interfaces, i.e. Nb(110)[001]|Al_2O_3(11-20)[0001], Nb(100)[001]|Al_2O_3(11-20)[0001], and Nb(111)[-1-12]|Al_2O_3(11-20)[0001], using least square surface fitting technique in MATLAB [141] and the correlation is given as:

$$\sigma_c = 6.112\left(\alpha_i \cdot \frac{W_{adh}}{W_0}\right)^{-0,0919} \cdot \sigma_y \qquad (58)$$

where W_0 is the reference work of adhesion taken to be 1 J/m^2 for this study while α_i is the parameter depending on the orientation of niobium/alumina bicrystal specimens. The value of α_i is found to be 1.0 for Nb(100)[001]|Al_2O_3(11-20)[0001], 1.35 for Nb(110)[001]|Al_2O_3(11-20)[0001], and 0.853 for Nb(111)[-1-12]|Al_2O_3(11-20)[0001]-interfaces.

This correlation can be used to estimate the cohesive strength (σ_c) for a given work of adhesion (W_{adh}) and yield stress (σ_y) for any of the three orientations of niobium/alumina interfaces.

4.4.2.2 Stresses along the Crack Front ahead of the Crack Tip

In this section the stresses ahead of stationary and growing interface cracks in the niobium/alumina system are examined. The stress state ahead of stationary and growing interface cracks is an important factor which controls the local mode mixity at and ahead of the crack tip. The local mode mixity strongly influences the fracture energy of bimaterial interfaces (as will be discussed later in section 4.4.4). First the case of a stationary crack tip is considered. The normal opening stress σ_{11} and the shear stress σ_{12} are plotted as a function of distance ahead of the crack tip in figure 59.

Figure 59 shows that the normal opening stress along the crack front of the stationary crack tip of orientation II is higher than that of orientations I and III. This was also found during the uniaxial tension test simulations without crack propagation as discussed in section 4.2.4. The shear stresses along the crack front of the stationary crack tip σ_{12} are essentially the same for all three orientations I, II and III and are almost negligible as compared to the normal opening stresses σ_{11}. The results show that normal opening stresses (σ_{11}) provide a major contribution to the stress state ahead of the stationary crack tip as compared to the shear stresses (σ_{12}) leading to a low local mode mixity ratio at the crack tip of niobium/alumina specimens (discussed in detail in section 4.4.4).

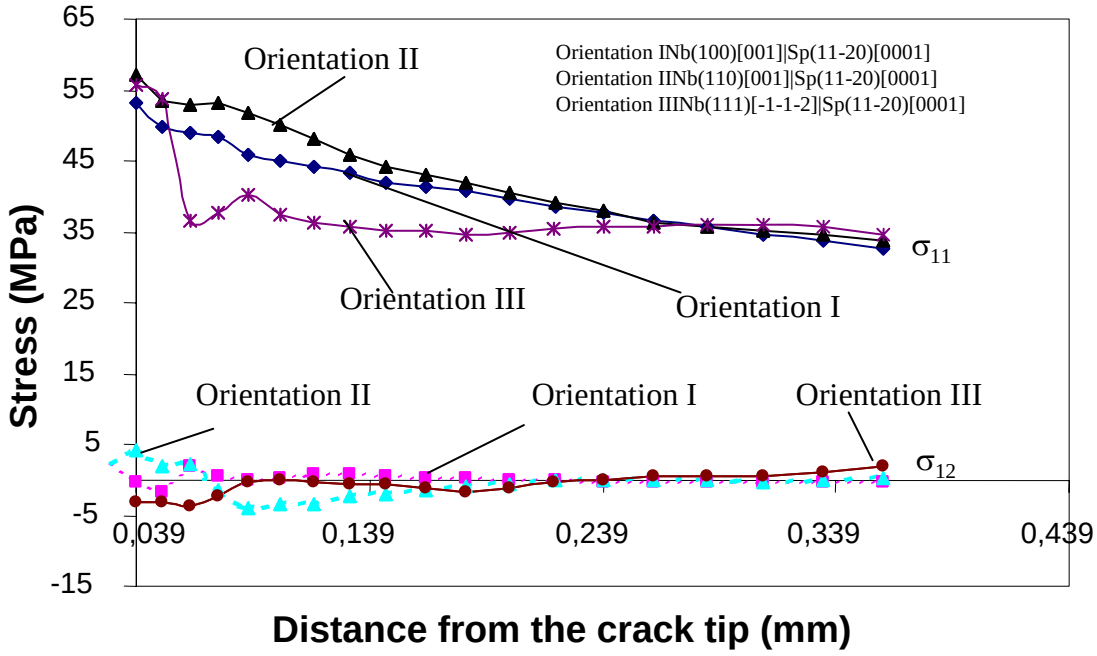

Figure 59: Stresses ahead of the tip for the case of a stationary interface crack of various Nb|Al_2O_3-orientations

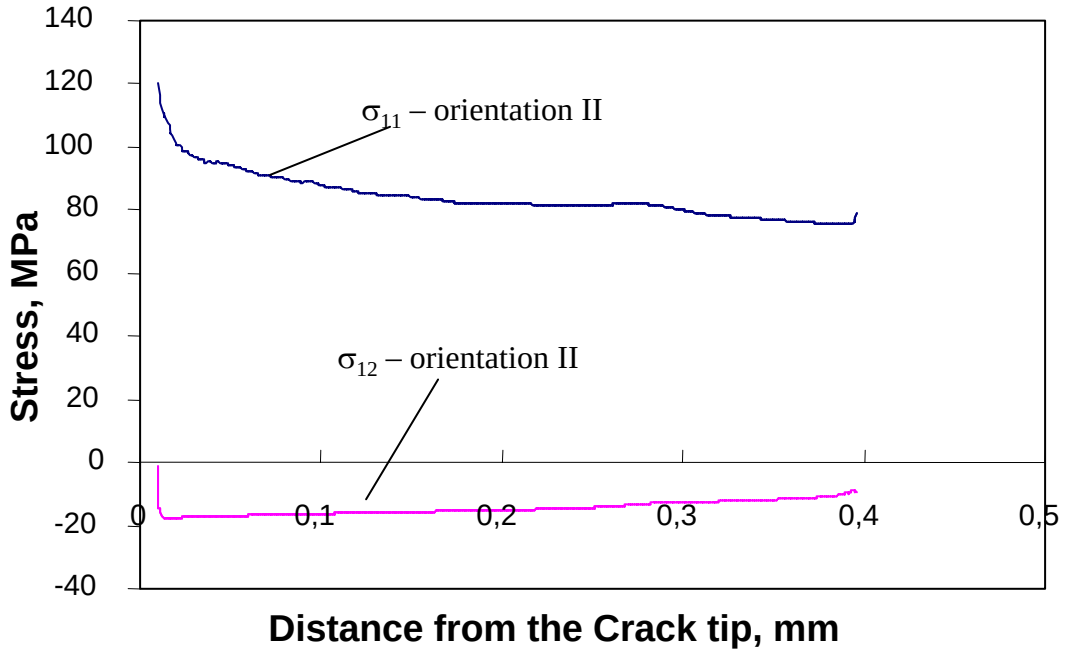

Figure 60: Stress ahead of the crack tip of the growing crack after 10.3 µm growth for the Nb(110)[001]|Al_2O_3(11-20)[0001]-interface (orientation II)

Finally, the stress state for the case of a growing interface crack of the Nb(110)|Al_2O_3(11-20)[0001] system is plotted in figure 60. The growing interface crack is simulated using the cohesive model (as discussed in section 4.4.2) for the Nb(110)|Al_2O_3(11-20)[0001] system with work of adhesion = 4 J/m^2, and cohesive strength = 160 MPa. The stress state ahead of

the crack tip is plotted for the growing crack after 10.3 μm growth of an initially 0.4 mm long crack in figure 60.

Figure 60 shows that the shear stress along the crack front is almost negligible as compared to the normal opening stress. Therefore, mode II crack loading is small compared to mode I crack tip loading.

4.4.2.3 Local Mode Mixity at the Crack Tip

The local mode mixity at the crack tip is defined by the local phase angle ψ'. The variation in the local phase angle ψ' may change the response of the crack tip upon loading on a bonded interface in metal/ceramic bimaterial systems. The local phase angle ψ' describes the mode mixity at the crack tip and is not necessarily equal to the external loading phase angle and this difference comes from the mismatch in elastic and thermal properties of the materials involved.

According to Wang [140] the local phase angle ψ' depends on some characteristic length L, the distance from the crack tip *r*, and the bimaterial parameter ε, where ε is given by:

$$\varepsilon = \frac{1}{2\pi}\ln\left(\frac{1-\beta}{1+\beta}\right) \tag{59}$$

and β is Dundurs second parameter:

$$\beta = \frac{1}{2}\frac{\mu_1(1-2\upsilon_2)-\mu_2(1-2\upsilon_1)}{\mu_1(1-\upsilon_2)-\mu_2(1-\upsilon_1)} \tag{60}$$

with μ_1 and μ_2 being the shear modulus of material 1 and 2 while ν_1 and ν_2 being Poisson's Ratios of material 1 and 2, respectively.

The geometry of the specimens also influences the local phase angle ψ' and is taken into account via some characteristic length, L such as the crack length *a*.

The local phase angle ψ' at a distance *r* from the crack tip is given by:

$$\psi' = \psi - \varepsilon\ln\left(\frac{L}{r}\right) \tag{61}$$

where ψ is the loading phase angle given by, $\psi = \tan^{-1}(2\varepsilon)$. The value of *r* in atomic scale sense is taken to be of the order *b*, the Burgers vector.

This local phase angle ψ' and the energy release rate $G_c(\psi')$ when plotted, give the failure locus as shown below in figure 61, Cao & Evans [122].

The criterion for interface crack growth is given in terms of local phase angle ψ' as:

$$|G(\psi')| = |G_c(\psi')| \tag{62}$$

where $G_c(\psi')$ is the energy release rate at fracture while $G(\psi')$ is the actual energy release rate of the bimaterial system. Therefore, according to the above criterion a bimaterial system will fail if $|G(\psi')| = |G_c(\psi')|$. This criterion defines a failure locus, which is a property of the interface, called the interface toughness curve.

Cao & Evans [122] measured the fracture resistance for a range of phase angles of a model bimaterial interface (glass/aluminum) bonded using epoxy as bonding agent. Their experimental studies revealed that the critical strain energy release rate increases with increase in phase angle, as shown in figure 61.

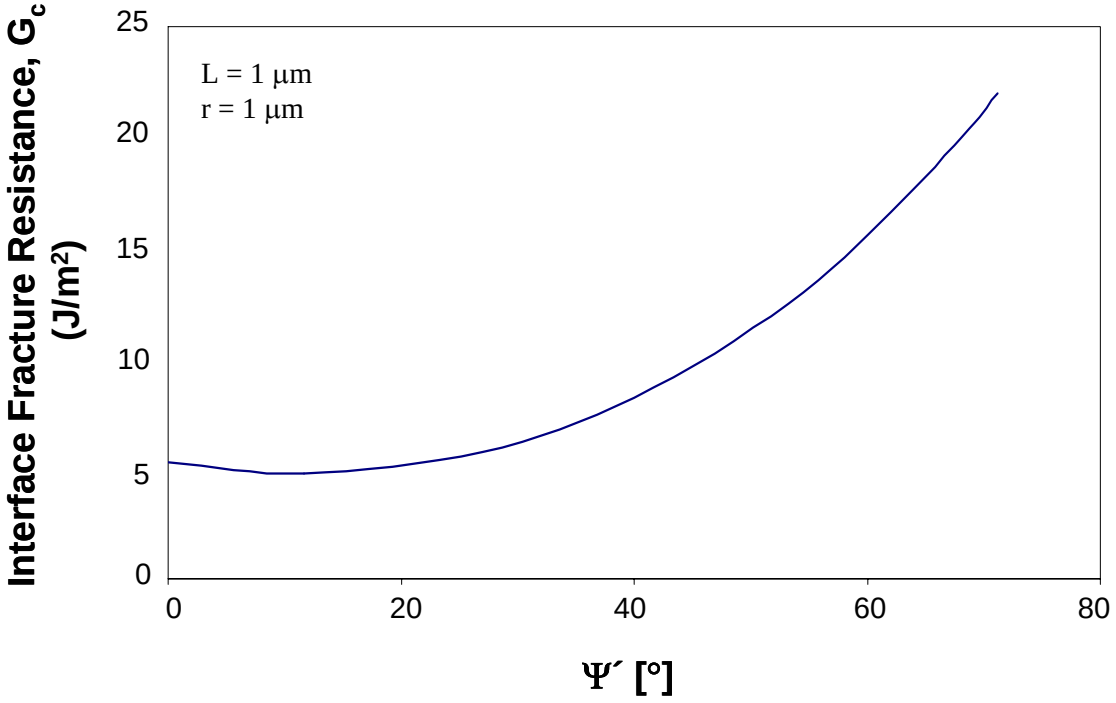

Figure 61: Fracture toughness curve for a bimaterial interface (glass/epoxy) [122]

O'Dowd et al. [121] and O'Dowd [123] discussed the effect of local mode mixity on the fracture energies of a niobium/alumina bimaterial specimens. They found the same behaviour as Wang[140] between the local phase angle and the stress intensity factors as shown in figure 62.

Shih & Asaro [124] showed that the local phase angle ψ' for the case of elastic plastic interface fracture can be computed via the following relation:

$$\psi' = \arctan\left(\frac{\sigma_{xy}}{\sigma_{xx}}\right) \tag{63}$$

where σ_{xy} denotes the shear stress at the crack tip along the crack front, while σ_{xx} is the normal opening stress at the crack tip at a distance of L = r along the crack propagation direction.

Using the relation of equation (63) the local phase angle ψ' has been computed for the case of a stationary crack tip and for growing cracks.

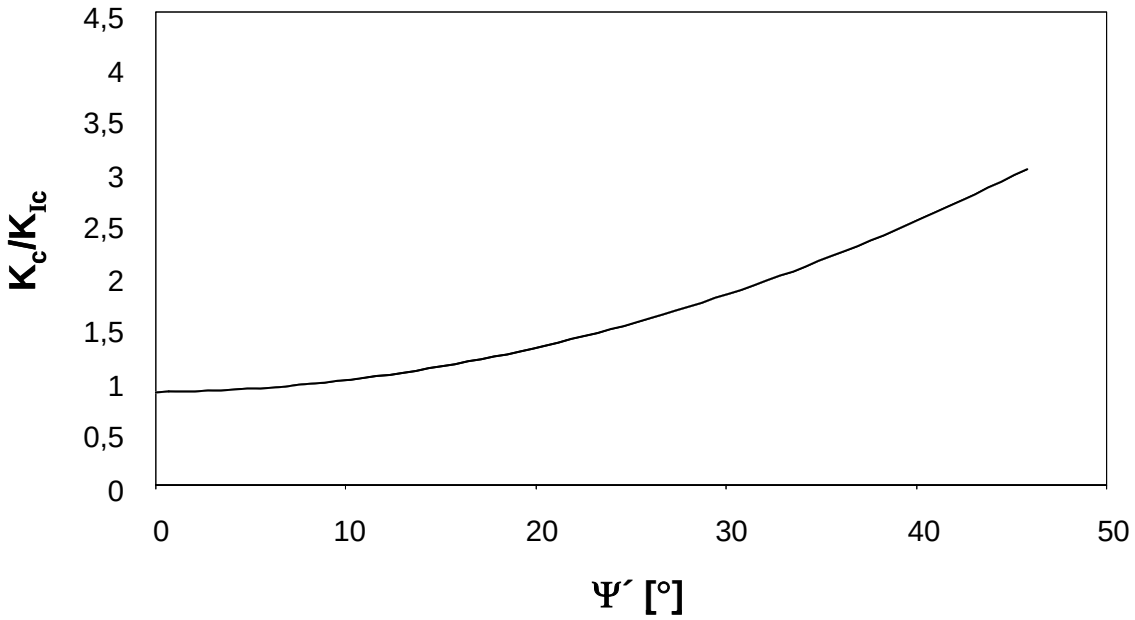

Figure 62: Fracture toughness curve for a bimaterial interface (niobium/alumina) [123]

The local phase angle ψ' for the case of a stationary crack tip in a bimaterial niobium/alumina system for three different orientations is given in table XVI. As the shear stress values along the interface at the stationary crack tip are small compared to the normal opening stress, the local phase angle ψ' is in the range of – 4.0° to – 0.3°. This range of local phase angles ψ' shows that the effect of local mode mixity is almost negligible. This can also be seen from figure 62 which shows for this range of local phase angles ψ' the K_c/K_{Ic} ratio is approximately equal to 1.

Table XVI: Local phase angle ψ' for various orientations of a stationary crack tip in niobium/alumina systems

Orientation	σ_{11} [MPa]	σ_{12} [MPa]	$\psi' = \tan^{-1}\left(\sigma_{12}/\sigma_{11}\right)$
Nb(100)[001]|Al_2O_3(11-20)[0001]	53.1	-4.08	-4.394°
Nb(110)[001]|Al_2O_3(11-20)[0001]	57.1	-5.278	-5.28°
Nb(111)[-1- 12]|Al_2O_3(11-20)[0001]	55.7	-3.07	-3.155°

Similarly, local phase angles ψ' have also been computed for growing cracks using a cohesive modelling approach. Two different cases have been considered. The first one is when both, the normal cohesive strength (σ_n) and the shear cohesive strength (σ_t) values are selected to be equal, i.e., $\sigma_n = \sigma_t$ (this has been the case for all the simulations performed in section 4.4.2). The normal cohesive strength (σ_n) is the maximum normal stress required for damage initiation and the shear cohesive strength (σ_t) is the maximum shear stress required for damage initiation. The second one is when the shear cohesive strength is selected as half of the normal cohesive strength, i.e., $\sigma_n = 2 \times \sigma_t$.

The local phase angle ψ' for the case when $\sigma_n = \sigma_t$ at different crack tip positions during crack growth is given in table XVII. All these results are for orientation II. The values of the local phase angle ψ' for the case of $\sigma_n = \sigma_t$ are found to be in the range of – 6.5° to – 4°.

Table XVII: Local phase angle ψ' for the case of a growing crack ($\sigma_n = \sigma_t$) for a Nb(110)-[001]|Al_2O_3(11-20)[0001] interface

Crack length (Δa), mm	σ_{11} [MPa]	σ_{12} [MPa]	$\psi' = \tan^{-1}\left(\sigma_{12}/\sigma_{11}\right)$
0.0	146.9	-11.23	-4.4°
0.00165	126.5	-14.46	-6.52°
0.00638	121.93	-11.6	-5.44°
0.0103	120.0	-12.3	-5.86°

The local phase angle ψ' for the case when $\sigma_n = 2 \times \sigma_t$ at different crack tip positions during crack growth is given in table XVIII. Again, the value of the local phase angle ψ' ranges in the narrow regime from –7.0° to – 4.7°.

Table XVIII: Local phase angle ψ' for the case of growing crack ($\sigma_n = 2 \times \sigma_t$) for a Nb(110)-[001]|$Al_2O_3$(11-20)[0001] interface

Crack length (Δa), mm	σ_{11} [MPa]	σ_{12} [MPa]	$\psi' = \tan^{-1}\left(\sigma_{12}/\sigma_{11}\right)$
0.0	146.0	-11.9	-4.66°
0.00165	125.64	-14.8	-6.71°
0.00638	119.68	-11.6	-5.54°
0.0103	118.9	-14.6	-7.0°

The results of the local phase angle ψ' for the case of a stationary crack tip and for growing cracks show that the effect of local mode mixity is almost negligible for the case of niobium/alumina bicrystal specimens.

4.4.2.4 Stress Triaxiality at the Crack Tip along the Interface

The locus of failure and the crack propagation behaviour are significant aspects in evaluating the mechanical properties of bonded joints. Dillard [125] showed that the crack path locus is closely related to material properties such as strength, interface quality and fracture toughness of the bonds along with the stress state at the crack tip.

Cao [126] and Akisanya [127] showed that the locus of failure and the crack propagation behaviour are dependent on the mode mixity of external loads.

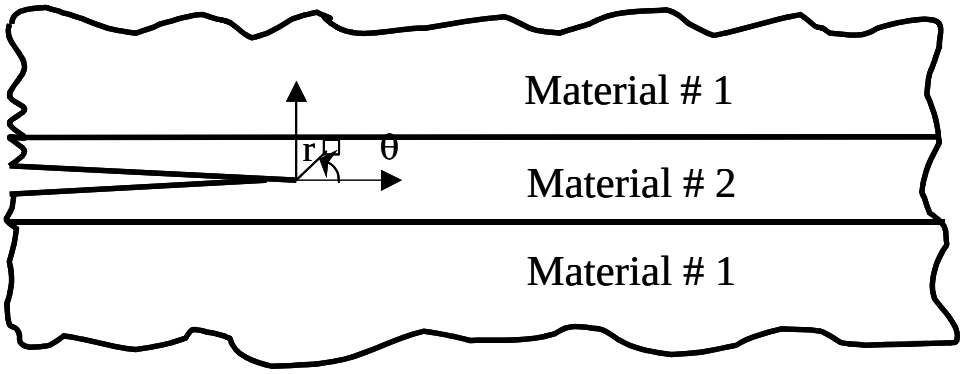

Figure 63: A crack in an adhesive bond, the model used by Fleck [128] and Akisanya [129]

Fleck [128] and Akisanya [127,129] investigated the directional stability issue in adhesive bonds. The geometry shown in figure 63, was assumed to be semi-infinite, the adhesive was assumed to be linear elastic, and a semi infinite straight crack was present within the adhesive layer. According to the coordinate system in figure 63, the stress state at the crack tip can be expressed in the asymptotic form [66] as:

$$\begin{bmatrix} \sigma_{xx} & \sigma_{xy} \\ \sigma_{xy} & \sigma_{yy} \end{bmatrix} = \frac{K_I}{\sqrt{2\pi r}} \cos\left(\frac{\theta}{2}\right) \begin{bmatrix} 1-\sin\left(\frac{\theta}{2}\right)\sin\left(\frac{3\theta}{2}\right) & \sin\left(\frac{\theta}{2}\right)\sin\left(\frac{3\theta}{2}\right) \\ \sin\left(\frac{\theta}{2}\right)\sin\left(\frac{3\theta}{2}\right) & 1+\sin\left(\frac{\theta}{2}\right)\sin\left(\frac{3\theta}{2}\right) \end{bmatrix}$$

$$+\frac{K_{II}}{\sqrt{2\pi r}} \begin{bmatrix} -\sin\left(\frac{\theta}{2}\right)\left[2+\cos\left(\frac{\theta}{2}\right)\cos\left(\frac{3\theta}{2}\right)\right] & \cos\left(\frac{\theta}{2}\right)\left[1-\sin\left(\frac{\theta}{2}\right)\sin\left(\frac{3\theta}{2}\right)\right] \\ \cos\left(\frac{\theta}{2}\right)\left[1-\sin\left(\frac{\theta}{2}\right)\sin\left(\frac{3\theta}{2}\right)\right] & \sin\left(\frac{\theta}{2}\right)\cos\left(\frac{\theta}{2}\right)\cos\left(\frac{3\theta}{2}\right) \end{bmatrix} \tag{64}$$

$$+\begin{bmatrix} T & 0 \\ 0 & 0 \end{bmatrix} + O\left(\sqrt{r}\right)$$

where r and θ are polar coordinates, and K_I and K_{II} are the stress intensity factors at the crack tip. The third term in equation (64) with stress $\sigma_{xx} = T$ is given as:

$$\sigma_{xx} = \frac{K_I}{\sqrt{2\pi r}}\cos\left(\frac{\theta}{2}\right)\left(1-\sin\left(\frac{\theta}{2}\right)\sin\left(\frac{3\theta}{2}\right)\right)+\frac{K_{II}}{\sqrt{2\pi r}}\left(-\sin\left(\frac{\theta}{2}\right)\left[2+\cos\left(\frac{\theta}{2}\right)\cos\left(\frac{3\theta}{2}\right)\right]\right)+T$$

where T is non-singular and acts in the direction parallel to the crack plane. By convention, this term is referred as the T-stress.

Rice [130] showed that the T-stress plays an important role in the directional stability of crack propagation. The crack is directionally stable if the T-stress is negative, whereas it is directionally unstable if the T-stress is positive. The reason for the directional instability is the positive T-stress, as the higher the positive T-stress is the higher will be the stress triaxiality, therefore, the crack will kink towards a direction where the T-stress becomes negative [125, 130] (a negative T-stress means compressive stress which does not allow the crack to kink while the positive T-stress means tensile stress which makes a crack to kink away from a direction where the T-stress is compressive). Rice [130] showed this crack kinking behaviour analytically (see [130] for details), it was shown that the crack kinks towards a direction where the T-stress becomes negative which is also the same direction where $K_{II} = 0$ [130]. Fleck [128] and Akisanya [127, 129] also concluded that under predominantly mode I loading, the crack propagation in an adhesive bond is directionally stable if the T-stress is negative and is directionally unstable if the T-stress is positive.

This criterion, although developed primarily for cracks in homogeneous materials, can be readily extended to interfaces in bimaterial systems such as bonded joints according to Hutchinson [105].

The study of Zhu and Chao [131] provides further insights about the effect of the T-stress on the crack propagation behaviour in homogeneous media. Not only the directional stability of cracks, but also the direction of crack propagation will be affected by the T-stress. Zhu and Chao [131] clarified that although the criteria for the cracking direction and directional stability of cracks are developed under the assumptions of linear elastic fracture mechanics, they are still applicable for ductile materials in most cases.

According to equation (64), the T-stress can be calculated by substituting the stress σ_{xx}, σ_{yy} and the stress intensity factors obtained from finite element analyses into equation (64).

When the fracture arises under pure mode I, i.e., $K_{II} = 0$ in equation (64), then the T-stress along the crack plane ($\theta = 0$ and $\pm\pi$) can be obtained from equation (64) as:

$$T = \sigma_{xx} - \sigma_{yy} \tag{65}$$

if the fracture is in mixed mode, i.e., $K_{II} \neq 0$. Then, the T-stress behind the crack tip ($\theta = \pm\pi$) [125] is obtained by substituting $\theta = \pm\pi$ in equation (64) and is given by:

$$T = \sigma_{xx} + K_{II}\sqrt{\frac{2}{\pi r}} \tag{66}$$

where σ_{xx} is obtained from the finite element analysis, and K_{II} can be obtained from the finite element analysis, as:

$$K_{II} = \left(\sigma_{xy}\sqrt{2\pi r}\right)_{\theta=0} \tag{67}$$

The relations for T-stress discussed above are used to compute the T-stress values at various crack tip positions during crack growth for two different combinations of normal cohesive strength and shear cohesive strength, i.e., when $\sigma_n = \sigma_t$ and $\sigma_n = 2 \times \sigma_t$.

The computed values of T-stress for various crack lengths is given in table XIX for $\sigma_n = \sigma_t$ and in table XX for the case when $\sigma_n = 2 \times \sigma_t$.

Table XIX: T-stress at various positions of the crack tip during crack growth ($\sigma_n = \sigma_t$)

Crack length (Δa), mm	σ_{xx} [MPa]	σ_{yy} [MPa]	T-stress [MPa]
0.0	82.03	146.9	-64.87
0.00165	89.4	126.5	-37.1
0.00638	66.36	121.93	-55.57
0.0103	63.67	120.0	-56.33

Table XX: T-stress at moving crack tip during different stages of crack growth ($\sigma_n = 2 \times \sigma_t$)

Crack length (Δa), mm	σ_{xx} [MPa]	σ_{yy} [MPa]	T-stress [MPa]
0.0	82.32	146.0	-63.68
0.00165	87.43	125.64	-38.21
0.00638	61.19	119.68	-58.49
0.0103	57.46	118.9	-61.44

The results shown in table XIX and XX demonstrate that the T-stress is always found to be negative, therefore, the crack propagation direction is always stable according to the above criteria, i.e., along the interface during all the simulations.

4.4.2.5 Influence of Strain Gradient Crystal Plasticity

Steep strain gradients in the vicinity of the crack tip produce locally high levels of strain hardening due to a high density of geometrically necessary dislocations which ultimately end up with higher levels of stresses around the crack tip. The effect has been observed at the micron scale in indentation tests, in torsion of wires, bending of thin films [134] and metal/ceramic interfaces [140]. In some cases (see [134] and [140]), stress levels from strain gradient theories have been observed to be two to three times the stresses in the absence of strain gradients. Such high stress levels from strain gradient effects are expected to have a profound influence on interface separation. For the cases when the length of the separation zone is less than a micron, the separation zone will be surrounded by plastically deformed material which has undergone gradient hardening. In this section the stress elevations due to strain gradient effects are explored using mechanism based strain gradient (MSG) crystal plasticity theory [132, 133].

The mechanism based strain gradient theory (MSG) which is being used here is developed in [132, 133]. It is a generalization of conventional crystal plasticity theory [55 - 57]. The mechanism based strain gradient crystal plasticity theory reduces to conventional crystal plasticity theory when strain gradients vanish or when the scale of the nonuniform deformation is larger than the intrinsic length scale *l*. This will be shown in the following.

The intrinsic length scale of a material which is a function of an empirical constant α in the order of 0.3 - 0.5, shear modulus μ, the magnitude of the Burgers vector *b* as well as the reference slip resistance g_0, and is given by [132, 133]:

$$l = \frac{\alpha^2 \mu^2 b}{(g_0)^2} \tag{68}$$

where α is an empirical coefficient ranging from 0.3 – 0.5, μ is the shear modulus, *b* the magnitude of the Burgers vector while g_0 denotes a reference slip resistance which is taken to be $\mu/100$ [132].

In mechanism based strain gradient crystal plasticity theory [132, 133], the effective slip resistance is the resultant of the slip resistance due to strain hardening which is caused by statistically stored dislocations g_S^α for slip system α and the slip resistance due to the effective density of geometrically necessary dislocations η_G^α:

$$g_T^\alpha = \sqrt{\left(g_S^\alpha\right)^2 + (g_G^\alpha)^2} \tag{69}$$

The slip resistance due to strain hardening which is caused by statistically stored dislocations g_S^α is computed using equation (9), given as:

$$\dot{g}^{(\alpha)} = \sum_\beta h_{\alpha\beta}\dot{\gamma}^{(\beta)}$$

The intrinsic length scale l enters into the effective slip resistance g_T^α through the slip resistance contribution by the effective density of geometrically necessary dislocations η_G^α.

The slip resistance due to the effective density of geometrically necessary dislocations g_G^α is given by

$$g_G^\alpha = \sqrt{l\eta_G^\alpha} \tag{70}$$

while the effective density of geometrically necessary dislocations is given by

$$\eta_G^\alpha = \left| \underline{m}^\alpha \times \sum_\beta s^{\alpha\beta} \nabla\gamma^\beta \times \underline{m}^\beta \right| \tag{71}$$

where $\underline{m}^\alpha$ is the slip plane normal while $s^{\alpha\beta} = \underline{s}^\alpha \cdot \underline{s}^\beta$ with $\underline{s}^\alpha$ being the slip direction.

The modified effective slip resistance is, therefore, given by

$$g_T^\alpha = \sqrt{\left(g_S^\alpha\right)^2 + l\eta_G^\alpha} \tag{72}$$

Using the above equation of effective slip resistance, the plastic slip rate in equation (8) is then modified to

$$\dot{\gamma}^\alpha = \dot{\gamma}_o^\alpha \,\mathrm{sgn}(\tau^{(\alpha)}) \left\{ \left| \frac{\tau^{(\alpha)}}{g_T^{(\alpha)}} \right| \right\}^m \tag{73}$$

In the following, the above discussed relations for mechanism based strain gradient crystal plasticity theory have been used to study the strain gradient effect on the stresses around the crack tip along with the J-integral values.

The UMAT subroutine (MSGMAT) consisting of conventional crystal plasticity theory [86] has been modified and above discussed relations of mechanism based crystal plasticity theory (equation (67) – (72)) have been implemented in the UMAT subroutine in order to study the effect of strain gradient theory on the stresses around the crack tip and fracture energies.

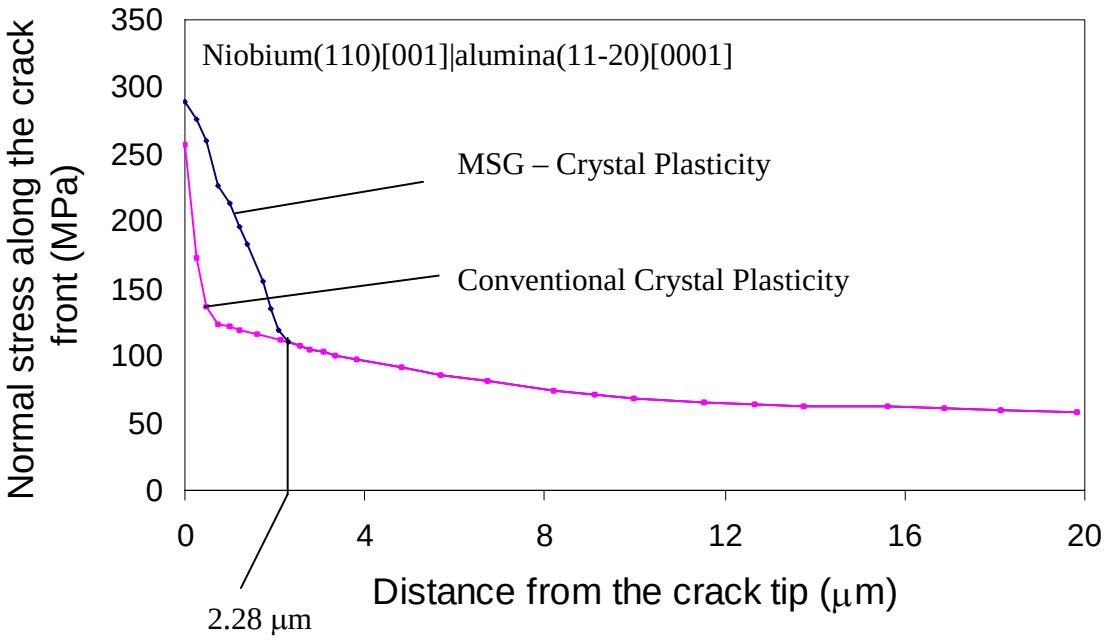

Figure 64: Normal stress distribution along the crack front for the case of conventional crystal plasticity and msg - crystal plasticity

The finite element model used for this study is the same as explained in section 4.4.1. The value of the intrinsic material length for single crystalline niobium (with b = 0.25 nm, $\alpha = 0.5$, and g_0 = 1.725 GPa) is found to be, l = 0.625 μm. All the simulations have been performed for the niobium (110)[001]|alumina (11-20)[0001] interface based on the fact that the intrinsic material length is almost the same for all orientations and the size of the plastic zone is always in the range of 30 – 61 μm.

The distribution of normal stress along the bicrystal niobium/alumina interface ahead of the crack tip is plotted in figure 64. The plot shows the results of both, conventional crystal plasticity and mechanism based strain gradient crystal plasticity theory.

Both, conventional crystal plasticity theory and the here implemented mechanism based strain gradient crystal plasticity theory give the same stress distribution at a distance of greater than 2.28 μm from the crack tip. For the distance less than 2.28 μm from the crack tip, mechanism based strain gradient crystal plasticity theory gives higher normal stress than conventional crystal plasticity theory: This is due to the strain gradient effect at the metal/ceramic interface. If we compare the ratio of the normal stress at the crack tip to the yield stress of single crystalline niobium (σ/σ_y) then for conventional crystal plasticity theory this ratio is 5.0953 while for mechanism based strain gradient crystal plasticity theory this ratio is increased to 5.7075 (with σ_y = 50.63 MPa for niobium (110)[001]).

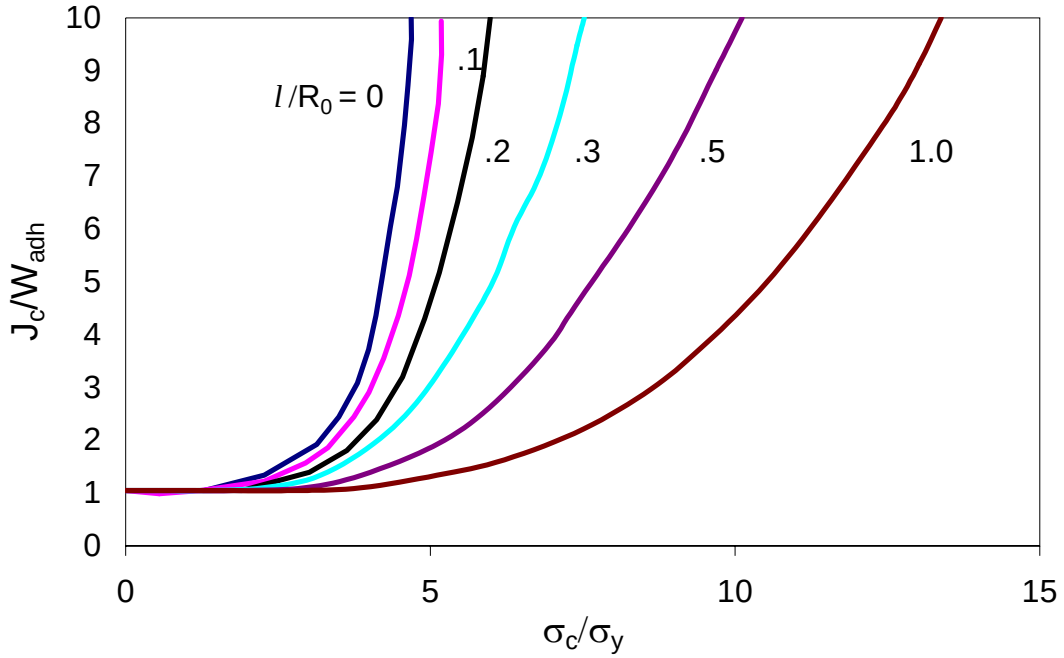

Figure 65: The influence of strain gradient plasticity on (J_c/W_{adh}) [134] (for details see text)

This suggests that a strain gradient does increase the normal stress near the crack tip significantly, and the difference in stress apart from the crack tip and below 2.28 μm is of the factor greater than 1.5. This difference (factor of >1.5) in stress can be explained on the basis of results obtained in [134] where the effect of J_2 strain gradient plasticity theory on the fracture energy of the bimaterial interface is discussed. The effect of intrinsic material length (l) on the fracture energy (J_c) and cohesive strength (σ_c) of the bimaterial interface is also studied in [134]. It is shown that as the intrinsic material length (l) increases, the cohesive strength required to reach a specific fracture energy (J_c) value also increases.

In figure 65 [134] the ratio of fracture energy to work of adhesion (J_c/W_{adh}) is shown as a function of cohesive strength to yield stress ratio (σ_c/σ_y) for various values of l/R_0 for a homogeneous material, where R_0 is the size of the plastic zone. It can be seen that at a given (J_c/W_{adh}) value, (σ_c/σ_y) increases as l/R_0 increases and that at a given σ_c/σ_y ratio J_c/W_{adh} increases as l/R_0 decreases. These results show that l/R_0 has a strong influence on the level of stress that will be achieved around the crack tip due to strain gradient effects, i.e., the larger the l/R_0 value the higher will be the stresses around the crack tip. More importantly: for a given J_c/W_{adh} ratio and a given l value the size of the plastic zone increases with increasing σ_c/σ_y ratio. This means that for a given material with intrinsic material length (l) the l/R_0 ratio will depend on the size of the plastic zone (R_0), which means that the smaller the plastic zone size the lower will be the plastic dissipation. This lower plastic dissipation means that such an

interface is relatively more brittle, which ultimately requires higher stresses to achieve a given (J_c/W_{adh}) value.

If we now look into the current niobium/alumina bicrystal interface the value of intrinsic material length is l = 0.625 μm as computed above. Also, the size of the plastic zone is always found to be in the range of 30 – 61 μm (figure 43). This gives a value of l/R_0 = 0.01 - 0.021 in which the region where (σ_c/σ_y) is less sensitive to the l/R_0 value due to the reason that the scale of plastic deformation is larger than the intrinsic material length l. Therefore, mechanism based strain gradient crystal plasticity theory has only a small influence on the (σ_c/σ_y) ratio for all interfaces analyzed in the case of niobium/alumina bicrystals.

The fracture energies computed for the case of mechanism based strain gradient crystal plasticity theory and conventional crystal plasticity theory were found to be identical in case of stationary cracks, as shown in figure 66. This is due to the small region (0.1 – 2 μm) where stresses were found to be higher for the case of mechanism based strain gradient crystal plasticity theory.

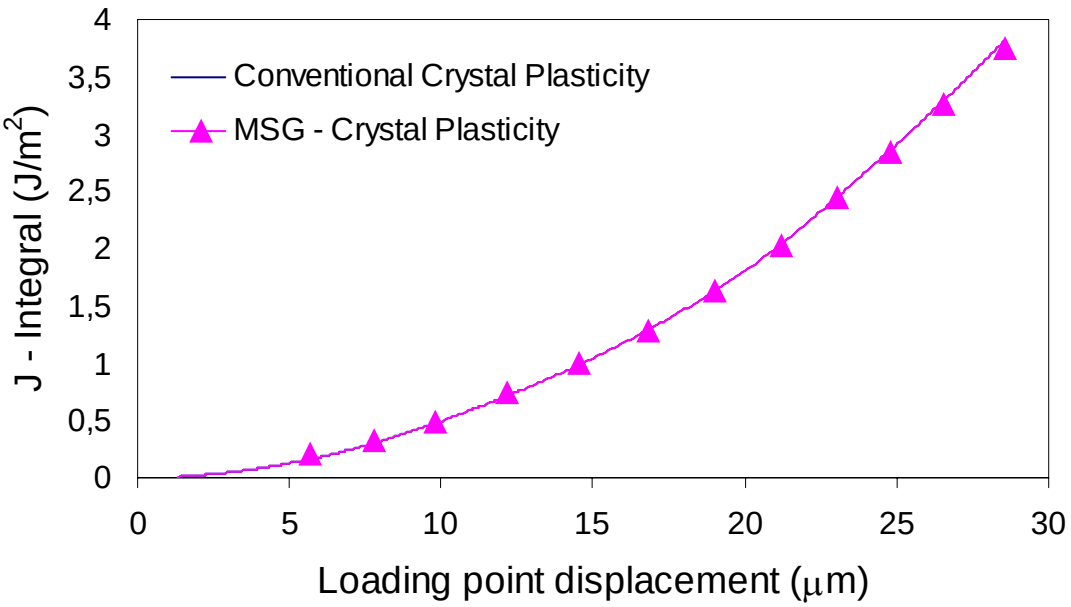

Figure 66: J–integral vs. loading point displacement for conventional crystal plasticity and MSG-crystal plasticity theory for a stationary crack of a Nb(110)[001]|Al_2O_3(11-20)[0001] interface

4.4.3 Correlation between Local Adhesion Capacity and Macroscopic Fracture Energy

In section 4.4.2 the influence on the fracture energies of different cohesive model parameters, such as, cohesive strength and work of adhesion on the fracture energy was presented. This section is devoted to find a correlation between the local adhesion capacity and macroscopic

fracture energy for three different orientations of niobium single crystals in niobium/alumina bicrystal specimens. The correlation found for the three different orientations can be extended to other orientations, if experimental data, such as stress-strain-curves and fracture energies are available for other orientations.

Different experimental investigators have put ample effort to correlate the local adhesion capacity and macroscopic fracture energy for different metal/ceramic interfaces. For example, a gold/alumina interface was studied experimentally in [135]. They found out that crack extension occurs by a combination of plastic void growth and interface debonding. It was also shown that the fracture energies are much larger than the work of adhesion and the fracture energy is dominated by plastic dissipation, which increases as the metal layer thickness increases. Different metal layer thicknesses ranging from 10 - 100 μm were investigated. The correlation was derived for initiation fracture energy as a function of work of adhesion, yield stress and thickness of metal layer as shown in figure 67. The relation between J_c and W_{adh} for gold/alumina interfaces is given in equation (73):

$$J_c = W_{adh}\left[1+\frac{\sigma_0 h}{W_{adh}}\right]^{1/2} \tag{74}$$

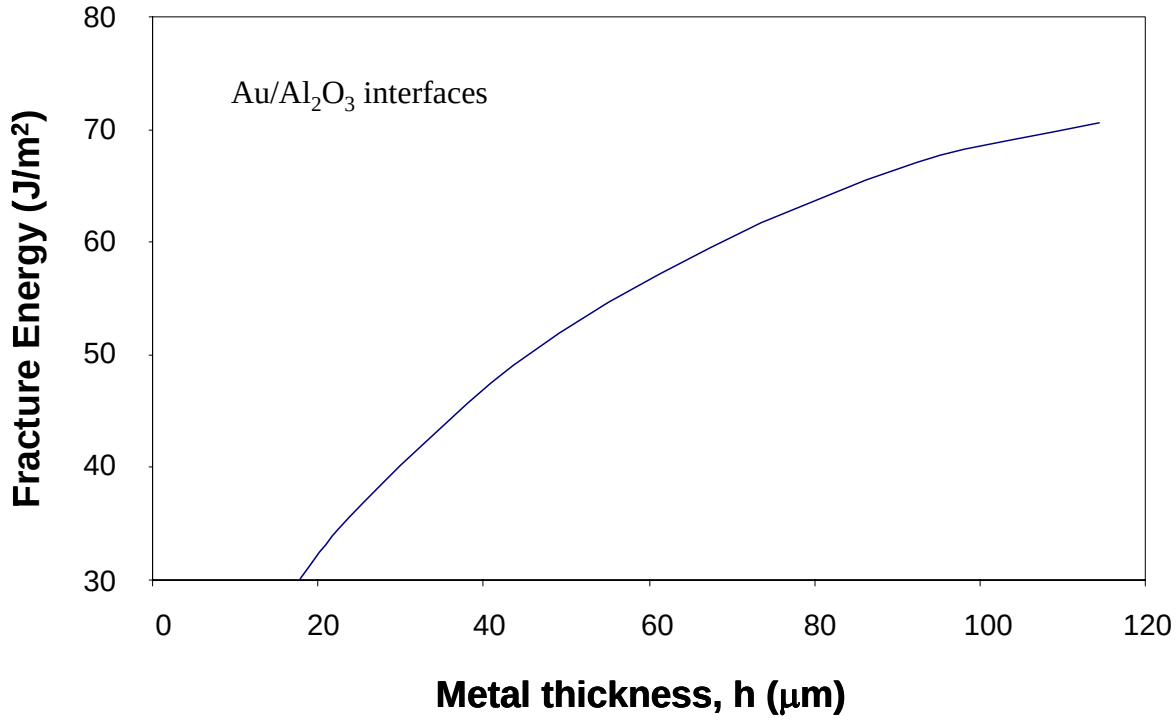

Figure 67: Fracture energy as function of metal layer thickness [135] for Au|Al_2O_3 interfaces

A correlation between work of adhesion and fracture energy for niobium/alumina interfaces was derived in [136]. For the derivation the value of work of adhesion value for a pure

niobium/alumina interface was assumed to be 800 mJ/m^2. The work of adhesion was varied from 0 to 800 mJ/m^2 by doping silver at the interface. It was found that the interface fracture energy increases linearly up to a critical value of the work of adhesion W_{adh}^{crit}. Above this value a strong exponential increase in fracture energy occurs which is due to extensive plastic deformation of the metal regions adjacent to the crack. The relation was derived for the above discussed two regions, i.e., linear and exponential regions and is given below:

$$\begin{aligned} J_c &= a \cdot W_{adh} && \text{for } W_{adh} < W_{adh}^{crit} \\ J_c &= a \cdot W_{adh} + \left(W_{adh} - W_{adh}^{crit}\right) && \text{for } W_{adh} > W_{adh}^{crit} \end{aligned} \tag{75}$$

As compared to the above discussed relations where the fracture energy was defined as a function of work of adhesion and yield stresses, this section describes the correlation among cohesive strength, work of adhesion, yield stress and fracture energy as given below:

$$J_c = f\left(\frac{\sigma_c}{\sigma_y}, W_{adh}\right) \tag{76}$$

The influence of cohesive strength (σ_c) to yield stress (σ_y) on fracture energy for three different values of work of adhesion (W_{adh}) was plotted in figure 52 for the niobium(110)[001]|alumina(11-20)[0001] interface. The plot shows that a cubic relation exists between the cohesive strength (σ_c) to yield stress (σ_y) ratio and the fracture energy. In the same manner the influence of work of adhesion (W_{adh}) on fracture energy was plotted in figure 53, which showed a linear relation between work of adhesion (W_{adh}) and fracture energy (J_c).

Based on the above conclusions the following relation has been used to described the correlation between the local adhesion capacity and the macroscopic fracture energy:

$$J_c = \left(a\left(\frac{\sigma_c}{\sigma_y}\right)^3 + b\left(\frac{\sigma_c}{\sigma_y}\right)^2 + c\left(\frac{\sigma_c}{\sigma_y}\right) + d\right) W_{adh} \tag{77}$$

In order to identify the coefficients *a*, *b*, *c*, and *d* in equation (76) a surface has been plotted using fracture energies (J_c), work of adhesion (W_{adh}) and cohesive strength (σ_c) to yield stress (σ_y) ratio, as shown in figure 68.

The coefficients *a*, *b*, *c*, and *d* in equation (76) are identified by least square surface fitting technique with MATLAB [141]. The identified coefficients are given in table XXI.

Table XXI: Coefficients in equation (76) identified for the niobium(110)[001]|alumina(11-20)[0001] interface

a	*b*	*c*	*d*
13.04076	-127.85	412.5	-417.074

Similarly, fracture energies (J_c), the work of adhesion (W_{adh}) and cohesive strength (σ_c) to yield stress (σ_y) ratio for niobium(100)[001]|alumina(11-20)[0001] interface has been plotted in figure 69. Using the same least square surface fitting technique the parameters *a*, *b*, *c*, and *d* in equation (76) are identified and are given in table XXII.

Table XXII: Coefficients in equation (76) identified for the niobium(100)[001]|alumina(11-20)[0001] interface

a	*b*	*c*	*d*
2.983804	-34.801	135.24	-164.89

Using the same approach the parameters *a*, *b*, *c*, and *d* in equation (76) are identified and are given in table XXIII while fracture energies (J_c), work of adhesion (W_{adh}) and cohesive strength (σ_c) to yield stress (σ_y) ratio for the niobium(111)[-1-12]|alumina(11-20)[0001] interface has been plotted in figure 70.

Table XXIII: Coefficients in equation (76) identified for the niobium(111)[-1-12)|alumina(11-20)[0001] interface

a	*b*	*c*	*d*
2.431	-32.523	136.0034	-164.7

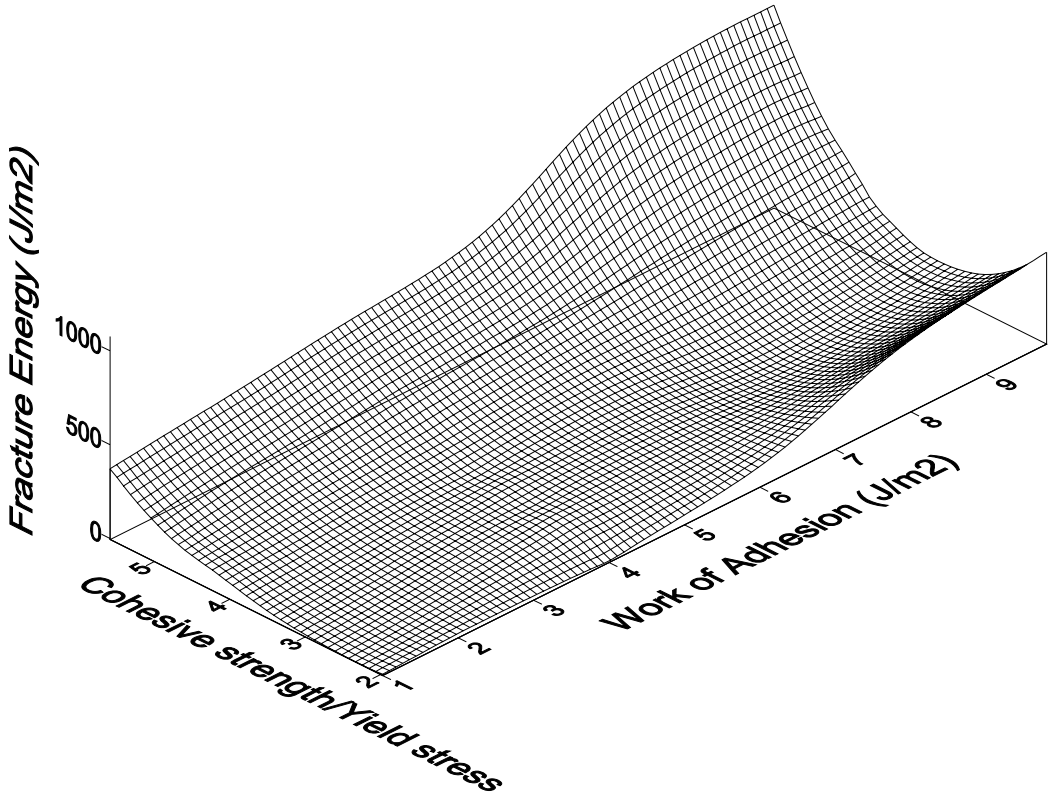

Figure 68: Surface plot of fracture energy vs. work of adhesion and cohesive strength for the niobium(110)[001]|alumina(11-20)[0001] interface

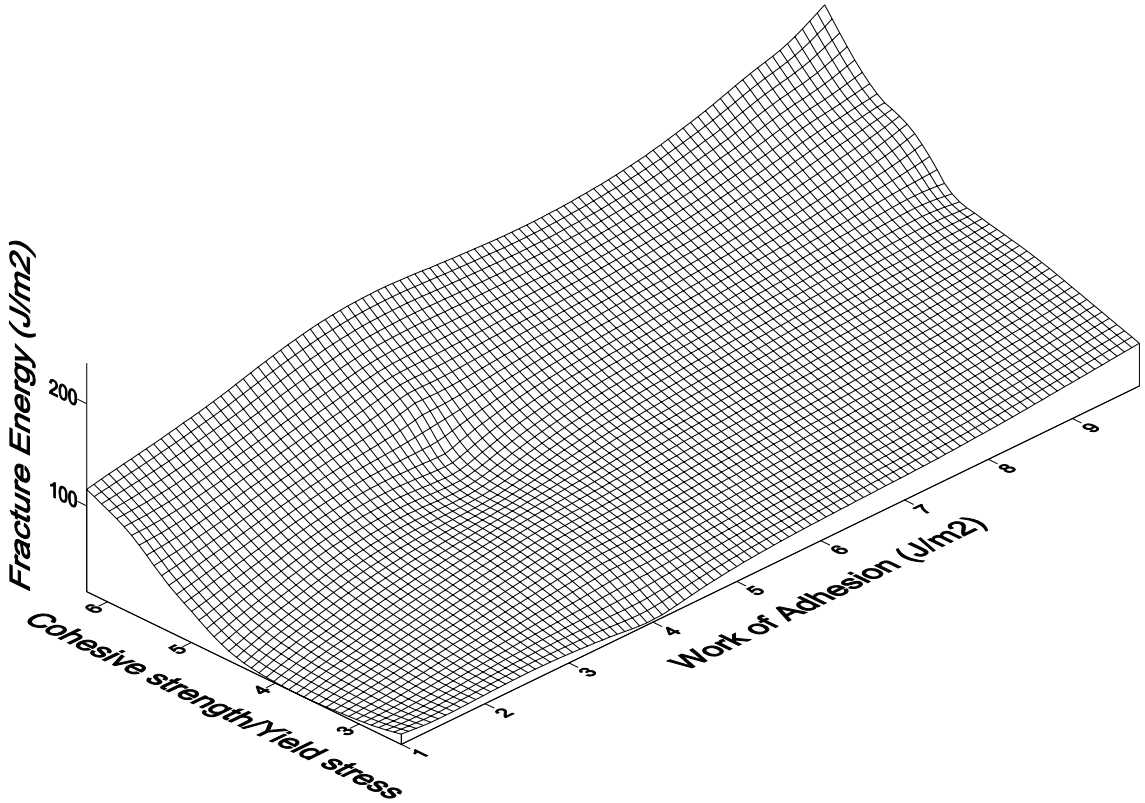

Figure 69: Surface plot of fracture energy vs. work of adhesion and cohesive strength for the niobium(100)[001]|alumina(11-20)[0001] interface

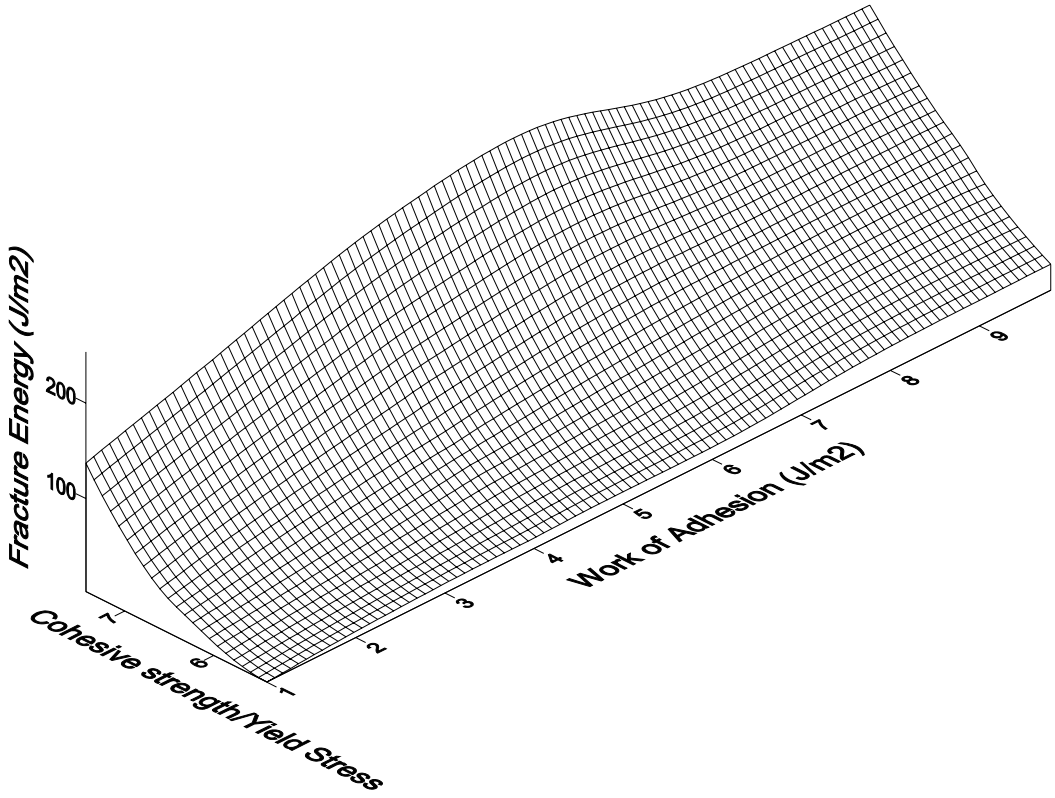

Figure 70: Surface plot of fracture energy vs. work of adhesion and cohesive strength for the niobium(111)[-1-12]|alumina(11-20)[0001] interface

In order to generalize the results obtained for the above discussed three orientations of niobium/alumina bicrystal specimens, a generalized relation has been deduced which can be used for any of the above three orientations of niobium/alumina bicrystal specimens. This has been done by introducing an additional parameter α_i which depends on the orientation of the bicrystal specimens. The generalized relation is given by:

$$J_c = \left(2.98\left(\alpha_i \cdot \frac{\sigma_c}{\sigma_y} \right)^3 - 34.8\left(\alpha_i \cdot \frac{\sigma_c}{\sigma_y} \right)^2 + 135.24\left(\alpha_i \cdot \frac{\sigma_c}{\sigma_y} \right) - 164.89 \right) W_{adh} \qquad (78)$$

Using the same least square surface fitting technique available in MATLAB [141], the orientation coefficients α_i have been identified for the three different orientations of niobium/alumina bicrystal interfaces which are given in table XXIV for three different orientations of niobium/alumina bicrystal interfaces.

A generalized correlation among cohesive strength, work of adhesion, yield stress and fracture energy for the three different orientations is thus deduced in this section with orientation parameters $\alpha_i \cong 0.8 - 1.35$ for the orientations studied. In the above correlation the cohesive strength (σ_c) can be estimated using the correlation derived in section 4.4.2.1 and is given by:

$$\sigma_c = 6.112\left(\alpha_i \cdot \frac{W_{adh}}{W_0}\right)^{-0,0919} \cdot \sigma_y \qquad (79)$$

Table XXIV: Orientation parameter (α_i) for three orientations of bicrystal niobium/alumina interfaces

Orientation	Orientation parameter α_i
Nb(100)[001]|Al_2O_3(11-20)[0001]	1.0
Nb(110)[001]|Al_2O_3(11-20)[0001]	1.35
Nb(111)[-1-12]|Al_2O_3(11-20)[0001]	0.853

The relation found in equation (78) can be used to predict the fracture energy of single crystalline niobium/alumina bimaterial systems, if the rest of the material parameters are available. The relation not only takes into account the dependence of the fracture energy on cohesive model parameters, such as, cohesive strength and work of adhesion, but also material properties, such as the yield stress which is strongly dependent on the crystal orientation [137, 138].

4.4.4 Summary

Interface fracture analyses of bicrystal niobium/alumina specimens were presented in this section using a cohesive modelling approach. In the first part, the influence of cohesive law parameters, such as, cohesive strength and work of adhesion were studied for different orientations of niobium single crystalline materials in the niobium/alumina bicystal specimens.

It was shown that cohesive strength has a strong influence on the fracture energy of the bicystal niobium/alumina interface for the different niobium orientations studied. It was found that as the cohesive strength increases the fracture energy also increases. This is due to the higher plastic energy dissipation. The relation between the cohesive strength and the fracture energy is found to be non-linear cubic.

It was also shown that the work of adhesion has also influence on the fracture energy, i.e., as the work of adhesion increases the fracture energy also increases. The relation for various orientations of niobium single crystalline material in the niobium/alumina bicrystal specimens is found to be almost linear.

Stresses along the crack front ahead of the crack tip were also analyzed for the cases of a stationary crack tip and for growing cracks. It is found that the shear stress contribution is almost negligible as compared to the normal stresses ahead of the crack tip.

Based on the stresses ahead of the crack tip the local mode mixity was studied by computing the local phase angle and it was found that for short cracks the local phase angle is always in the range of -7° to -4°, which - when plotted on the fracture toughness curve of niobium/alumina curve - shows that the influence of local mode mixity for the case of niobium/alumina bicrystal specimens is almost negligible.

Local mode mixity was found to not play any significant role in the case of niobium/alumina bicrystal specimens. The effect of stress triaxiality was also studied to find the directional stability of the growing cracks. T-stresses were computed and are always found to be negative in the range of –65 to –35 MPa resulting in a directionally stable crack growth, namely along the interface of niobium/alumina bicrystal specimens because of low stress triaxiality at the interface crack tip of the niobium/alumina bicrystal interface. The physical reason as explained in section 4.4.2.4 is negative T-stress means compressive stress acting parallel to the interface causing the crack to propagate in the direction along the interface while a positive T-stress means tensile stresses acting parallel to the interface causing an interface crack to kink into the direction where the stress parallel to the crack face becomes compressive.

The influence of strain gradient crystal plasticity theory was also studied using a mechanism based crystal plasticity theory. It was found that due to the strain gradient in the vicinity of the crack tip, i.e., in the range of 0.1 – 2 μm the stresses for the case of mechanism based strain gradient crystal plasticity theory were always found to be higher than the conventional crystal plasticity theory. It was also found that the difference in the stresses from both theories is not large. Also the overall fracture energies computed from the mechanism based strain gradient crystal plasticity theory and conventional crystal plasticity theory were found to be identical except for a very small region at the crack tip where normal stresses are significantly higher for the case of mechanism based crystal plasticity theory. The shear stress distribution along the crack front was found to be negligible as compared to the normal stress. This was also the case for the stresses obtained from conventional crystal plasticity theory.

In the last part of this section a generalized correlation was derived among the fracture energy, cohesive strength, work of adhesion and yield stress. Orientation parameters for this correlation were identified for three different orientations of niobium single crystalline materials in the bicrystal niobium/alumina specimens.

5. Summary and Conclusion

This work is focused on the study of crystal plasticity effects in the fracture of metal/ceramic interfaces for the system Nb/Al_2O_3. A procedure has been described to realistically simulate the fracture behaviour of the Nb/Al_2O_3 system. Crystal plasticity theory [45] has been used to take into account crystal orientation effects on the plastic deformation and ultimately on the fracture energy of the Nb/Al_2O_3 system. The crack propagation analysis has been performed with a cohesive modelling approach using a cohesive model [84, 85]. The ultimate goal of the investigation is to theoretically clearing-up the connection between local adhesion capacity and macroscopic fracture energy.

The niobium single crystalline material is always modelled as body-centered-cubic crystals using crystal plasticity theory. The three stage hardening of niobium single crystalline material during deformation has been modelled using the Bassani & Wu (BW) model. For the case of body-centered-cubic crystals the parameters which are to be identified for the Bassani & Wu (BW) model are twenty, i.e., ten parameters for each family of slip systems. Therefore, an automatic identification procedures has been applied to identify these parameters by creating an interface between an optimisation tool and ABAQUS. This procedure automatically identifies the hardening parameters for each family of slip systems.

Different techniques, such as the global energy method, the virtual crack closure technique and the J-integral method have been presented to compute the fracture energy of the bicrystal specimens both for two and three dimensional structures. The fracture energies computed using the above three methods have been compared which showed the consistency in the results.

Four-point-bending-testing of the bicrystal specimens has also been simulated using crystal plasticity theory for the niobium single crystalline material. All the simulations are done for a stationary crack tip. The results obtained from these simulations are compared with the experimental results which show that there is a variation in fracture energy for different orientations as was measured in experiments. This is due to the plastic anisotropy of the single crystalline niobium material which cannot be captured by the continuum deformation plasticity theory because continuum deformation plasticity theory can only be used for isotropic materials. The difference in the fracture energies has been explained based on the contribution of the plastic slip (strain) of each activated slip system for various orientations. The finite element analyses results using crystal plasticity theory for the case of a stationary

crack tip show the same trend of computed fracture energy as was found in the experiments [22, 23].

The effect of thermal residual stress induced in the bicrystal specimens during diffusion bonding when a specimens is cooled down from the bonding temperature of 1400 °C, has been studied. As the mismatch in the thermal expansion coefficients is very small, therefore, it is found that the induced thermal residual stresses are small. Therefore, no significant effect on the fracture energies was found for the niobium/alumina system.

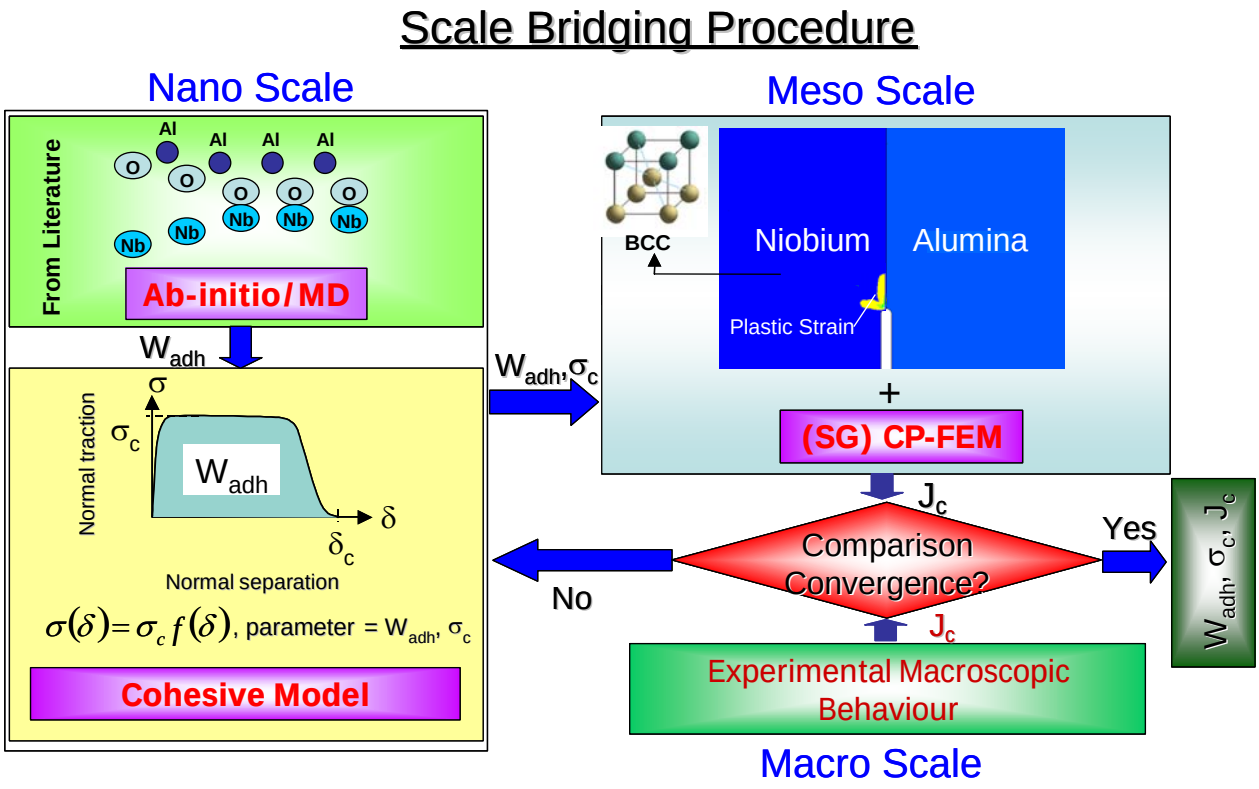

Figure 71: Scale bridging procedure for metal/ceramic interface fracture

The interface fracture of the bicrystal Nb/Al_2O_3 system is studied using a cohesive modelling approach. Parameter studies were performed in order to study the effect of different cohesive law parameters, such as, cohesive strength and work of adhesion on fracture energies and crack growth resistance. It has been found that the effect of cohesive strength on fracture energies is non-linear and more profound as compared to the work of adhesion. It was found that as the cohesive strength increases the fracture energy also increases due to the higher plastic dissipation. In addition, the fracture energies depend linearly on the work of adhesion for various orientations of the niobium single crystalline material in the niobium/alumina bicrystal specimens. Cohesive model parameters are identified for different combinations of cohesive strength and work of adhesion by applying a scale bridging procedure as shown in figure 71. For each value of work of adhesion [26, 27, 28, 42, 119, 120] (experimental

estimate 1 J/m^2 [42, 119], ab-initio [26, 27, 28] 9.8 J/m^2, and molecular dynamics [120] 4 J/m^2), the cohesive strength (σ_c) is varied and transferred to the bicrystal niobium/alumina finite element model as input parameters for the cohesive law to simulate the interface fracture. Niobium single crystals are modelled using crystal plasticity theory in bicrystal niobium/alumina interfaces. The result of the simulation, i.e. the computed fracture energy of the system is compared with the experimental fracture energy value. When convergence is reached then the final set of local interface fracture parameters (σ_c, W_{adh}) and global fracture energy (J_c) of the system is obtained, otherwise the simulation is rerun with the new guess of cohesive strength (σ_c). The new guess of cohesive strength (σ_c) is based on the comparison of global fracture energy (J_c) obtained from the simulation and the experimental fracture energy. If the simulated global fracture energy (J_c) is lower than the experimental fracture energy then the value of cohesive strength (σ_c) is increased otherwise decreased. The amount of the $\Delta\sigma_c$ value selected depends on the difference between simulated and experimental fracture energies and was chosed in the range of 1 - 40 MPa. The procedure has been repeated for each value of work of adhesion (W_{adh}).

Stresses along the crack front ahead of the crack tip and local mode mixity are also analysed for the cases of stationary crack tips and for growing cracks. It is found that the shear stress contribution is almost negligible as compared to the normal stresses at the crack tip because the mismatch in the elastic properties of niobium and alumina is small with elastic mismatch parameter $|\varepsilon| < 0.06$ [23]. The elastic mismatch parameter ε is defined in [144]. It is computed using the elastic properties of the two materials and its magnitude describes how high is the elastic mismatch. Based on the stresses ahead of the crack tip the local mode mixity according to the applied tensile stresses is computed and it was found to be in the range of -7° to -4°. This shows that local mode mixity does not play any significant role for the case of niobium/alumina bicrystal specimens because the local mode mixity angle is less than 10° (as shown in figure 62 for local mode mixity value less than 10° the overall stress intensity factor is mode I dominated).

The effect of stress triaxiality was also studied to find the directional stability of the growing cracks. T-stresses were computed and are always found to be negative in the range of –65 to –35 MPa resulting in a directionally stable crack growth, namely along the interface of niobium/alumina bicrystal specimens because of a low stress triaxiality at the interface crack tip of niobium/alumina bicrystal interfaces.

The influence of strain gradient crystal plasticity theory is also studied using mechanism based crystal plasticity theory. It is found that due to the high strain gradient in the vicinity of

the crack tip, i.e., in the range of 0.1 – 2 μm the stresses for the case of mechanism based strain gradient crystal plasticity theory were always found to be higher than for the conventional crystal plasticity theory. It is also found that the difference in the stresses from both theories is not large - this is due to the low intrinsic material length to size of plastic zone ratio. It is also found that overall fracture energies are the same from both theories.

In the last part a correlation is derived among the fracture energy, cohesive strength, work of adhesion and yield stress. And parameters for this correlations were identified for different orientations of niobium single crystalline material in the bicrystal niobium/alumina specimens.

The work presented in this thesis is focused on the modelling of interface fracture of niobium/alumina bicrystal specimens for various orientations of niobium single crystalline material. Conventional crystal plasticity theory and mechanism based strain gradient crystal plasticity theory have been used throughout the work to model the niobium single crystalline material. The interface fracture is modelled using a cohesive modelling approach.

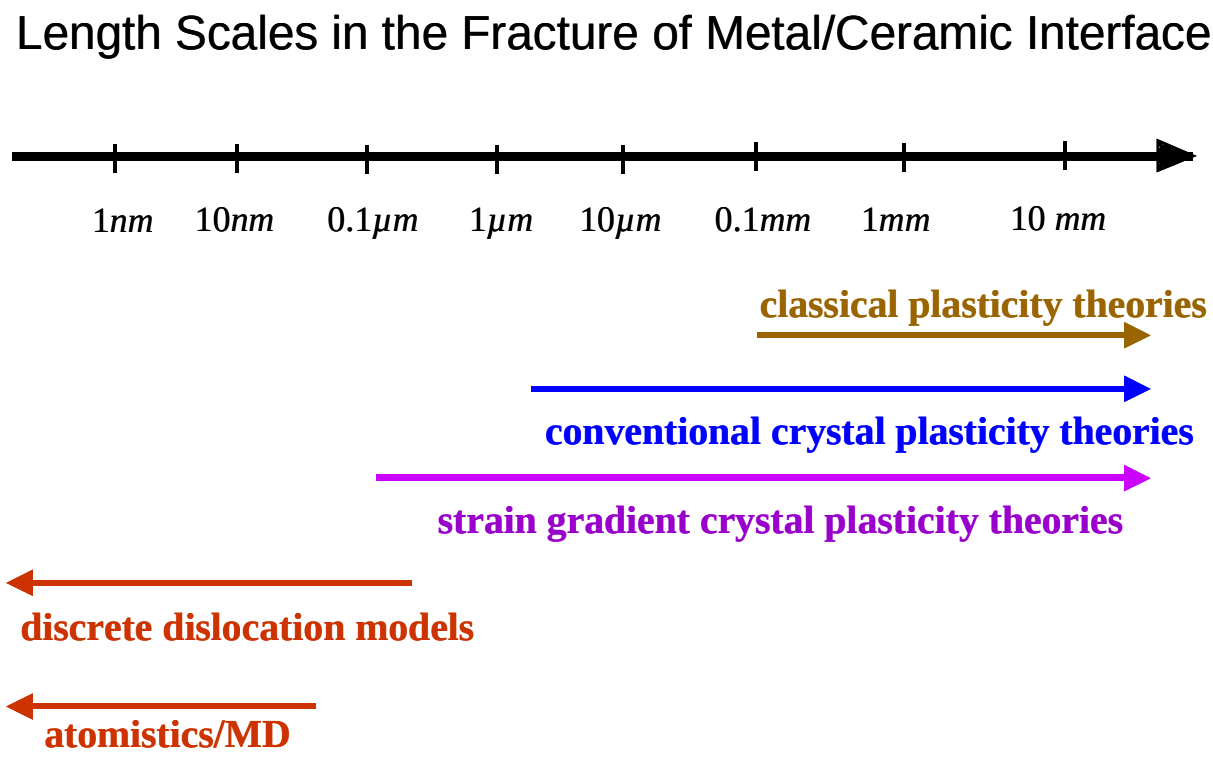

Figure 72: Length scales in the fracture of metal/ceramic interfaces

The outlook of the metal/ceramic interface fracture can be explained on the basis of different length scales involved in the fracture of metal/ceramic interfaces. As shown in figure 72 classical plasticity theory can be suitable above a length scale of ~ 0.1 mm because such theories are formulated for macroscopic elastic-plastic problems and below 0.1 mm deformation in each grain, grain size and grain boundary effects become more important,

therefore, it can only be used to study the macroscopic plastic zone developed around the crack tip for isotropic materials. Conventional crystal plasticity theory can be suitable above a length scale range of 1 - 2 μm while strain gradient crystal plasticity theory can be used above a length scale of 0.1 μm because these theories can be used to model the deformation behaviour of single and polycrystalline materials by taking into account the discrete slip system activities into the overall plastic strain. These two theories not only give macroscopic plastic zones developed around the crack tip but also give the plastic strain contribution coming from individual slip systems. These theories can also be used to study the plastic anisotropy of single crystalline materials due to the change in orientations, as is shown in this thesis.

Below 0.1 μm discrete dislocation events become more important and discrete dislocation models are suitable not only to study the discrete dislocation behaviour during crack propagation but also to quantify the stress level achieved around the crack tip. Below 100 nm molecular dynamics calculations can be used to derive the decohesion curves (traction-separation law) while ab-initio simulation results can be applied to derive the work of adhesion (W_{adh}) for metal/ceramic interface failure.

As discussed above this work concentrated upon linking three different length scales, i.e., macroscopic fracture behaviour, crystal plasticity theory (> 0.1 μm) and atomistic work of adhesion of metal/ceramic interfaces (< 0.1 μm). Future wok can be done by using discrete dislocation models in the range of 10 nm – 100 nm. This will further quantify the crack tip stress level reached during deformation in order to validate the cohesive law parameters identified during this work using crystal plasticity theory. Although this will not effect the results of macroscopic fracture energies computed in this work for various orientations due to the very small region, i.e., 10 -100 nm, but will provide qualitative comparison of the stress level around the crack tip computed from strain gradient theory and discrete dislocation models. Another important point could be the quantification of critical normal separation (δ_c) which is the normal separation value at complete failure. In this work these values are found to be in the range of 6 nm – 60 nm. These values can be quantified using either ab-initio or molecular dynamics simulations. Until now all ab-initio computations have been done using ideal conditions, i.e. ideally clean and perfect interface. That is why, the value of normal separation is always found to be relatively low (< 1 nm). One research direction could be to study such interfaces using either molecular dynamics or ab-initio simulations and study the dependence of cohesive law on interface properties, such as effect of small poorly bonded regions, surface roughness, lattice mismatch and surface impurities (not ideally clean surface).

From the above discussion it can be concluded with this remark that metal/ceramic interface fracture is an ideal problem to be addressed with a mixed atomistic-continuum mechanics simulation including discrete dislocation theory. The study of metal/ceramic interface fracture using a multiscale modelling approach is planned at the institute in the next stage.

References

[1] www.dentaltec.org.nz

[2] www.nasa.gov

[3] M. W. Finnis, The theory of metal-ceramic interfaces, J. Phys.: Cond. Mat. 8, 5811 (1996).

[4] E. Saiz, R. M. Cannon and A. P. Tomsia, Energetics and atomic transport at liquid metal/Al_2O_3, Acta Mater. 47, 4209 (1999).

[5] E. Saiz, A. P. Tomsia, K. Suganuma, Wetting and strength issues at Al/α-alumina interfaces, J. European Ceramic Society 23, 2787 (2003).

[6] A. P. Tomsia, E. Saiz, B. J. Dalgleish, and R. M. Cannon, in Proc. 4th Japan Int. SAMPE Symp. And Exposition, Tokyo (1995), invited keynote lecture.

[7] G. Soyez, Plastische Verformung und Rißbildung in druckbeanspruchten Niob/α-Al_2O_3-Verbunden, Ph. D. thesis, Stuttgart, 1996.

[8] G. Soyez, G. Elssner, M. Rühle, and R. Raj, Constrained yielding in niobium single crystals bonded to sapphire, Acta Mater. 46, 3571 (1998).

[9] H. F. Fischmeister. In: J. A. Pask, A. G. Evans, editors. Ceramic microstructures `86: role of interfaces. Plenum Press; 1987.

[10] M. G. Nicholas, R. J. Lee, Joining dissimilar materials, Metals Mater. 1, 348 (1989).

[11] M. G. Nicholas, T. M. Valentine, Waite M. J., The wetting of Alumina by copper alloyed with Titanium and other elements, J. Mater. Sci. 15, 2197 (1980).

[12] C. R. Kurkjian, W. D. Kingery, Surface Tension at Elevated Temperatures, III. Effect of Cr, In, Sn, and Ti on Liquid Ni Surface Tension and Interfacial Energy with Al_2O_3, J. Phys. Chem. 60, 961 (1956).

[13] A.G. Evans, M. Rühle, B. J. Dalgleish, P. G. Charalambides, The Fracture Energy of Bimaterial Interfaces, In: M. Rühle, A. G. Evans, M. F. Ashby, J. P. Hirth, (eds) Metal-ceramic interfaces. Oxford: Pergamon Press; 1990, p. 345.

[14] A.G. Evans, B. J. Dalgleish, The Fracture resistance of metal ceramic interfaces, Acta Metall. Mater. 40, S295 (1992).

[15] C. J. McMahon, V. Vitek, The effects of segregated impurities on intergranular fracture energy, Acta Metall. Mater. 27, 507 (1979).

[16] M. L. Jokl, V. Vitek, C. J. McMahon, A microscopic theory of brittle fracture in deformable solids, Acta Metall. Mater. 28, 1479 (1980).

[17] J. P. Hirth, J. R. Rice, On the thermodynamics of adsorption at interfaces as it influences decohesion, Metall. Trans. 11A, 1501 (1980).

[18] J. R. Rice, Z. Suo, J. S. Wang, Mechanics and thermodynamics of brittle interfacial failure in bimaterial systems, In: M. Rühle, A. G. Evans, M. F. Ashby, J. P. Hirth, (eds) Metal-ceramic interfaces. Oxford: Pergamon Press; 1990, p. 269.

[19] H. F. Fischmeister, W. Mader, B. Gibbesch, G. Elssner, Joining of ceramic, glass and metal, Mat. Res. Soc. Symp. Proc. 122, 529 (1988).

[20] G. E. Beltz, J. R. Rice, Dislocation Nucleation at metal/ceramic interfaces, Acta Metall. Mater. 40, S321 (1992).

[21] G. E. Beltz, J. S. Wang, Crack direction effects along copper/sapphire interfaces, Acta Metall. Mater. 40, 1675 (1992).

[22] D. Korn, Bruchenergie und plastische Verformung von grenzflächendotierten Metall-Keramik-Verbunden, Ph. D. Thesis, University of Stuttgart (1993).

[23] D. Korn, G. Elssner, R. M. Cannon, M. Rühle, Fracture properties of interfacially doped Nb-Al_2O_3 bicrystals: I, fracture characteristics, Acta Mater. 50, 3881 (2002).

[24] J. W. Kysar, Directional dependence of fracture in copper/sapphire bicrystal, Acta Mater. 48, 3509 (2000).

[25] M. Methfessel, D. Hennig and M. Scheffler, Trends of the surface relaxations, surface energies, and work functions of the 4d transition metals, Phys. Rev. B. 46, 4816 (1992).

[26] M. W. Finnis, C. Kruse and U. Schönberger, Ab initio calculations of metal/ceramic interfaces: what have we learned, what can we learn?, Nanostructured Mat. 6, 145 (1995).

[27] I. G. Baitrev, A. Alavi and M. W. Finnis, First-principle calculations of the ideal cleavage energy of bulk niobium(111)/alpha-alumina(0001) interfaces, Phys. Rev. Lett. 82, 1510 (1999).

[28] W. Zhang and J. R. Smith, Stoichiometry and adhesion of Nb/Al_2O_3, Phys. Rev. B. 61, 16883 (2000).

[29] P. E. McHugh, A. G. Varias, R. J. Asaro, C. F. Shih, Computational modelling of microstructures. Future Generation Computer Systems. 5, 295 (1989).

[30] R. J. Asaro, Geometrical effects in the inhomogeneous deformation of ductile single crystals, Acta Metall. 27, 45 (1979).

[31] R. J. Asaro, Micromechanics of crystals and polycrystals, In: J. W. Hutchinson (ed.), Advances in Applied Mechanics. Academic Press: New York; 1983. p. 2.

[32] R. J. Asaro, Crystal Plasticity, J. Appl. Mech. 50, 921 (1983).

[33] A. G. Varias, N. P. O'Dowd, R. J. Asaro, C. F. Shih, Failure of Bimaterial interfaces, Mater. Sci. Engg. A 126, 65 (1990).

[34] J. S. Wang, A Micromechanical Model for Interface Crack Extension in Metal/ceramic bimaterial systems, Acta Mater. 46, 4973 (1998).

[35] J. W. Kysar, Continuum simulations of directional dependence of crack growth along a copper/sapphire bicrystal interface: Part I, Experiments and crystal plasticity background, J. Mech. Phys. Solids 49, 1099 (2001).

[36] J. W. Kysar, Continuum simulations of directional dependence of crack growth along a copper/sapphire bicrystal interface: Part II, Crack tip stress and deformation analysis, J. Mech. Phys. Solids 49, 1129 (2001).

[37] J. W. Kysar, C. L. Briant, Crack tip fields in ductile single crystals, Acta Mater. 50, 2367 (2002).

[38] A. Nakatani, W. J. Drugan, E. Van der Giessen, A. Needleman, Crack tip fields at the ductile single crystal- rigid material interface, Int. J. of Fract. 122, 131 (2003).

[39] C. Kohnle, O. Mintchev, D. Brunner, S. Schmauder, Fracture of metal/ceramic interfaces, Comp. Mater. Sci. 19, 261 (2000).

[40] C. Kohnle, O. Mintchev, S. Schmauder, Elastic and plastic fracture energies of metal/ceramic joints, Comp. Mater. Sci. 25, 272 (2002).

[41] J. S. Wang, P. M. Anderson, Fracture behaviour of embrittled FCC metal bicrystals, Acta Metall. Mater. 39, 779 (1991).

[42] R. M. Cannon, D. Korn, G. Elssner, M. Rühle, Fracture properties of interfacially doped Nb-Al_2O_3 bicrystals: II, relation of interfacial bonding, chemistry and local plasticity, Acta Mater. 50, 3903 (2002).

[43] G. Elssner, G. Hörz, Probleme der Haftung bei Schichtverbindungen aus Keramik und Metall, Z. MetallKd. 62, 217 (1971).

[44] Z.C. Szkopiak, Hardness of niobium-nitrogen and niobium-oxygen alloys, J. Less Common Metals 19, 93 (1969).

[45] R. Hill, J. R. Rice, Constitutive Analysis of Elastic-Plastic Crystals at arbitrary strain, J. Mech. Phys. Solids 20, 719 (1972).

[46] P. H. Geubelle, J. Baylor, The impact-induced delamination of laminated composites: A 2D simulation, Composites Part B 29B, 735 (1998).

[47] I. Scheider, W. Brocks, Simulation of cup-cone fracture using the cohesive model, Engg. Fract. Mech. 70, 1943 (2003).

[48] R. W. Armstrong, Cleavage crack propagation within crystals by the Griffith mechanism versus a dislocation mechanism, Mat. Sci. and Engg. 1, 251 (1966).

[49] R. J. Price, A. Kelly, Deformation of age-hardened aluminium alloy crystals-II. Fracture, Acta Metall. 12, 979 (1964).

[50] W. J. Clegg, I. Horsfall, J. F. Mason, L. Edwards, The tensile deformation and fracture of Al-"Shaffil" metal-matrix composites, Acta Metall. 36, 2151 (1988).

[51] E. R. Fuller, B. R. Lawn, R. M. Thomson, Atomic modelling of chemical interactions at crack tips, Acta Metall. 28, 1407 (1980).

[52] Y. H. Chiao, D. R. Clarke, Direct observation of dislocation emission from crack tips in silicon at high temperatures, Acta Metall. 37, 203 (2003).

[53] M. A. Jameel, P. Peralta, C. Laird, Initiation and propagation of stage-I cracks in copper single crystals under load control, Mat. Sci. and Engg. A. 342, 279 (2003).

[54] G. I. Taylor, Plastic Strain in Metals, J. Inst. Metals 62, 307 (1938).

[55] R. Hill, Generalized Constitutive Relations for Incremental Deformation of Metal Crystals by Multislip, J. Mech. Phys. Solids 15, 79 (1966).

[56] J. R. Rice, Inelastic Constitutive Relations for Solids: An Internal-Variable Theory and its Application to Metal Plasticity, J. Mech. Phys. Solids 19, 433 (1971).

[57] R. Hill, J. R. Rice, Constitutive Analysis of Elastic-Plastic Crystals at Arbitrary Strain, J. Mech. Phys. Solids 20, 401 (1972).

[58] D. Peirce, R. J. Asaro, A. Needleman, Material Rate Dependence and Localized Deformation in Crystalline Solids, Acta Metall. 31, 1951 (1983).

[59] Y. Nakada, A. S. Keh, Latent hardening in iron single crystals, Acta Metall. 14, 961 (1966).

[60] A. H. Shalaby, K. S. Havner, A general kinematical analysis of double slip, J. Mech. Phy. Solids 26, 79 (1978).

[61] D. Peirce, R.J. Asaro, A. Needleman, An analysis of nonuniform and localized deformation in crystalline solids, Acta Metall. 30, 1087 (1982).

[62] T. Y. Wu, J. L. Bassani, Latent Hardening in Single Crystals I. Theory and Experiments, Mathematical and Physical Sciences 435, 21 (1993).

[63] T. Y. Wu, J. L. Bassani, Latent hardening in single crystals II. Analytical characterization and predictions. Philos. Trans. Roy. Soc. London A 435, 21 (1993).

[64] A. M. Cuitino, M .Ortiz, Computational modelling of single crystals, Modell. Simul. Mater. Sci. Eng. 1, 225 (1992).

[65] P. Franciosi, The concept of latent hardening and strain hardening in metallic single crystals, Acta Metall. 33, 1601 (1985).

[66] T. Kameda, M. A. Zikry, Three dimensional dislocation-based crystalline constitutive formulation for ordered intermetallics, Scr. Mater. 38, 631 (1998).

[67] T. Ohashi, K. Asakawa, Evaluation of Dislocation Storage by Means of Crystal Plasticity Analysis, Mat. Res. Soc. Symp. Proc. 683E, BBS5.4.1 (2001).

[68] J. Harder, A crystallographic model for the study of local deformation processes in polycrystals, Int. J. Plast. 15, 605 (1999).

[69] A. Arsenlis, D. M. Parks, Modeling the evolution of crystallographic dislocation density in crystal plasticity, J. Mech. Phys. Solids 50, 1979 (2002).

[70] A. Acharya, A model of crystal plasticity based on the theory of continuously distributed dislocations, J. Mech. Phys. Solids 49, 761 (2001).

[71] F. Erdogan, G. C. Sih, On the crack extension in plane loading and transverse shear, J. Basic Engg. 85, 519 (1963).

[72] G. I. Barenblatt, The Formation of Equilibrium Cracks During Brittle Fracture. General Ideas and Hypothesis. Axisymmetrical Cracks, PMM. 23, 434 (1959).

[73] G. I. Barenblatt, Mathematical Theory of Equilibrium Cracks, Advances in Applied Mechanics, Academic Press, NY, 55 (1962).

[74] D. S. Dugdale, Yielding of Steel Sheets Containing Slits, J. Mech. Phys. Solids 8, 100 (1960).

[75] A. Needleman, A continuum model for void nucleation by inclusion debonding, ASME J. Appl. Mech. 54, 525 (1987).

[76] A. Needleman, An analysis of decohesion along an imperfect interface, Int. J. Fract. 42, 21 (1990).

[77] X. P. Xu, A. Needleman, Numerical simulation of fast crack growth in brittle solids, J. Mech. Phys. Solids 42, 1397 (1994).

[78] X. P. Xu, A. Needleman, Void nucleation by inclusion debonding in a crystal matrix, Modell. Simul. Mater. Sci. Engg. 1, 111 (1993).

[79] V. Tvergaard, J. W. Hutchinson, The relation between crack growth resistance and fracture process parameters in elastic-plastic solids, J. Mech. Phys. Solids 40, 1377 (1992).

[80] V. Tvergaard, Effects of fibre debonding in a whisker-reinforced metal, Mater. Sci. Eng. A125, 203 (1990).

[81] J. Chaboche, R. Girard and P. Levasseaur, On the interface debonding models, Int. J. Damage Mech. 6, 220 (1997).

[82] G. T. Camacho, M. Ortiz, Computational modelling of impact damage in brittle materials, Int. J. Solids Struct. 33, 2899 (1996).

[83] P. H. Geubelle, J. Baylor, The impact-induced delamination of laminated composites: A 2D simulation, Composites, Part B. 29B, 589 (1998).

[84] I. Scheider, W. Brocks, Simulation of cup cone fracture using cohesive model, Eng. Fract. Mech. 70, 1943 (2003).

[85] I. Scheider, W. Brocks, The effect of the traction separation law on the results of cohesive zone crack propagation analyses, Key Engg. Mater. 251, 313 (2003).

[86] ABAQUS Version 6.4, Hibbitt, Karlsson, Sorenson.

[87] M. Anglada, F. Guiu, Cyclic deformation of Nb single crystals. Phil. Mag. A, 44, 499 (1981).

[88] D. K. Bowen, J. W. Christian, G. Taylor, Deformation properties of niobium single crystals. Canadian Journal of Physics 45, 903 (1967).

[89] M. S. Duesbery, R. A. Foxall, A detailed study of the deformation of high purity niobium single crystals. Phil. Mag. 27, 719 (1969).

[90] Y. Huang, A user–material subroutine incorporating single crystal plasticity in the ABAQUS Finite Element Program (1991).

[91] L. Meric, P. Poubanne, G. Cailletaud, Single crystal modelling for structural calculations, J. Engg. Mater. Tech. 113, 162 (1991).

[92] T. E. Mitchell, R. A. Foxall, P. B. Hirsch, Work hardening in niobium single crystals. Phil. Mag. 8, 1895 (1963).

[93] Stephane Quilici, Georges Cailletaud, FE simulation of macro-, meso- and micro-scales in polycrystalline plasticity, Comp. Mater. Sci. 16, 383 (1999).

[94] Tien-Yue Wu, John L. Bassani, Latent hardening in single crystals I. Theory and experiments, Mathematical & Physical Sciences 435, 21 (1993).

[95] A. Ma, D. Raabe, MPI, Düsseldorf (unpublished data).

[96] J. Mandel, Generalisation de la theorie de plasticite de W. T. Koiter, Int. J. Solids and Struct. 1, 273 (1965).

[97] U. F. Kocks, T. J. Brown, Latent hardening in aluminium, Acta Metall. 14, 87 (1966).

[98] ABAQUS Version 6.5, Hibbitt, Karlsson, Sorenson (2005).

[99] D. Korn, G. Elssner, R.M. Cannon, M. Rühle, Fracture properties of interfacially doped Nb-Al_2O_3 bicrystals: I, fracture characterisitics, Acta Mater. 50, 3881 (2002).

[100] L.B. Freund. Dynamic fracture mechanics. Cambridge University Press, 1998.

[101] Ronald Krueger, The virtual crack closure technique: History, approach and applications, ICASE Report no. 2002-10.

[102] C. P. Cherepanov, Crack propagation in continous media, Appl. Math. Mech. 31, 476 (1967).

[103] J. R. Rice, A path independent integral and the approximate analysis of strain concentrations by notches and cracks, J. Appl. Mech. 35, 379 (1968).

[104] A. Siddiq, S. Schmauder, Simulation of hardening in high purity niobium single crystals during deformation, Steel Grips, Journal of steel and related materials, 3, 281 (2005).

[105] J. W. Hutchinson, and Z. Suo, Mixed mode cracking in layered materials. Adv. in Appl. Mech. 29, 63 (1992).

[106] J. S. Wang, and Z. Suo, Experimental determination of interfacial toughness using Brazil-nut-sandwich. Acta Metall. 38, 1279 (1990).

[107] W. Brocks, I. Scheider, Numerical aspects of the path-dependence of the J-integral in incremental plasticity, Technical Note GKSS/WMS/01/08, internal report, 2001.

[108] C. Kohnle, O. Mintchev, D. Brunner, S. Schmauder, Fracture of metal/ceramic interfaces, in: Proc. Material Week (CD-ROM), 25.-28.09.2000, Munich, Germany http://www.materialsweek.org/proceedings (2000).

[109] Available from <www.goodfellow.com>.

[110] W. Ramberg, W. R. Osgood, Description of stress-strain curves by three parameters, NASA Technical Note No 902, 1945.

[111] O. Mintchev, J. Rohde, S. Schmauder, Mesomechanical simulation of crack propagation through graded ductile zones in hardmetals, Comp. Mater. Sci. 13, 81 (1998).

[112] Wilson, W. K. and Osias, J. R., A comparison of finite element solutions for an elastic-plastic crack problem, Int. J. Fract. 14, R95 (1978).

[113] Larsson, L. H., A calculational round robin in elastic-plastic fracture mechanincs, Int. J. Press. Vess. Piping 11, 207 (1983).

[114] C. G. Hwang, P. A. Wawrzynek, A. K. Tayebi, A. R. Ingraffea, On virtual crack extension method for calculation of the rates of energy release rate, Engng. Fract. Mech. 59, 521 (1998).

[115] M.G. Nicholas, editor. Joining of Ceramics. New York, NY: Chapman and Hall; 1990.

[116] R. L. Williamson, B. H. Rabin, G. E. Byerly, FEM study of the effects of interlayers and creep in reducing residual stresses and strains in ceramic-metal joints, Composite Engineering 5, 851 (1995).

[117] J. W. Hutchinson, M. E. Mear, J. R. Rice, Crack paralleling an interface between dissimilar materials. J. Appl. Mech. 54, 239 (1987).

[118] M. Y. He, J. W. Hutchinson, Crack deflection at an interface between dissimilar elastic materials. Int. J. Solids Structures 25, 1053 (1989b).

[119] T. Suga, Bruchmechanische Charakterisierung und Bestimmung der Haftfestigkeit von Materialübergängen, Ph. D. thesis, Stuttgart, 1983.

[120] D. F. Duffy, J. H. Hardning, A. M. Stoneham, A calculation of the structure and energy of the niobium/alumina interface, Acta Mater. 44, 3293 (1996).

[121] N. O'Dowd, C. F. Shih, M. G. Stout, Test geometries for measuring interfacial fracture toughness, Int. J. Solids Structures 5, 571 (1992).

[122] H. C. Cao, A. G. Evans, An experimental study of the fracture resistance of bimaterial interfaces, Mech. Mater. 7, 295 (1989).

[123] N. O'Dowd, Interface Fracture, in: K. H. J. Buschow, R. W. Cahn, M. C. Flemings, B. Ilschner, E. J. Kramer, S. Mahajan (eds.), Encyclopedia of materials. Oxford: Elsevier Science; 2001, p. 3273.

[124] C. F. Shih, J. R. Asaro, Elastic-plastic analysis of cracks on bimaterial interfaces: Small scale yielding, J. Appl. Mech. 55, 299 (1991).

[125] B. Chen, D. A. Dillard, The effect of the T-stress on crack path selection in adhesively bonded joints, Int. J. Adhesion & Adhesives 21, 357 (2001).

[126] H. C. Cao, A. G. Evans, An experimental study of the fracture resistance of bimaterial interfaces, Mech. Mater. 7, 295 (1989).

[127] A. R. Akisanya, N. A. Fleck, Brittle fracture of adhesive joints, Int. J. Fract. 58, 93 (1992).

[128] N. A. Fleck, W. Hutchinson, Z. Suo, Crack path selection in brittle adhesive layer, Int. J. Solids Structures 27, 1683 (1991).

[129] A. R. Akisanya, N. A. Fleck, Analysis of a wavy crack in sandwich specimens, Int. J. Fract. 55, 29 (1992).

[130] B. Cotterell, J. R. Rice, Slightly curved or kinked cracks, Int. J. Fract. 16, 155 (1980).

[131] X. Zhu, Y. J. Chao, Constraint effects on crack-tip fields in elastic-perfectly plastic materials, J. Mech. Phys. Solids 49, 363 (2001).

[132] C. S. Han, H. Gao, Y. Huang, W. D. Nix, Mechanism-based strain gradient crystal plasticity – I. Theory, J. Mech. Phys. Solids 53, 1188 (2005).

[133] C. S. Han, H. Gao, Y. Huang, W. D. Nix, Mechanism-based strain gradient crystal plasticity – II. Analysis, J. Mech. Phys. Solids 53, 1204 (2005).

[134] Y. Wei, J. W. Hutchinson, Models of interface separation accompanied by plastic dissipation at multiple scales, Int. J. Fract. 95, 1 (1998).

[135] I. E. Reimanis, B. J. Dalgleish, A. G. Evans, The fracture resistance of a model metal/cermic interface, Acta Metall. Mater. 39, 3133 (1991).

[136] G. Elssner, D. Korn, M. Rühle, The influence of interface impurities on fracture energy of UHV diffusion bonded metal-ceramic bicrystals, Scripta Metall. Mater. 31, 1037 (1994).

[137] A. Siddiq, S. Schmauder, Crystal orientation effects on the fracture energies of a bimaterial interface, Abstract no. 274, Proc. McMAT 2005 Mechanics and Materials Conference (CD-ROM), Louisiana, USA, 2005.

[138] A. Siddiq, S. Schmauder, Modelling of crystal plasticity effects on the crack initiation energies of a bicrystal interface, Computer Assisted Mechanics & Engng. Science 13, xxx-xxx (2006). (In press)

[139] K. B. Broberg, Cracks and fracture. Academic Press, London, 1999.

[140] S. Qu, Y. Huang, H. Jiang, C. Liu, P. D. Wu, K. C. Hwang, Fracture analysis in the conventinoal theory of mechanism-based strain gradient (CMSG) plasticity, Int. J. of Fract. 129, 199 (2004).

[141] MATLAB Version 6.0, The Mathworks, Inc, Massachusetts, 2004.

[142] Y. J. Kim, N. S. Huh, Y. J. Kim, Enhanced reference stress based J and COD estimation method for LBB analysis and comparison with GE/EPRI method, Fatigue Fract. Engng. Struct. 24, 243 (2001).

[143] L. Xia, C. F. Shih, J. W. Hutchinson, A computational approach to ductile crack growth under large scale yielding conditions, J. Mech. Phys. Solids 43, 389 (1995).

[144] T. Suga, G. Elssner, S. Schmauder, Composite parameters and mechanical compatibility of material joints, J. Comp. Mat. 22, 917 (1988).